

BIO-MIMETIC SMART SYSTEM FUNCTIONING LIKE

NATURAL SKIN AND MUSCLE

BY

ZHANAN ZOU

B.E., Southwest Jiaotong University, 2011

M.S., Zhejiang University, 2014

A thesis submitted to the
Faculty of the Graduate School of the
University of Colorado in partial fulfillment
of the requirement for the degree of
Doctor of Philosophy
Department of Mechanical Engineering

2019

This thesis entitled:
BIO-MIMETIC SMART SYSTEM FUNCTIONING LIKE NATURAL
SKIN AND MUSCLE
written by Zhanan Zou
has been approved for the Department of Mechanical Engineering

(Prof. Jianliang Xiao)

(Prof. Wei Zhang)

(Prof. Franck Vernerey)

(Prof. Gregory Whiting)

(Prof. Rong Long)

Date _____

The final copy of this thesis has been examined by the signatories, and we find that both the content and the form meet acceptable presentation standards of scholarly work in the above mentioned discipline.

Zhanan Zou (Ph.D., Mechanical Engineering)

BIO-MIMETIC SMART SYSTEM FUNCTIONING LIKE NATURAL SKIN AND MUSCLE

Thesis directed by Prof. Jianliang Xiao

Soft machines, or soft robotics, are emerging technologies bringing many exciting prospects for the coming future. Creating soft machines with biomimetic functions is of key importance for applications in bettering human life and creating more complex robotic systems. Various mechanisms have been adopted to mimic natural tactile sense, tough, muscular motion, and even artificial intelligence. Among these, developing a bio-mimetic system capable of self-healing and degradation that behaves like a muscular hydrostat is appealing for soft robotics. This thesis will mainly focus on developing both artificial skin and artificial muscles that can self-heal, be recycled, and function like biological tissue. To develop a biomimetic artificial skin, we adopted an imine-bonded polymer as the main component, and embedded silver nanoparticles as well as liquid metals to create conductive components. Our artificial skin is capable of re-healing and recycling, and can be mounted to a complex 3D surface without introducing damage and strains. Such artificial skin, at the same time, can sense pressure and temperature change, flow across the surface, and humidity change in the atmosphere. Recyclability enables this platform to not only serve as an artificial skin, but also for other electronics applications. The artificial muscles were also developed for this project based on a recently invented Liquid Crystal Elastomer, whose behavior is most similar to that of natural muscles. To achieve large actuation strains, a fast response, and small scale local controlling, a Liquid Metal was introduced for

stimulating the artificial muscle. Over 100% linear contracting strain was realized based on such a combination, which is greater than that of natural muscles. Bending and twisting deformation were also realized easily on such system. To further demonstrate the advantages of our artificial muscle, we integrated it into other passive soft elastomers like Ecoflex to mimic the camouflage behavior of cephalopods.

Keywords: Artificial skin, Artificial Muscle, Imine-bonding, Liquid Crystal Elastomer, Soft Robotics.

Dedication

To my family

ACKNOWLEDGEMENTS

Firstly of all, I appreciate the guidance from my advisor Prof. Jianliang Xiao in my Ph.D. study and research. Prof. Xiao helped me over the first tough years as a new Ph.D. student with his professions and patience. During these years, I had both the freedoms of trying my own ideas and getting instructions from his handful research experiences. I was very lucky to join his group in Fall 2014, and it proved to be the best choice in my life so far.

I'm also grateful for Prof. Wei Zhang from Chemistry Department in CU Boulder, one of my most important collaborators throughout my Ph.D. studies. I got handful of knowledge from him, as well as brain storms from a different background. His passion and optimism about research inspired both my study and life.

I would like to thank Prof. Franck Vernerey, and Prof. Rong Long for their brilliant comments and suggestions in my comprehensive exam. I am grateful for Prof. Gregory Whiting for serving as my committee member and his help on my recent research. I also thank Prof. Jae-Woong Jeong and Prof. Tam Vu for the fruitful collaborations with their groups.

I would like to thank my labmates Yan Li, Qingyang Sun, Chuanqian Shi, Haiqing Lu, Yimeng Liu, Yu Wang, Zhengwei Li, and Andres Villada, for the fruitful discussion and generous support. I appreciate the experimental assistance from Zepeng Lei, Yuan Qi, Chengpu Zhu, Yinan Lu, Xinpeng Zhao, and Raza Qazi.

I thank my parents, my uncle and aunt for their care and support, also my best friend Cesar Valencia for his encouragement.

Contents

Chapter 1 Introduction to artificial muscles and skins

| | | |
|-----|--------------------------------------|----|
| 1.1 | Background | 1 |
| 1.2 | Bio-inspired artificial skin..... | 3 |
| 1.3 | Bio-inspired artificial muscle | 6 |
| 1.4 | Motivation and mission..... | 10 |

Chapter 2 Rehealable and recyclable Artificial Skin¹²

| | | |
|-----|--|----|
| 2.1 | State of the art of Artificial Skin..... | 12 |
| 2.2 | Fabrications and results..... | 13 |
| 2.3 | Materials for polyimine E-skin | 27 |

Chapter 3 Investigating the rehealability of polyimines and their nano-composites

| | | |
|-----|--|----|
| 3.1 | Self-healing materials | 32 |
| 3.2 | Characterization of the rehealability of polyimine | 33 |
| 3.3 | Measurements and testing methods for polyimines..... | 43 |

Chapter 4 Bio-memetic camouflageable surfaces enabled by Liquid Crystal Elastomer

| | | |
|-----|---|----|
| 4.1 | Current researches about artificial camouflage..... | 46 |
| 4.2 | Fabrication and characterization of the Artificial Muscle | 48 |
| 4.3 | Materials and methods for artificial skin | 63 |

Chapter 5 Fabrication and characterization of highly deformable artificial muscle based on liquid crystal elastomer

5.1 Artificial muscles for robotics and healthcare 67

5.2 Fabrication and characterization of LCE based artificial muscle 69

5.3 Conclusion: 78

Chapter 6 A vivo-mimetic prosthetic hand with a tendon-pulley design

6.1 Current researches about Prosthetic hand 79

6.2 Fabrication and characterization of the prosthetic hand 81

6.3 Conclusion: 87

Bibliography.....88

FIGURES

| | |
|---|--------|
| Figure 1.1. Stretchable electronics | - 2 - |
| Figure 1.2. Wound healing mechanism of natural skins | - 4 - |
| Figure 1.3. Strategies of self-healing materials. | - 4 - |
| Figure 1.4. Environmental pollutions | - 5 - |
| Figure 1.5. various artificial muscle candidates for soft robotics..... | - 8 - |
| Figure 2.1. Rehealable, fully recyclable and malleable electronic skin (e-skin).... | - 14 - |
| Figure 2.2. Rehealing and characterization of the pure and conductive polyimine films..... | - 16 - |
| Figure 2.3. Recycling and characterization of the pure and conductive polyimine films..... | - 19 - |
| Figure 2.4. Characterization of the rehealable, fully recyclable and malleable e-skin..... | - 25 - |
| Figure 2.5. Polymerization of polyimine networks | - 27 - |
| Figure 2.6. Optical image of humidity sensor (left) and flow/temperature sensor (right)..... | - 29 - |
| Figure 2.7. Characterizations of temperature sensor. | - 31 - |
| Figure 3.1. Polymer synthesis and rehealing process..... | - 34 - |
| Figure 3.2. Optical microscopy images of the cross-section view of lap-joint polyimine films..... | - 36 - |
| Figure 3.3. Uniaxial tension test specimen and optical microscopy images of failure interfaces after tests. | - 38 - |
| Figure 3.4. Shear strength of rehealed interfaces of polyimine specimens. | - 40 - |

| | |
|--|--------|
| Figure 3.5. Characterization of conductive polyimines..... | - 41 - |
| Figure 3.6. Optical microscopy images of the top view of lap-joint polyimine films..... | - 43 - |
| Figure 4.1. Conceptual demonstration and experimental results of LLAM. | - 49 - |
| Figure 4.2. Characterization of the LLAM..... | - 51 - |
| Figure 4.3. Design and characterization of the APAT. | - 55 - |
| Figure 4.5. Self-sensing of LM/LCE based soft walker. | - 61 - |
| Figure 4.6. Finite element analysis for predicting such transformations..... | - 63 - |
| Figure 5.1. The design and fabrication process of the LCE/LM artificial muscle. | - 69 - |
| Figure 5.2. Contraction test of the artificial muscle. | - 70 - |
| Figure 5.3. Temperature and contraction characterization of the artificial muscle. | - 72 - |
| Figure 5.5. Pulling force characterization of the artificial muscle. | - 75 - |
| Figure. 6.1 Design, fabrication, and the structure of LCE..... | - 79 - |
| Figure. 6.2 The performance of LCE | - 81 - |
| Figure. 6.3 Control fingers to achieve different actions. | - 83 - |
| Figure. 6.4 The practical application of robot hand. | - 84 - |

Chapter 1

Introduction to artificial muscles and skins

1.1 Background

Biological systems are complex and delicate, to adjust to such objects, scientists and engineers are seeking for more bio-friendly and bio-related solutions. Soft robotics and Artificial sensing are emerging areas to shoot this target. To develop a bio-mimetic system that most fits human body, a well conformal artificial skin and a muscular artificial tissue can pave the way for soft robotics serving people's everyday life.

To be conformal to human body, those systems, at the first place, should be soft and smooth. Pioneer researches include super-stretchable electronics that are either based on conventional chips, thin film materials and serpentine interconnectors or on organic semiconductors that are intrinsically stretchable, indicated in Fig. 1.1. Highly stretchable devices that are able undergoing over 100% bi-axial strain without damage is show in Fig. 1.1A. Multiple serpentine structures are introduced here, so that when the 1st order reaches its limit, the second order take charge, enabling the whole device deform as much as possible[1]. Those methods still depend on conventional chips and metals, that are rigid and venerable to large deformation. While other researchers explored the more intrinsic way of stretchable electronics, i.e., the organics semiconductors, shown in Fig.1.1B. The conventional chips that are consist of silicone and metals are replaced with organic

semiconductors and same functional transistor are fabricated[2]. Applications of such approaches various from strain/pressure sensors to organic LEDs. More promisingly, both strategies apply to human skin directly and are able to serve for days and month owing to their stretchability, show in Fig.1.1C[3]. The stretchable devices are able to sense the deformation of the skin, having therapy, or collecting bio-chemicals directly from the skin[4]. Apart from these, multi-functions have been achieved as well, indicated in Fig.1.1D, in which all types of sensors are integrated together, including the antenna for data transmission[5].

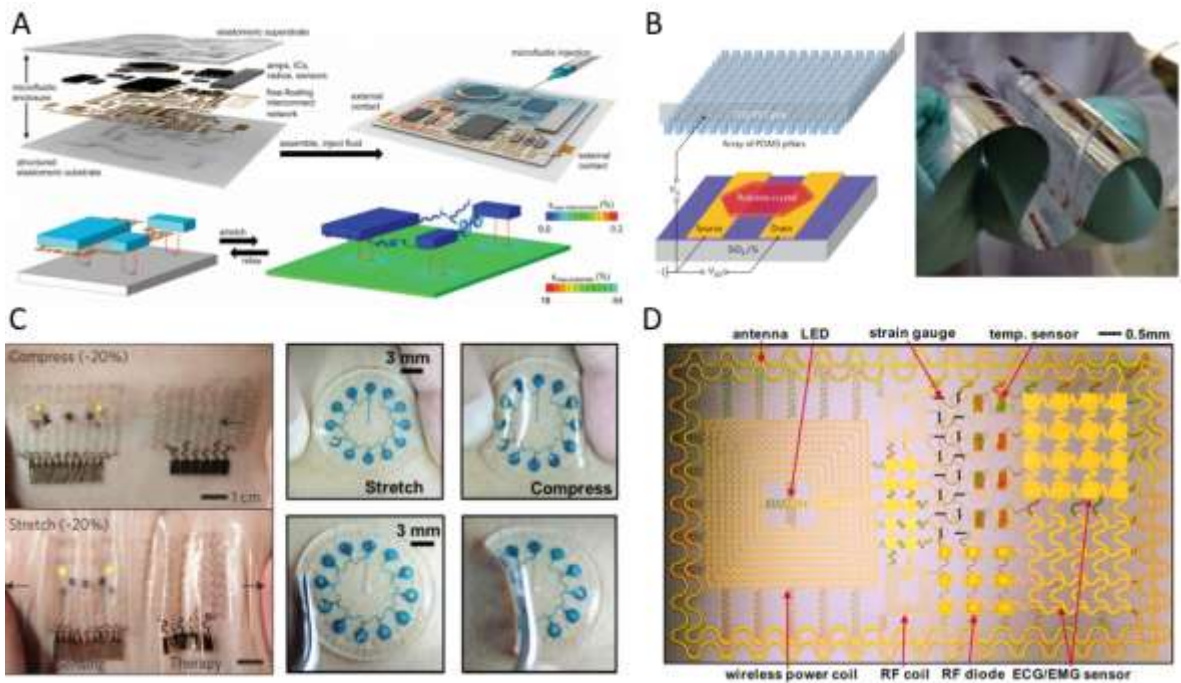


Figure 1.1. Stretchable electronics. (A) Soft and hard components are integrated together, serpentine interconnectors are introduced for the super stretch ability[1]. (B) Examples of Organics semiconductors[2]. (C) Stretchable electronics are able to attach to human skin and deform along it without damage, as well as collecting bio-chemicals[3,4]. (D) multi-functional devices are possible in such platform[5].

1.2 Bio-inspired artificial skin

The natural skins, however, are not only stretchable but pertains way more functionalities than current state of art of the stretchable electronics. Actually, biological skin plays an important role of living creatures in interacting with the environment. Skin not only protects the internal tissues and organs, but also provides sensation of temperature, pressure, vibration and haptics[6], [7]. It's been of great interest to the research community to design and fabricate electronic skins (e-skins) with functionalities and mechanical properties comparable to natural skin, due to their great potential in robotics, prosthetics, healthcare and human-computer interface.

Moreover, natural skin pertains the ability to repair itself when damage/ wound happens, as indicated in Fig.1.2. The mechanism behind this is quit complex, which is the result of millions of years of biological evolution, each cell functions like a small robot to deliver the nutrition, repair, and replace the old/dead tissues[8]. However, much simpler mechanism is available in polymer material science that includes, encapsulation of rehealing materials, hydrogen bonding functional groups in polymers, and dynamic covalent bonding in polymer networks, shown in Fig.1.3. A straightforward method is to including healing agent inside of materials that forms as micro encapsulations, while releasing the materials inside when damages happen to certain areas, shown in Fig.1.3A[9]. However, the healing agent that leaks out of the matrix potentially change the surface texture of the materials and forms potential defects at that area. Introducing hydrogen bonding in polymer network is promising in terms of efficient and robust self-healing,

indicating in Fig.1.3B[10]. The damaged area can be completely recovered without introducing any extra materials. Other mechanisms adopted the dynamic covalent bonding polymer networks that pertains similar functionalities, while having the freedom of various materials as candidates[11].

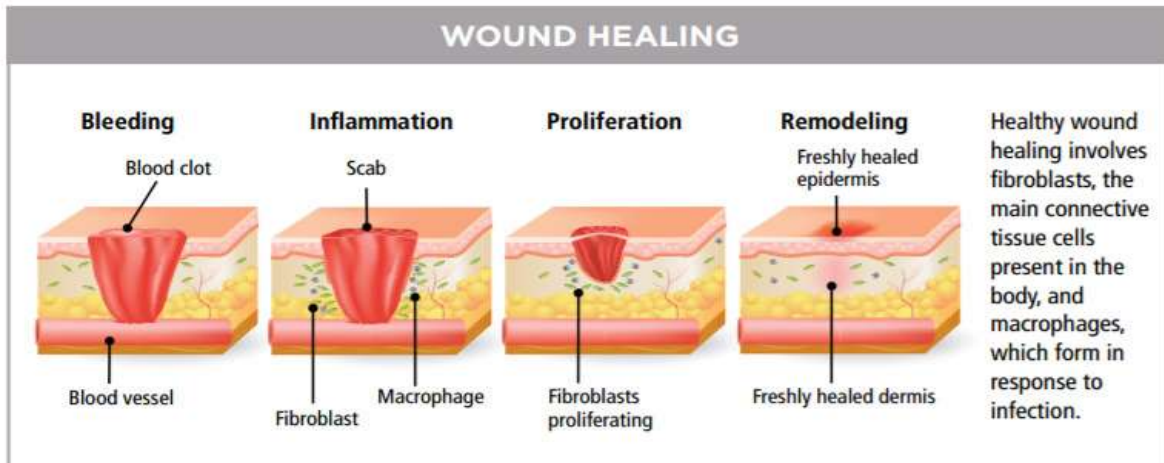


Figure 1.2. Wound healing mechanism of natural skins [8]

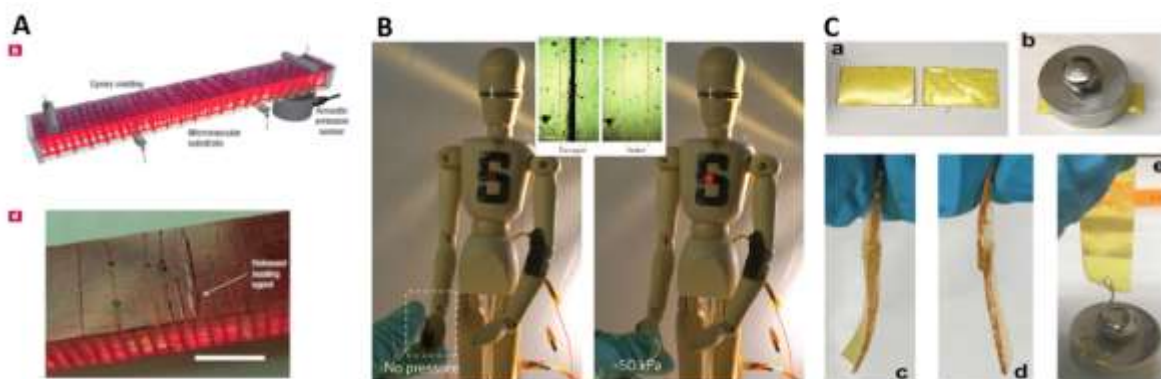


Figure 1.3. Strategies of self-healing materials. (A) healing agent encapsulated inside of materials [9]. (B) Polymer networks with hydrogen bonding[10]. (C) Polymer networks with covalent bonding [11].

Another functionality of natural skin, maybe not noticeable but very important, is their capability of be recycled. When tissues are dead or damaged, they get “decomposed” by either body immune system or nature environment into basic elements. As the development of human society, decomposing artificial stuff or manmade stuff became an issue that is getting more and more urgent. And it’s not just artificial skin or flexible electronics themselves, but even more broad products. Everyday, billions of ton of waste were either dumped into the ocean or berried under earth, making the potential threatening of our offspring, as see in Fig. 1.4 the poisonous element could get into plants first and then trough the eco-system to the human bodies[12].

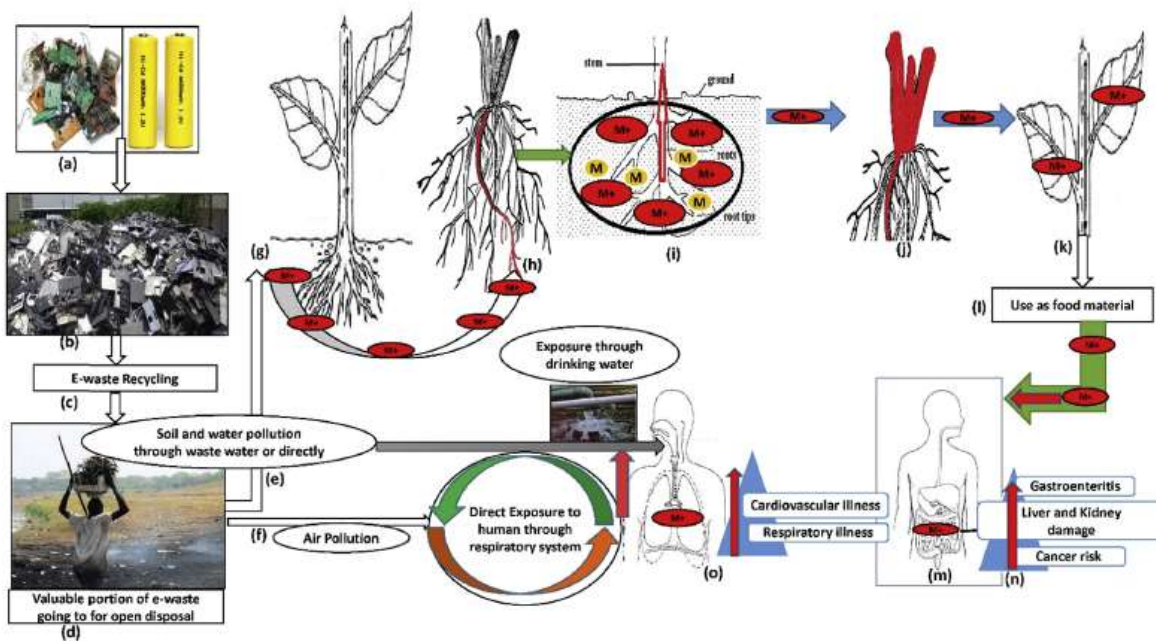


Figure 1.4. Environmental pollutions [12]

Thus, developing a both healable and recyclable artificial skin could benefit the future. Recently we developed a novel class of catalyst-free recyclable covalent network polymer[11], prepared from commercially available monomers: terephthalaldehyde, ethylene triamine and triethylene tetraamine through imine condensation reaction. Simply mixing these monomers in certain stoichiometry in organic solvent, and leaving the reaction at room temperature overnight, a coherent, hard and glassy poly-imine solid formed. The resulting dynamic covalent polymer can be healed and reshaped because of reversible bond exchange with simultaneous bond forming/breaking reaction, which let crosslink density of the polymer remain constant[13]–[16]. The polymer becomes malleable when heated to 60°C, also enable by the fast exchange (i.e break and reform) of imine bonds. Such poly-imine materials can also be fully recycled between powder and coherent solid form, and the recycling of this material doesn't decrease its mechanical strength over multiple generations[11]. It should be noted that traditional thermosets materials, highly cross-linked polymeric networks connected with irreversible covalent bonds cannot be reprocessed or reshaped once polymers are cured[17], while dynamic covalent networks can still maintain their reprocessibility and recyclability in addition to their high mechanical strength[18]–[21]. All these unique physical properties and ready accessibility of poly-imine make it a strong candidate for being used as the polymer matrix for artificial skin.

1.3 Bio-inspired artificial muscle

Beneath the skins, muscle plays an important role as well. Conventional actuators are bulky, rigid and lack of flexibility. Smart active materials enable actuations be more

similar to natural locomotion. Among all living creatures, soft animals are capable of dramatically deforming their bodies to another topology. Leach, for example, can elongate its body to over 5 times of its original length, suck surfaces with different texture and stiffness, and move with multiple locomotion. The naturally selected animals inspired researchers and scientists to investigate all types of Soft Robotics, mimicking natural animals and functionalities[22]. While the key to the success of bio-mimetic soft robotics is the ‘muscle’ that enlivens a piece of soft material. Various studies have been introduced to establish the bio-mimetic soft actuators, artificial muscles and soft robotics. Pneumatic actuation and dielectric effect are widely adopted for such purposes, as indicated in Fig.1.5. The pneumatic soft robot is capable of deforming into complex shape and at the same time output large force (Fig.1.5A)[23]. Dielectric elastomer actuators pertain fast response and self-sensing capability, making them good candidate for membrane based actuators (Fig.1.5B)[24], [25]. Shape memory alloy can deform linearly and be programed into complex shape, and can also be embedded into elastomers as the internal muscle that drives the soft robot moving forward, bending, and even jump, shown in Fig.1.5C[26]. Ionic polymer metal composite actuators require low operating voltage and save energy, thus an independent soft robot was able to be achieved with simply design, shown in Fig. 1.5D[27].

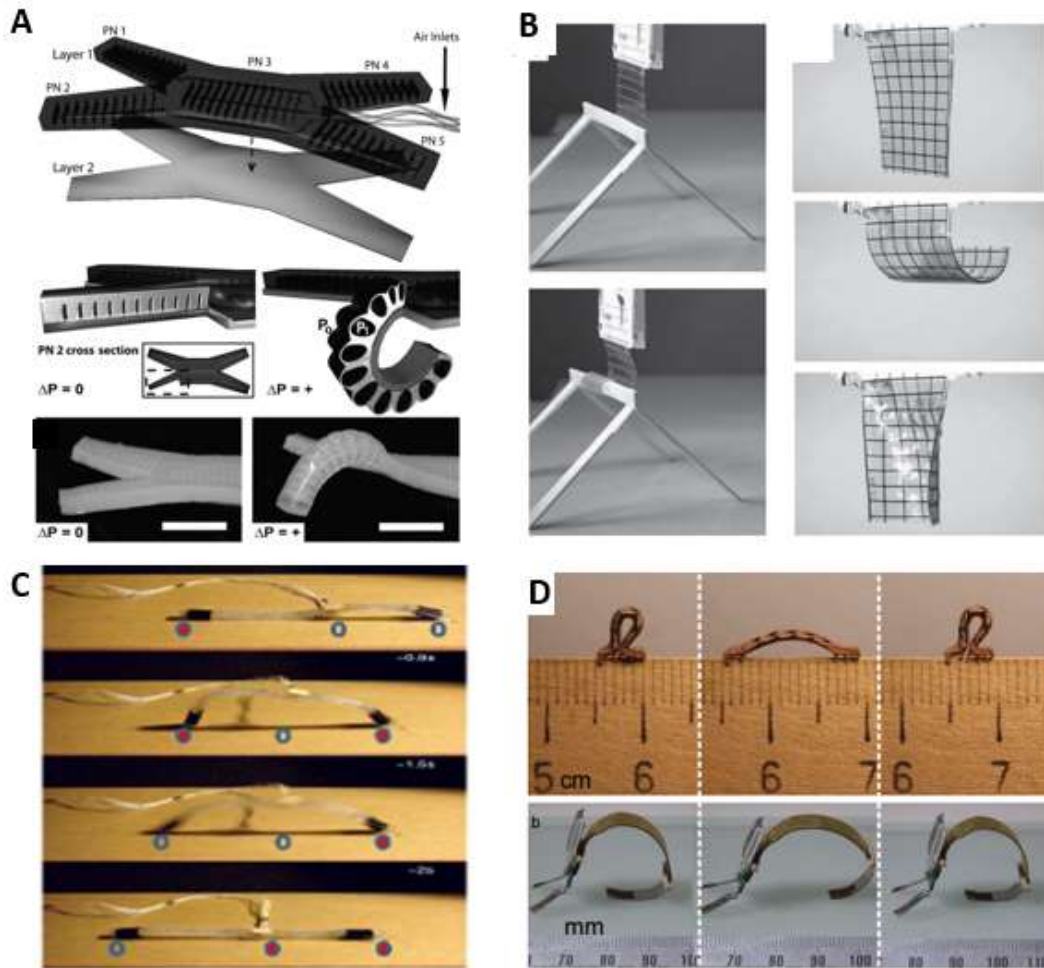


Figure 1.5. various artificial muscle candidates for soft robotics. (A) Pneumatic actuation[23]. (B) Dielectric elastomer actuator[24]. (C)Shape memory alloy actuator[26]. (D)Ionic polymer Metal composite actuator[27].

However, the requirements of fixed pre-stretch, high voltage, snap-through instability and pumping systems limit the design, fabrication and application of above methods[28], [29]. Liquid Crystal Elastomers (LCEs), on the other hands, exhibit the most similar actuation to natural muscle, due to their dramatic contraction[29], reversible deformations[30], responses to multiple stimuli[22], and great potentials for micro-scale robotics[30], [31]. To mimic the performance of natural muscular tissues, efficient driving of LCE artificial muscles plays an important role, as well as the great potential of deformation. Alignment, prior to actuation, is critical for LCE actuators. Various methods have been considered including taking advantage of diamagnetic and dielectric anisotropy of mesogens, which is limited to certain monomers and requires large magnetic fields[32]. Surface patterning, achieved by such means as rubbing with a cloth, is adopted as well, but limited to thin membranes ($<100\text{ }\mu\text{m}$)[33]–[37]. Mechanical alignment is the most widely used option due to its convenience and ease of operation, offering the most potential for LCE actuators to mimic the large, linear actuation of natural muscle tissues. Stimulating the aligned LCEs also remains a challenge. Introducing a dye into the LCE network to enable a response to light proves to be a good method, but is confined to certain formulas and difficult for precise unit controlling. In other cases, heaters were adhered to the surface of aligned LCE layers to trigger phase disorder of the aligned LCE sheet, but this method was limited to small local strain and bending deformation[31]. Embedding heaters into the LCE material could efficiently enhance the heat transferring from the heaters to the LCE network and enable linear actuation closer to natural muscle tissues. Unfortunately, conventional heaters based on solid metal and composite materials could be damaged under large alignment strain (up to 600%)[38].

Liquid Metal (LM), however, can handle such deformation without any problem, and is especially suitable for LCE alignment. Further, LM heaters would never introduce any extra confinements to the active polymer network, owing to their fluidic properties above a certain temperature. Compared to solid metals, such as copper and gold, LM also has a relatively lower conductivity ($3.4 \times 10^6 \text{ S m}^{-1}$)[39], which turns out to be good news for heaters.

1.4 Motivation and mission

In the first part of this thesis (chapter I and chapter II), I will demonstrate a not only rehealable, but also fully recyclable and malleable e-skin that can sense pressure, flow, temperature and humidity. This e-skin is based on a newly developed dynamic covalent thermoset (polyimine) doped with silver nanoparticles (AgNPs). Comparing with the other rehealable devices and electronics, our e-skin can be not only rehealed, but also fully recycled and reprocessed, due to the reversible bond exchange through simultaneous bond forming and breaking reactions under certain external stimuli[11], [18]. Furthermore, covalently bonded thermoset matrix used in this work ensures better mechanical strength and chemical stability of the e-skin under the service condition than other approaches[9], [10], [40]–[45]. These properties are distinct from conventional thermoset materials that cannot be reprocessed, reshaped and recycled due to their highly cross-linked polymeric networks connected with irreversible covalent bonds. The prominent characteristics of the e-skin represent an economical and eco- friendly technology that can find wide applications in robotics, prosthetics, health monitoring, and biomedical devices.

In the second part (chapter III, chapter IV, and chapter V), I also investigated biomimetic artificial muscle, in which we choose an LCE network based on a two-stage thiol-acrylate reaction[46], and embed patterned LM heater (99.99% Gallium, Amazon) directly into the LCE network. The LM heater deforms with the LCE network during alignment with no damage. Linear actuation, bending, and twisting are easily realized with this system. Gallium (melting at 30°C) was chosen as the material for the LM heater and patterned using stencil methods. The LM heater not only remain robust during actuation but also does not confine the deformation of LCE networks. Large linear strains over 100% can be realized, much higher than natural muscle. Inspired by biological tissue, passive and active materials are then combined as a system, mimicking dramatically changing surface patterns.

Chapter 2

Rehealable and recyclable Artificial Skin

2.1 State of the art of Artificial Skin

As the largest organ in human body, skin plays an important role in our daily interaction with the environment. Skin not only protects the internal tissues and organs, but also provides sensation of temperature, pressure, vibration and haptics [6], [7]. It's been of great interest to the research community to design and fabricate electronic skins (e-skins) with functionalities and mechanical properties comparable to natural skin, due to their great potential in robotics, prosthetics, healthcare and human-computer interface. Different sensing capabilities of e-skins have been realized, by integrating tactile/pressure sensors [3], temperature sensors [5], [47], strain sensors [48], [49], humidity sensors [47, 49], and chemical sensors [50]. To achieve good compliance and conformability, design principles developed in flexible and stretchable electronics were introduced to achieve flexible and stretchable e-skins [1], [51]–[59]. Inspired by the wound healing capability of natural skin, rehealable e-skins have also been developed [9], [10], [40]–[45], [60]–[66].

In this work, we demonstrate a not only rehealable, but also fully recyclable and malleable e-skin that can sense pressure, flow, temperature and humidity. This e-skin is based on a newly developed dynamic covalent thermoset (polyimine) doped with silver

nanoparticles (AgNPs). Comparing with the other rehealable devices and electronics, our e-skin can be not only rehealed, but also fully recycled and reprocessed, due to the reversible bond exchange through simultaneous bond forming and breaking reactions under certain external stimuli [35, 36]. Furthermore, covalently bonded thermoset matrix used in this work ensures better mechanical strength and chemical stability of the e-skin under the service condition than other approaches [22-24]. These properties are distinct from conventional thermoset materials that cannot be reprocessed, reshaped and recycled due to their highly cross-linked polymeric networks connected with irreversible covalent bonds. The prominent characteristics of the e-skin represent an economical and eco-friendly technology that can find wide applications in robotics, prosthetics, health monitoring, and biomedical devices.

2.2 Fabrications and results

The rehealable and recyclable e-skin integrates tactile, flow, temperature, and humidity sensors, as shown conceptually in Fig. 2.1A. These sensors are fabricated using conductive polymers, obtained by doping dynamic covalent thermoset polyimine with silver nanoparticles (AgNPs). They are then integrated onto a polyimine substrate by heat pressing, to ensure malleability, rehealability and full recyclability of the entire e-skin. Covalent bonds are formed between the sensors and the substrate due to dynamic covalent bond exchange reactions at the interfaces. Serpentine interconnects are adopted to minimize the effects of strain on sensor performance when deformed. The e-skin can be easily

conformed onto curved surfaces, e.g. human arms and robotic hands, by applying moderate heat and pressure (Fig. 2.1A, left). The geometrical conformity of the e-skin is

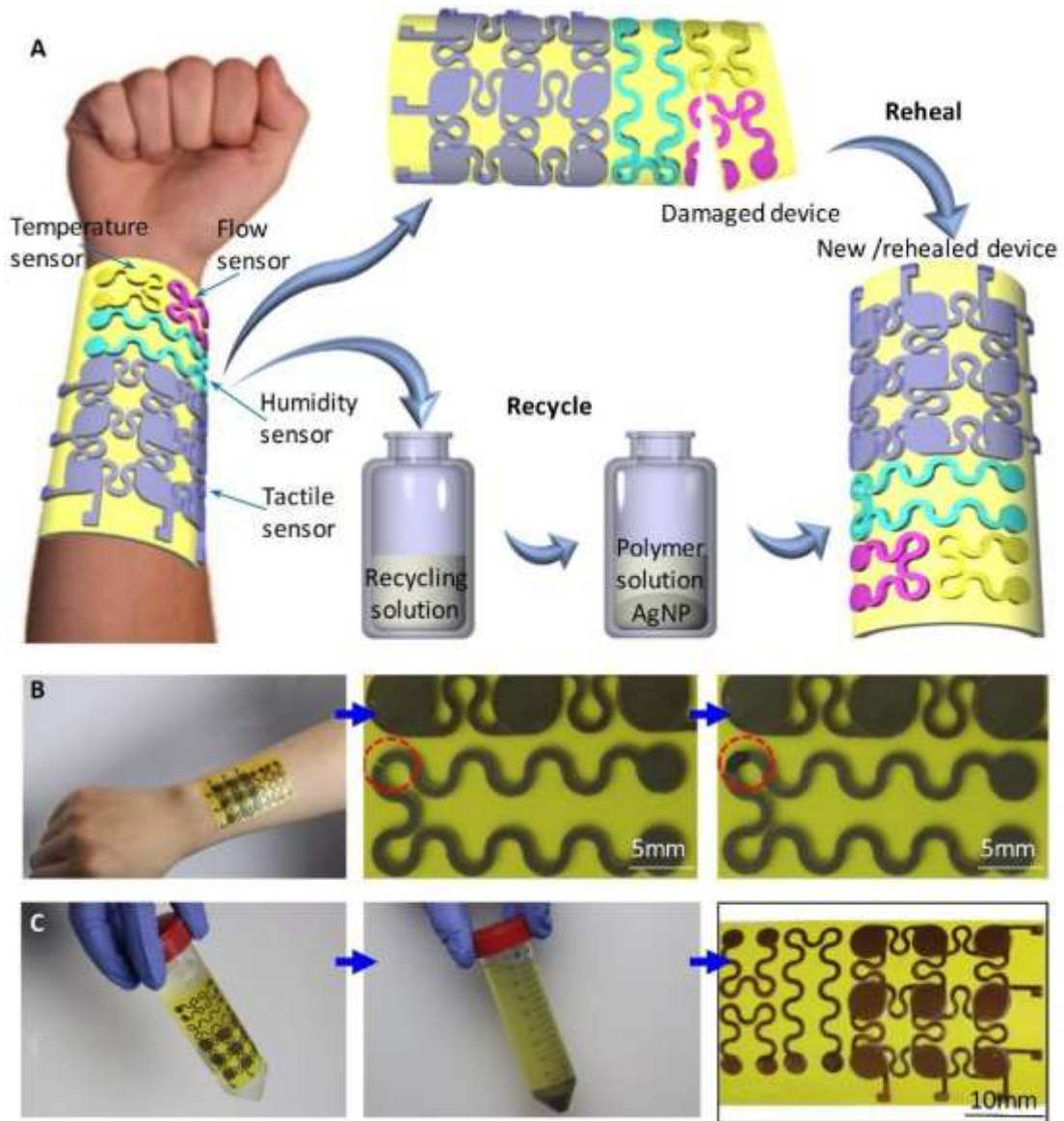


Figure 2.1. Rehealable, fully recyclable and malleable electronic skin (e-skin). (A) Schematic illustration of rehealability and full recyclability of the e-skin. (B) The malleable e-skin can be conformally mounted onto a human arm (left). When mechanically cut broken (middle), the e-skin can be rehealed by applying a small amount of rehealing agent and heat pressing (right). (C) The e-skin can be fully recycled using the recycling solution (left),

yielding the solution with dissolved oligomers/monomers and AgNPs at the bottom (middle).

The solution and AgNPs can be reused to make a new e-skin (right).

permanent due to its malleability, even after the pressure or force is removed[2], [67]. When moderately damaged (Fig. 2.1A, top center), the e-skin can be rehealed (Fig. 2.1A, right). The rehealed e-skin can restore mechanical and electrical properties comparable to the original device. When severe damage occurs or the device is never needed, the whole e-skin can be fully recycled, leaving no waste at all. Once recycled, short oligomer/precursor solution and AgNPs are obtained (Fig. 2.1A, bottom center), and can be used for making new materials and devices (Fig. 2.1A, right). Optical images in Fig. 2.1B illustrate the rehealing process of an e-skin. Due to the malleability provided by polyimine substrate, the e-skin can be conformally mounted onto a human arm (Fig. 2.1B, left). When a sensor is broken due to mechanical cutting (Fig. 2.1B, middle), it completely loses its functionality. By applying a small amount of rehealing agent and heat pressing (8.5 kPa at 80°C), the broken sensor is rehealed, regaining its full sensing capability and mechanical integrity (Fig. 2.1B, right). To recycle the e-skin, simply soaking the whole device into the recycling solution (Fig. 2.1C, left) makes the polymer matrix degrade into oligomers and monomers that are soluble in ethanol (Fig. 2.1C, middle), and the AgNPs sink to the bottom of the solution (bottom dark part). The recycled solution and nanoparticles are then used to make a new, functional e-skin (Fig. 2.1C, right).

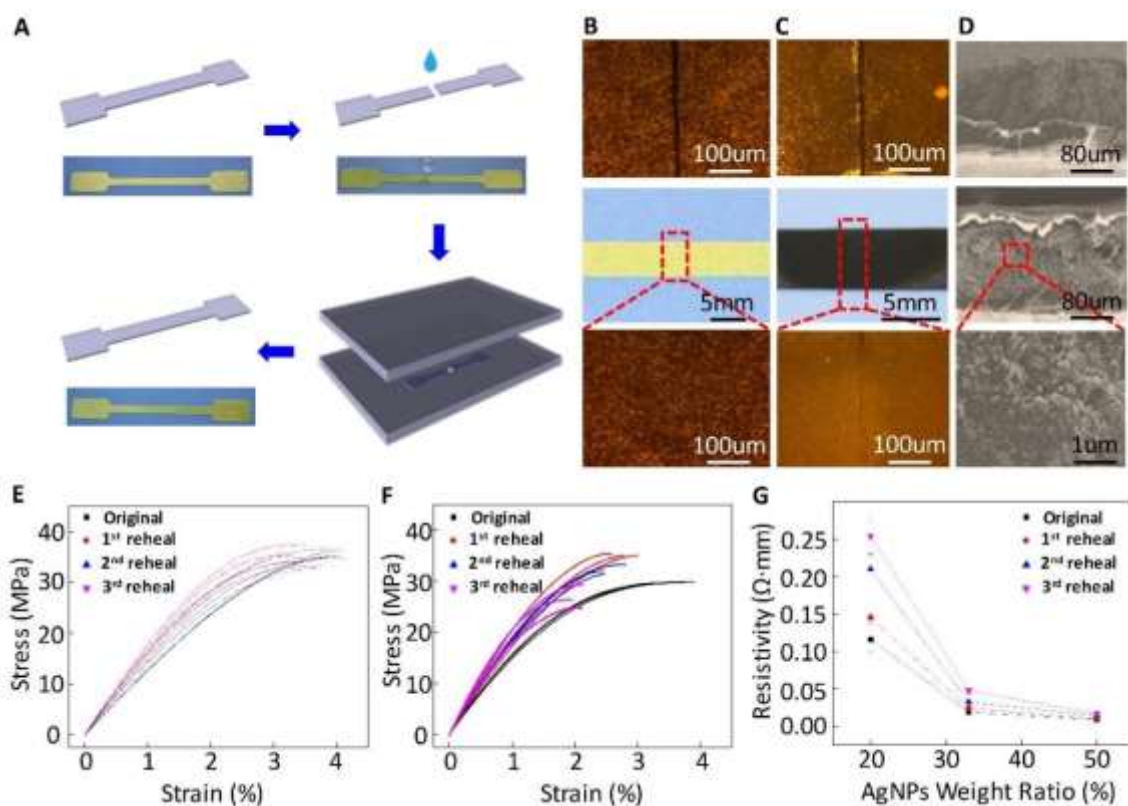


Figure 2.2. Rehealing and characterization of the pure and conductive polyimine films.

(A) Schematic illustration of the rehealing process. Optical images of the polyimine film are shown at the bottom of each frame. (B) Optical microscopy images of a pure polyimine film that is cut broken (top) and rehealed (bottom). After rehealing, the cut is invisible (middle and bottom). (C) Optical microscopy images of a conductive polyimine film that is cut broken (top) and rehealed (bottom). After rehealing, the cut is invisible (middle), but traces of the cut can still be seen under microscope (bottom). (D) Scanning electron microscopy images of the cross sections of a conductive polyimine film before (top) and after rehealing (middle). The magnified view at the bottom shows the dispersion of AgNPs in the polymer network. Uniaxial tension test results of pure (E) and conductive (F) polyimine films before and after rehealing. Three samples were tested for each case. (G)

Electrical resistivity measurements of the conductive polyimine films with different AgNP weight ratios before and after rehealing.

The detailed rehealing process of a pure polyimine polymer film is schematically illustrated in Fig. 2.2A, with optical images of the polyimine film shown at the bottom of each frame. A polyimine film is prepared by mixing three commercially available compounds: terephthalaldehyde (1), diethylenetriamine (2) and tris(2-aminoethyl)amine (3) in ethanol (see supporting information for details). The polyimine film (Fig. 2.2A, top left) is cut broken along its width direction (Fig. 2.2A, top right). By applying a small amount of rehealing solution (compounds 1, 2, and 3 in ethanol) at the cut area and heat pressing (Fig.2.2A, bottom right), the cut is rehealed (Fig. 2.2A, bottom left). During rehealing, the new oligomers/polymers grow across the broken surfaces. This eventually leads to covalent (chemical) bonding of the two pieces, leaving no interfaces in the rehealed area, which mimics the natural skin rehealing process. This mechanism is different from traditional ways of bonding two material parts together, which rely on van der Waals (physical, non-covalent) interactions to form physical bonding at the interface. The interfaces remain after bonding, which usually lead to significant degradation in mechanical properties, such as elastic modulus and tensile strength. Figure 2.2B shows optical microscopy images of the cut at different stages of the rehealing process. The cut has a width of $\sim 20\ \mu\text{m}$ initially (Fig. 2.2B, top), and becomes invisible after it's rehealed, even under optical microscope (Fig. 2.2B, middle and bottom). The conductive polyimine film, obtained by doping dynamic covalent thermoset polyimine with AgNPs at 33% weight ratio, can be rehealed through the same process as described in Fig. 2.2A, except that the rehealing agent consists of

compounds 1, 2, 3, and AgNPs in ethanol. The top frame of Fig. 2.2C shows an optical microscopy image of a cut of width $\sim 20\ \mu\text{m}$ in a conductive polyimine film. After applying rehealing agent and heat pressing, the cut is rehealed and becomes invisible (Fig. 2.2C, middle). Under optical microscope, traces of the cut can still be seen, probably because the presence of AgNPs affects polymerization of monomers/oligomers. Scanning electron microscopy (SEM) images of cross sections of the conductive polyimine before and after rehealing are shown in the top and middle frames of Fig. 2.2D, respectively. Good dispersion of AgNPs in the polymer network is shown in the magnified view (Fig. 2.2D, bottom).

Uniaxial tension test is conducted to compare the mechanical properties of pure and conductive polyimine films before and after rehealing. As shown in Fig. 2.2E, pure polyimine films restore their mechanical properties, such as elastic modulus, tensile strength and maximum tensile strain, even after three times rehealing. In addition, we observed that the locations of failure of the rehealed films were different from the previous failure points, indicating perfect rehealing effects. Figure 2.2F presents uniaxial tension test results of conductive polyimine films (33% AgNP weight ratio) before and after rehealing. The elastic modulus and tensile strength are retained or even slightly increased. The average maximum tensile strain decreases by 23%, 26% and 44% after 1st, 2nd and 3rd rehealing, probably because AgNPs complicate the interfacial bonding interactions, and multiple heat pressing treatments increase the brittleness of the films. Electrical resistivities of the conductive polyimine before and after rehealing are also investigated, for three different AgNP weight ratios (20%, 33% and 50%), as shown in Fig. 2.2G. After 1st, 2nd and 3rd rehealing, the electrical resistivity increases by 20% (27%, 13%), 44%

(70%, 59%) and 119% (150%, 88%) for 25% (33%, 50%) AgNP weight ratio. In the following, conductive polyimine films with 33% AgNP weight ratio are used to fabricate sensors in the e-skin, due to their good electrical property and mechanical robustness.

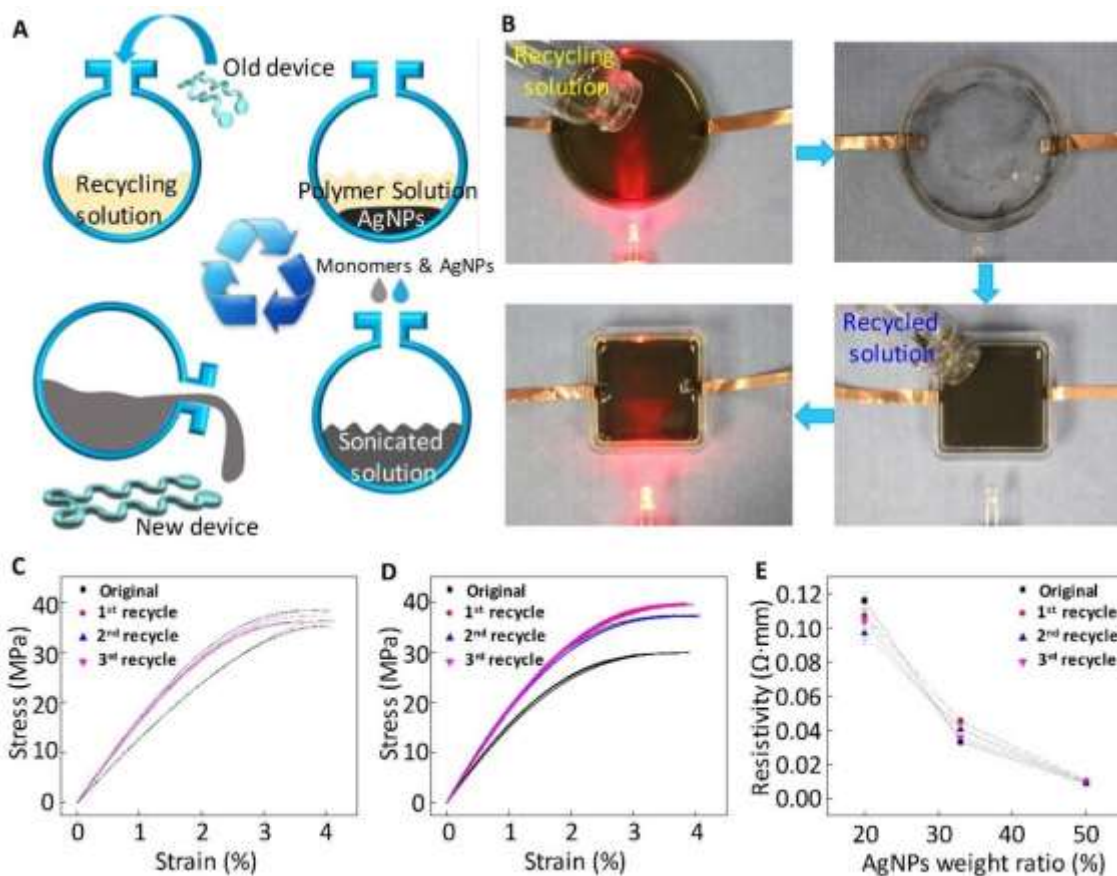


Figure 2.3. Recycling and characterization of the pure and conductive polyimine films. (A) Schematic illustration of the recycling process. (B) A LED light is on when a conductive polyimine film is connected into a simple lighting circuit (top left). After recycling, the LED light turns off (top right). The recycled solution is then casted into a new, square petri dish (bottom right). After polymerization, the film is conductive and the LED light turns on (bottom left). Uniaxial tension test results of the pure (C) and conductive (D) polyimine films before

and after recycling. (E) Electrical resistivity measurements of the conductive polyimine films before and after recycling.

The recyclability of such polyimine and AgNPs material system is then explored. The stoichiometric balance among aldehyde and amine groups (their reaction forming the imine linkage) within the polyimine network can be upset by introducing an excess of free primary amine groups (e.g. excess diamine monomer). Transimination reactions among the excess diamine monomers and the imine-linked network can lead to increased end groups within the matrix, thus reducing the molecular weight and solubilizing the network. Such a depolymerization mechanism could enable efficient recycling of the device consisting of dynamic covalent polyimine matrix and AgNPs. Figure 2.3A schematically illustrates the recycling process of a recyclable device. An old device is soaked in the recycling solution (ethanol and compound 2) (top left), and decomposes into oligomers/monomers and AgNPs. The oligomers/monomers are soluble in the solution, and AgNPs sink to the bottom (top right). After recycling, the solution and AgNPs can be either separated or mixed together to make new materials or devices. To completely reuse the recycled solution and AgNPs to fabricate new devices, compounds 1 and 3, and additional AgNPs are added proportionally and efficiently mixed (bottom right). After polymerization, the conductive polyimine can be used to fabricate new devices (bottom left, see SI for details). Figure 2.3B demonstrates the recycling of a conductive polyimine film. The LED light turns on when the conductive polymer is integrated into a simple lighting circuit (top left). Then the recycling solution is poured into the petri dish, causing decomposition of the polymer. After recycling is completed, the LED light turns off (top right). Subsequently, the solution and AgNPs are transferred out of the original circular petri dish, and poured into a different,

square petri dish (bottom right). Upon polymerization, the resulting film becomes conductive again, and lights up another LED light (bottom left). The recycling processes can be completed within 6 hours at room temperature without sonication or within 2 hours with sonication, and thus are very economical and eco-friendly (100% recyclable and reusable).

The stress-strain curves of pure polyimine films before and after up to three times recycling are compared in Fig. 2.3C. The Young's moduli and tensile strengths of the recycled films increase by 20% and 26% compared with the original films, respectively. This could be due to the increased crosslinking density (more complete reaction) by using recycled oligomers as the starting materials instead of small molecule based monomers. Figure 2.3D exhibits the comparison of stress-strain curves of conductive polyimine films before and after up to three times recycling. Similar increases in both Young's modulus and tensile strength are observed. Electrical resistivities of conductive polyimine films with 20%, 33% and 50% AgNP weight ratios before and after recycling are compared in Fig. 2.3E. The results indicate that recycling doesn't show noticeable influence on electrical resistivity of the conductive polyimine films.

To demonstrate the great potential of such polyimine-AgNP nanocomposites toward e-skin applications, we next utilized the conductive polyimine films to fabricate tactile, flow, temperature, and humidity sensors, which are then integrated onto a polyimine substrate to realize malleable, rehealable and fully recyclable e-skin. The design of the e-skin is schematically illustrated in Fig. 2.4A, and an optical image of the e-skin is shown at the bottom. Serpentine structures are adopted to minimize the influence of strains on the

performance of sensors. The tactile sensing is based on the capacitance change between two conductive element arrays (gray element arrays in Fig. 2.4A) separated by a dielectric polymer ring array (purple ring array in Fig. 2.4A). Figure 2.4B shows the performance of the tactile sensor. When two different balance weights (2 g and 5 g) are placed on the tactile sensor array (top left), both the weights and positions are detected by the sensor (top right). The relative capacitance change versus weight shows linear relationship (bottom left). Loading and unloading of a 13.2 g weight is also tested for 100 times to ensure repeatability (bottom right). Figure 2.4C exhibits the measured relative resistance change in the flow sensor versus flow rate at different currents. The measurement was conducted by controlling the water flow in a tube of diameter 10 mm, and the flow sensor was attached on the inner wall of the tube. As shown in Fig. 2.4C, the flow sensor can sense flow rates lower than 10 ml/s, beyond which the flow sensor doesn't change its resistance with increasing flow rate any more. And as expected, increasing current can effectively enhance the sensitivity. Characterizations of the temperature sensor is presented in Fig. 2.4D. The sensor resistance changes linearly with temperature between 24 °C and 54°C. The humidity sensor can sense humidity based on the plasticizing effect of water on polyimine. As water molecules diffuse into the sensor, the polymer network expands, leading to increase of the sensor resistance. Figure 2.4E presents the measured relative resistance change of the humidity sensor versus humidity between 15% and 80%, which shows quadratic dependency.

The average sensitivities of the tactile, temperature and humidity sensors can be obtained by calculating the average slopes of the curves in Figs. 2.4B, 2.4D and 2.4E, respectively. The sensitivity of the tactile sensor is 0.0067 kPa^{-1} , comparable to most of the other reported sensitivities of e-skins (10^{-4} kPa^{-1} to 0.5 kPa^{-1})[2]. The sensitivity of the temperature sensor is $0.17\% \text{ }^{\circ}\text{C}^{-1}$, slightly smaller than the previously reported e-skin ($<1\% \text{ }^{\circ}\text{C}^{-1}$). The average sensitivity of the humidity sensor is $0.22 \text{ } \%/%$, higher than the other reported humidity sensors on e-skins ($\sim 0.08 \text{ } \%/%$). The detection limits of the sensors are also indicated by the data shown in Figs. 2.4B-2.4E. For each tactile sensor, the detection limit is between 0 g and 14 g. Beyond 16 g, the deflection of the top conductive elements lead to their direct contact with the bottom elements and thus failure of tactile sensing. The flow sensor can detect water flow between 0 m/s and 10 m/s. For the temperature sensor, the detection limit is below $60 \text{ }^{\circ}\text{C}$, above which the active bond exchange reactions in the polyimine network lead to large variation of the resistivity of the conductive polyimine. For the humidity sensor, the upper limit of detection is about 80%-90%.

In addition to individual characterization, the sensing performance of the e-skin in a complicated environment combining air flow, humidity and pressure was tested. The results recorded by the flow, humidity and tactile sensors are shown in Figs. 2.4F, 2.4G and 2.4H, respectively. The air flow and relative humidity of the ambient environment were 10 m/s and 15%, respectively, and there were no weight applied on the tactile sensors. At stage1, constant air flow was applied on the surface of the e-skin. The flow speed recorded by the flow sensor was 3.6 m/s (Fig. 2.4F), the humidity sensor also recorded an increase of 2% in humidity due to relatively more humid air flow than the environment (Fig. 2.4G), the air pressure was also sensed by the tactile sensor, which was equivalent to 0.15 g (Fig.

2.4H). Afterwards, the air flow was turned off, the flow, humidity and tactile sensors went back to the original states. At stage 2, a moisture generator was used to spray moisture on top of the e-skin. The flow sensor gave the flow speed to be 0.59 m/s (Fig. 2.4F), and the relative humidity sensed by the humidity sensor increased to 67% (Fig. 2.4G). Because the air pressure was very small, the tactile sensor didn't give readable values (Fig. 2.4H). At stage 3, the moisture generator was turned off, and several screw nuts were placed on top of the e-skin. The central tactile sensor element gave the weight put on top of it to be 2.1 g (Fig. 2.4H), while the flow and humidity sensors didn't show any changes (Figs. 2.4F and 2.4G).

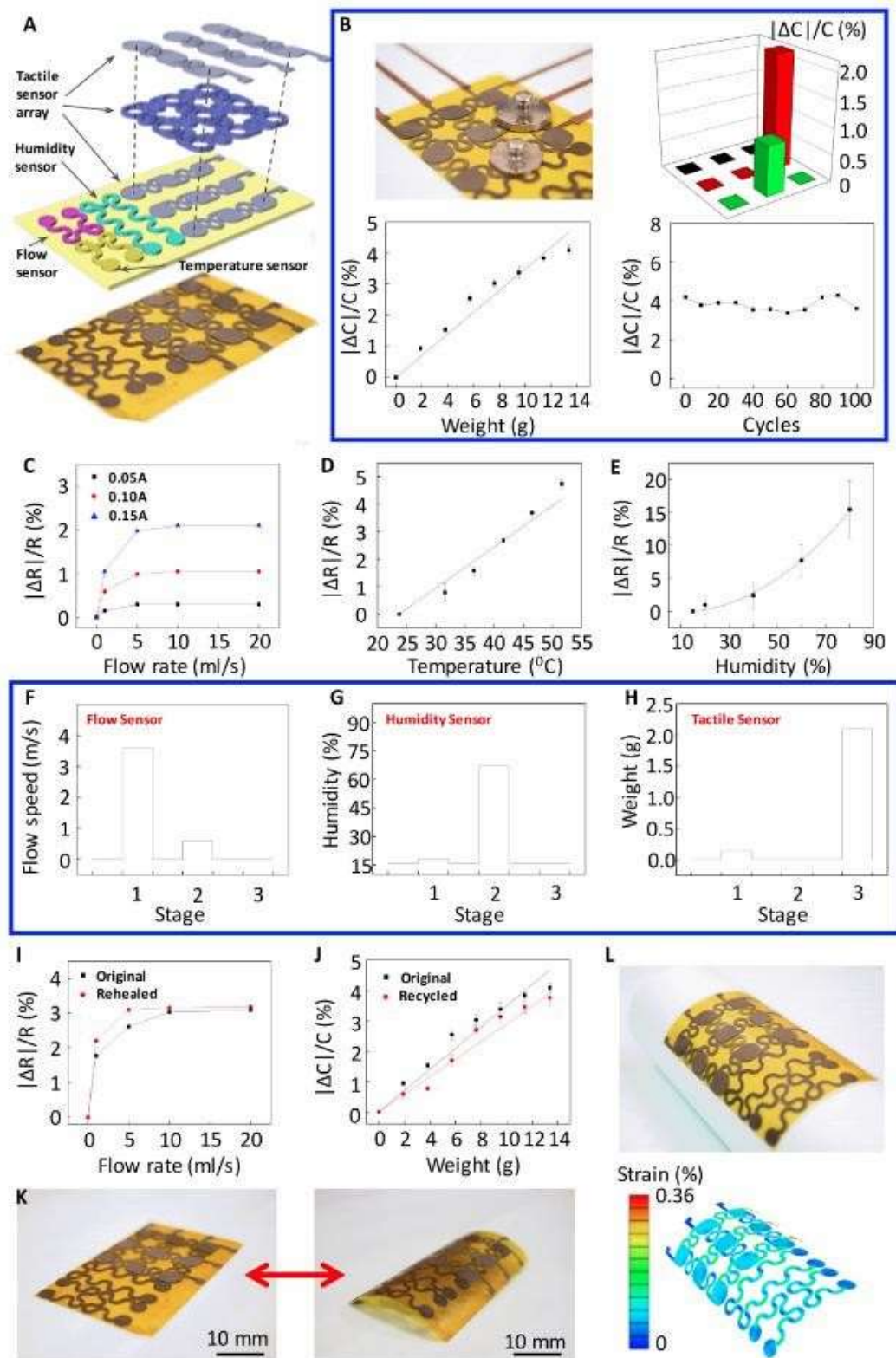


Figure 2.4. Characterization of the rehealable, fully recyclable and malleable e-skin.

To demonstrate the rehealing capability of the e-skin, the flow sensor is cut broken, and then rehealed using the process described previously. As shown in Fig. 2.4I, the rehealed flow sensor regains its flow sensing capability, which is comparable to the original sensor before cutting. Recycling of the tactile sensor is also demonstrated. Figure 2.4J compares the sensing characteristics of the tactile sensor in its original form, and after recycled. The recycled tactile sensor shows similar sensing performance compared with the original tactile sensor. The slight reduction in sensitivity is probably due to the slight increase in Young's modulus of the recycled conductive polyimine film, as shown in Fig. 2.3D.

The e-skin is not only rehealable and recyclable, but also flexible and malleable. By applying moderate heat (60 °C), the flat e-skin (Fig. 2.4K, left) can be deformed into a curved shape. After cooling down and removing the applied force, the e-skin stays at its deformed, curved shape (Fig. 2.4K, right). This process is reversible and repeatable. Such property renders the e-skin excellent capability in matching with complex geometries, without incurring high stress buildup at the interface. Figure 2.4L shows the e-skin is bended around a cylinder of radius 100 mm. Finite element simulation results give the strain distribution in the deformed e-skin. The maximum strain in the deformed e-skin is 0.36%, much smaller than the failure strain of the conductive polyimine.

2.3 Materials for polyimine E-skin

Material preparation. The polyimine was synthesized by mixing terephthalaldehyde (1, 0.8 g, 5.96 mmol), diethylenetriamine (2, 0.184 g, 1.79 mmol), and tris(2-aminoethyl)amine (3, 0.407 g, 2.78 mmol) in ethanol. The solution was vigorously stirred and poured into petri dish coated with PDMS, followed by evaporating in a fume hood for 12 hours at room temperature and heat-pressing at 80 °C and 8.5 kPa. The conductive polyimine films were prepared by mixing the same compounds as described above and silver nanoparticles in ethanol. The solution was sonicated for 2 hours and poured into petri dish coated with PDMS, followed by evaporating in a fume hood for 12 hours at room temperature and heat-pressing at 80 °C and 8.5 kPa. Detailed polymer structure is shown in Fig.2.5.

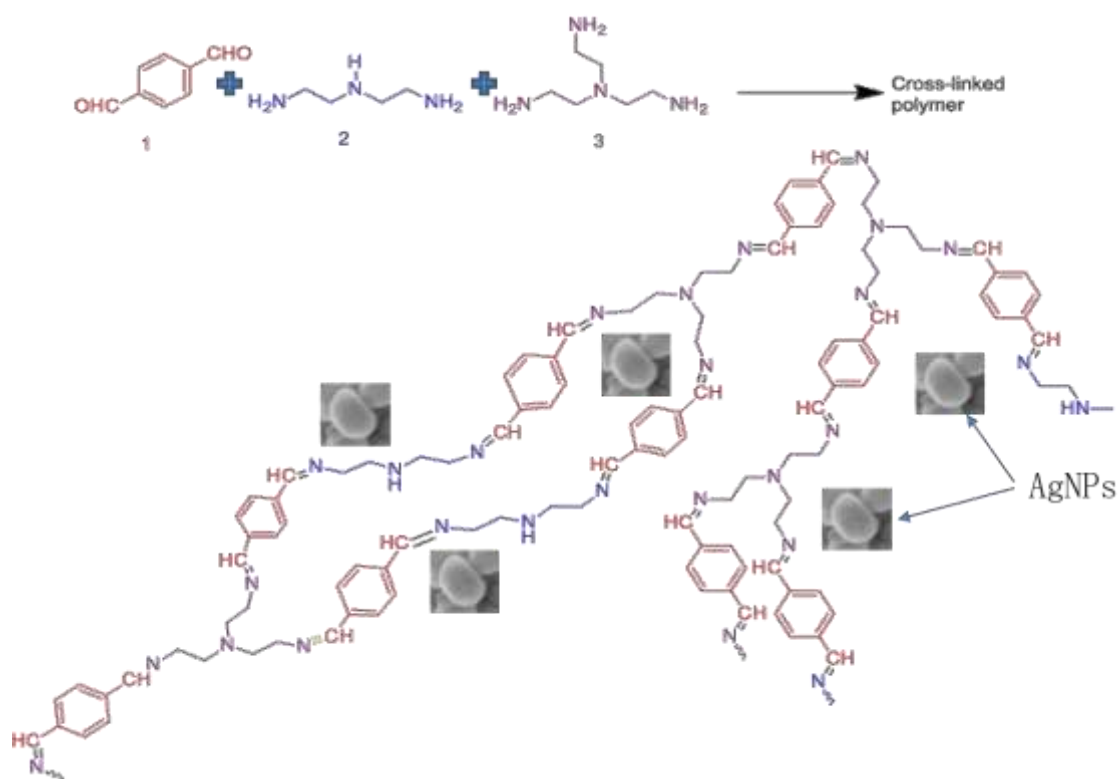


Figure 2.5. Polymerization of polyimine networks

Rehealing and recycling process. To reheat both the pure and conductive polyimine films, a small amount of rehealing agent was added to the crack, followed by heat-pressing at 80 °C and 8.5 kPa. To recycle the pure and conductive polyimine films, 1 equivalent diethylenetriamine (2, 0.046 g, 0.448 mmol), and 1 equivalent tris(2-aminoethyl)amine (3, 0.102 g, 0.685 mmol) were firstly added to dissolve the polyimine film. Then terephthalaldehyde (1, 0.2 g, 1.49 mmol) was added into the solution for polymerization. For conductive polyimine nanocomposites, extra silver nanoparticles were added to adjust the weight ratio of the mixture.

Mechanical test. The mechanical tests were carried out using an INSTRON mechanical testing system. Testing samples were cut into dog-bone shapes with a laser cutter.

Characterization of sensors. To characterize the temperature and flow sensors, four point measurement was adopted to measure their resistance change. A current supplier (HY3005M-3 Digital Control) was used for the current input, and an oscilloscope (KEYSIGHT DSO-X 2004A) was used for measuring the voltage. A constant current of 10 mA was applied on the temperature sensor, while three different current values (0.05A, 0.1A, 0.15A) were applied on the flow sensor for characterization.

The temperature sensor was encapsulated with Kapton tape and soaked in water bath. The temperature of the water bath was controlled using a temperature controller (INKBIRD TECH.C.L).

The flow sensor had the same design as the temperature sensor and was also encapsulated with Kapton tape. The integrated sensor was then inserted into a rubber tube of diameter 10 mm, as shown in Fig. 2.6. A pump was used to supply water which flows through the tube, and the speed was controlled using a valve. While the flow speed is calculated by measuring flow volume within one minute.

The humidity sensor was characterized within a chamber. The humidity was controlled by placing saturated solution of potassium acetate, magnesium nitrate, and sodium chloride at the bottom of the chamber. The solutions ensure the stabilized humidity within the chamber to be $21\pm 2\%$, $40\pm 2\%$, and $60\pm 2\%$, respectively. The humidity values of $16\pm 2\%$ and $80\pm 2\%$ were controlled using calcium chloride and distilled water. Four-point measurement was used for testing the resistance change.

The tactile sensor array was based on capacitance change between the two conductive element arrays separated by the dielectric polymer ring array. A capacitance meter for ultra-low capacitance measurement (Excelvan M6013) was used for the measurement of the capacitance change.

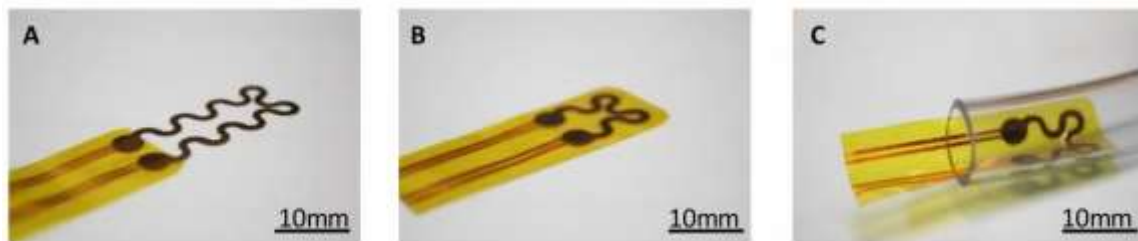


Figure 2.6. Optical image of humidity sensor (left) and flow/temperature sensor (right).

Fabrication of sensors. The sensors were fabricated from the conductive polyimine sheets with 33% AgNP weight ratio. A laser cutter was used to cut the serpentine structures out of the sheets.

The flow sensor, humidity sensor and temperature sensor were designed with serpentine structures to minimize the influence of strains due to the deformation of the whole device. When the sensors were fabricated, silver conductive adhesive was used to connect them to the external conductive wires for measurement. To test the flow sensor, it was attached on the inner wall of a tube of diameter 10 mm, with water flow controlled by a valve. The temperature sensor was characterized in water bath to better control the temperature. To seal both flow and temperature sensors, Kapton tapes were used for encapsulation.

To fabricate the tactile sensor array, two arrays of conductive elements interconnected by serpentine were fabricated from conductive polyimine sheets, as shown in Fig. 2.4A. An array of dielectric rings of thickness 20 μm was cut from a pure polyimine sheet, as shown in Fig. 2.4A. The dielectric ring array was sandwiched between the two conductive element arrays, and good alignment was ensured. Then heat-pressing for 10 minutes (1 KPa and 80 $^{\circ}\text{C}$) bonded the three layers together due to dynamic covalent bond exchange reactions at the interfaces.

Characterization of sensors under bending. The sensors were bended on top of a cylinder of diameter 70 mm. Testing methods described above were used for characterizing the

sensors. The testing results are shown in Fig.2.7. After bending, the sensing properties of the sensors remain similar to those in their flat states.

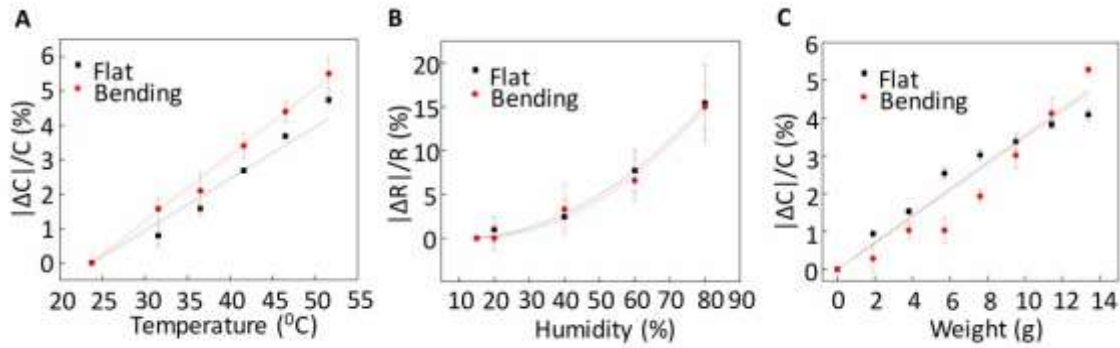


Figure 2.7. Characterizations of temperature sensor (A), humidity sensor (B) and tactile sensor (C) under bending, and comparison to the flat state.

Chapter 3

Investigating the rehealability of polyimines and their nano-composites

3.1 Self-healing materials

The self-healabilities of the natural skins of animals and plants are taken for granted, however, achieving healable smart and soft materials remains a challenge, and is significant for the applications of flexible electronics and artificial skins. Mimicking the existing self-healing functionality of many organisms[68]–[70], various of studies have been carried out for recent decades.

Depending on the required stimuli and the nature of the self-healing process, self-healing materials can be divided into autonomic and non-autonomic materials[15], [51]. Autonomic self-healing materials automatically respond to damage without any requirement of force applied, hydrogen bonding, for example[72]. In contrast, non-autonomic self-healing materials need modest external stimulates, like heat [73]–[77], chemicals[78]–[81], light[82]–[85], pressure[60], [78], water[86]–[88], and so on. Currently, polymers and composites are widely studied materials in self-healing materials. Covalent dynamic bonds in polymer networks usually offers more robustness, tunable mechanical and electrical properties and bridge the gap between thermoplastics and thermosets. Heat treatment, in

this case, is a well-adopted method for self-healing polymers[89], Philp and co-workers demonstrated a series of polyimine thermosets and composites which can be rehealed and recycled by thermal stimuli[11], [67], [90]. A straightforward and practical way to make polymers conductive is to physically mix conductive materials into the network, such as silver nano-particles (-wires), carbon nanotubes and liquid metal. Various applications of such strategy can be found in flexible electronics, optical devices, and artificial skins[90]–[92], as well as skin sensors[10], frequency antennas[93], stretchable wires[60], and artificial muscles[94].

Previously, we reported a rehealable, recyclable and malleable electronic skin, which is based on the polyimine and its Silver nano-particle composites[80]. The rehealability is triggered by solution, water, or heat. follow-up studies reveal that the rehealing behavior is affected by loads, times, temperatures and AgNPs weight ratios as well. In this paper, we present how these conditions affect the rehealing of polyimines. A simple test procedure is presented for three AgNPs weight ratio (0, 20%, 50%) composites. After healing, the conductivity and shear strength of rehealable specimens were observed to quantify rehealing capability. Microscopy images described healing cracks and failure interfaces of rehealable polyimine films.

3.2 Characterization of the rehealability of polyimine

Pure (composite) polyimine networks were prepared from commercially available monomers. A mixture of diethylenetriamine (0.092g, 0.895mmol) and tris(2-

aminoethyl)amine (0.204g, 1.39mmol) was dissolved in ethanol (5mL) and added to a 20 mL screw cap. Silver nanoparticles in different weight percentages (0%wt 0g, 20%wt 0.348g, 50%wt 0.696g) were added into the vial and sonicated for 3 hours. Then, terephthaldehyde (0.4 g, 2.98mmol) was added into the vial, and the mixed solution was poured into a petri dish coated with PDMS. The solvent was then allowed to evaporate 12 hours in a fume hood under ambient conditions. The detailed rehealing process of a pure (composite) polyimine film is schematically illustrated in Fig. 3.1B, with optical images of the pure polyimine film shown at the bottom of each frame. A virgin polyimine strip (0.15mm*3.5mm*36mm, Fig. 3.1B, top left) was cut broken along its width direction (Fig. 3.1B, top right). By overlapping cut area with 2mm long and heat pressing (Fig. 3.1B, bottom right), the lapped interfaces are rehealed (0.15mm*3.5mm*34mm Fig. 3.1B, bottom left). In all cases, the overlapped polyimine films were heat-pressed at different times, temperatures and loads before being subjected to various property tests.

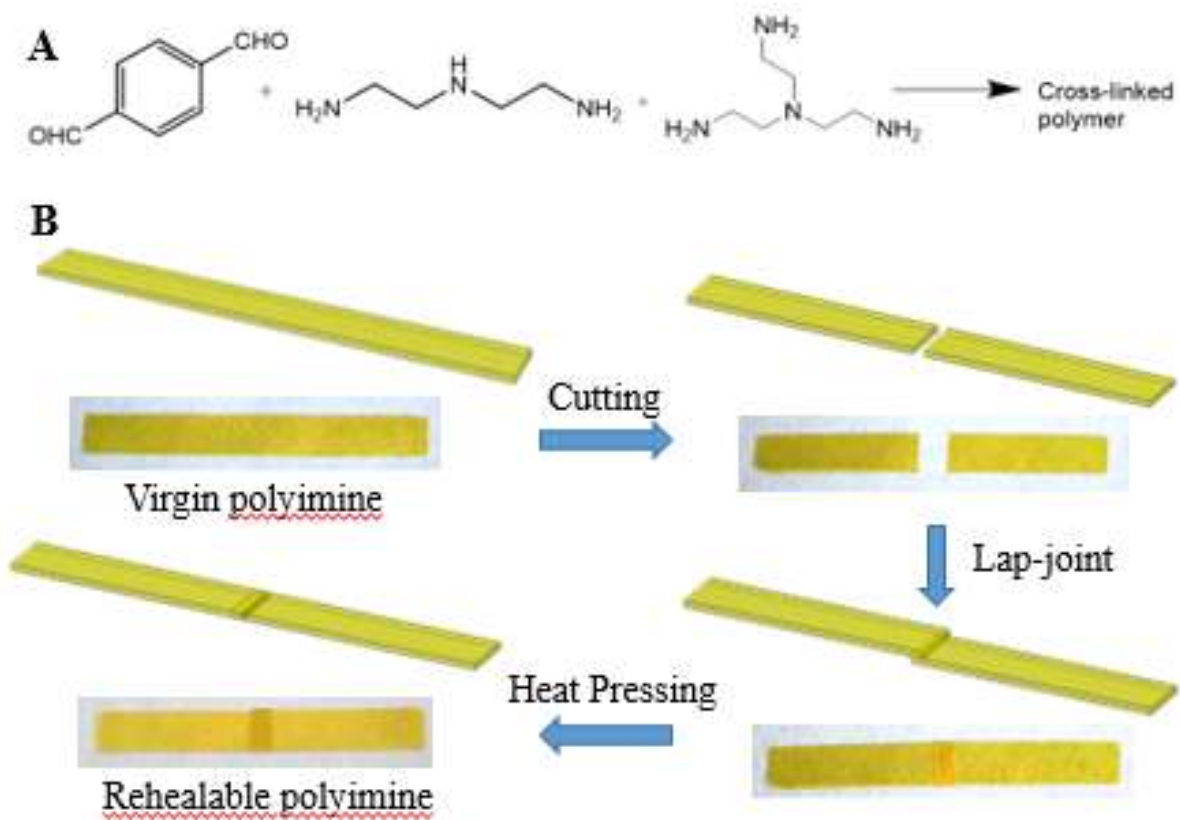


Figure 3.1. Polymer synthesis and rehealing process. A) Synthesis of crosslinked polyimine.

B) Schematic illustration of preparation process of rehealable polyimine. Optical images of the polyimine film are shown at the bottom of each frame.

The optical microscopy images (Fig. 3.2) are cross-section views of overlapped areas, showing the gap size between interfaces at different stages of the rehealing process. The gap at the left of each frame initially has a width of $\sim 20 \mu\text{m}$ and gradually becomes invisible after being rehealed. We obtained a discernible trace of interfaces after 5mins, 80°C and 500g loading heating (middle left of each frame in Fig. 3.2), and the interfaces are not entirely rehealed, but three weight ratios of rehealable polyimine strips are firm enough to hold 1g weights (right of each frame in Fig. 3.2). After heat pressing for 65mins with 80°C temperature and 500g loading, traces of the interfaces completely disappear (middle right of each frame in Fig. 3.2) because of sufficient polymerization of monomers/oligomers under extended time. Traces change similarly at different temperatures and loads. Correspondingly, the rehealed specimens can easily lift the 1g weight at lower temperatures and loads.

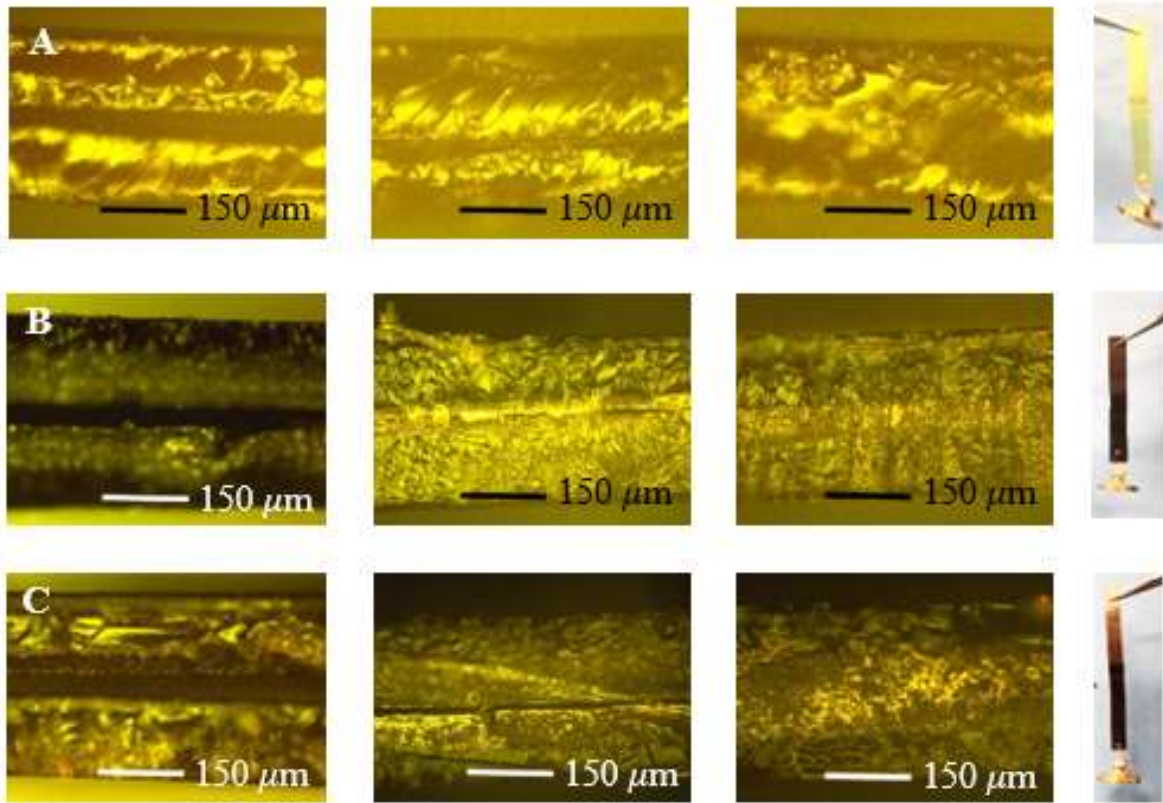


Figure 3.2. *Optical microscopy images of the cross-section view of lap-joint polyimine films. A) Optical image of a pure polyimine film. B) 20% AgNPs conductive polyimine film. C) 50% AgNPs conductive polyimine film. Gaps between interfaces before rehealing are on the left of each frame. Crack traces after 80°C, 500g, 5mins heat pressing (middle left of each frame). Invisible traces after 80°C, 500g, 65mins heat pressing (middle right of each frame). Rehealable polyimine strips hold 1g weight after 80°C, 500g, 5mins heat pressing (right of each frame).*

A uniaxial tension test is conducted to compare the mechanical properties of pure and conductive polyimine films with different heat pressing conditions. To test the rehealing effects of overlapped interfaces, shear failure of a lap-joint area should become the primary failure mode in the uniaxial tension test by recording failing loads per shear area[95]. As shown in Fig. 3.3A, long (~0.3mm*3.5mm*17mm) and short (~0.45mm*3.5mm*3mm) aluminum alloy plates were stuck to both sides of rehealable polyimine strips. Aluminum alloy plates could increase tensile strength and avoid the tensile failure of test samples, as well as adjust the loading axis to be consistent with the center line of the specimens. Fig. 3.3B-3.3D compare failure interfaces between pure and composite polyimine films after uniaxial tension tests, with optical images of the failure interfaces shown at the bottom of each frame. On the left of the images in each frame, optical microscopy shows no visible breach of failure interfaces after 5mins heat pressing. The interfaces are partially rehealed and bond exchange of the interfaces polymerized insufficiently, so there is no damage of overlapped interfaces. In contrast, all interfaces are broken after tensile testing when loading samples with 65mins heat pressing (right image of each frame), probably because monomers/oligomers have sufficient polymerization with longer heat pressing time, and the interfaces would heal more entirely to an integrated film after an extended time. Therefore, the failure mode of the interfaces is not only shear failure but also a tensile failure.

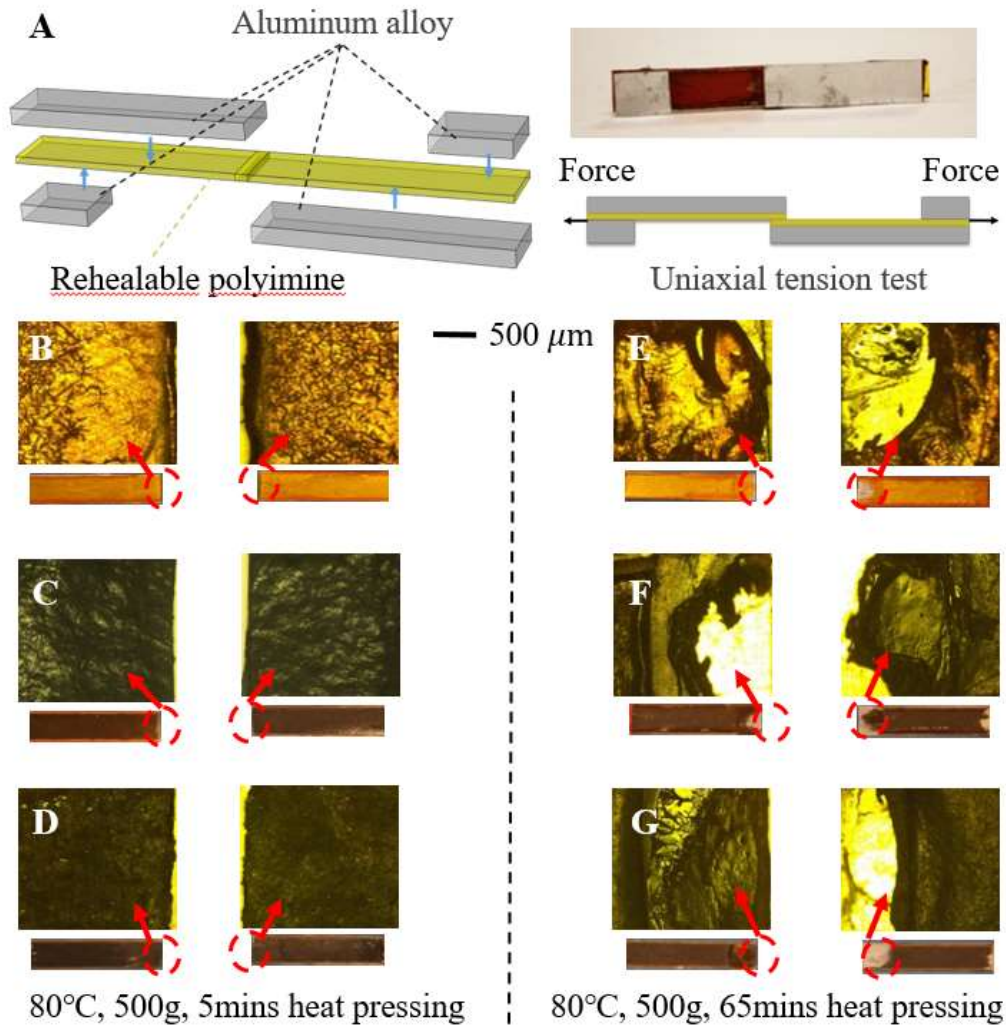


Figure 3.3. Uniaxial tension test specimen and optical microscopy images of failure interfaces after tests. A) Schematic illustration of uniaxial tension test specimen. An optical image of the specimen is shown at the top right. Front view of specimen at the bottom right. B) and E) Optical image of pure polyimine failure interfaces. C) and F) 20%wt AgNPs composite polyimine failure interfaces. D) and G) 50%wt AgNPs composite polyimine failure interfaces. B)~D) Rehealable polyimine specimens at 80°C, 500g, 5mins heat pressing show no visible fracture of failure interfaces (the images on the left frame). E)~G) Rehealable polyimine specimens at 80°C, 500g, 65mins heat pressing illustrate breach of failure interfaces (the images on the right frame).

The results of uniaxial tension test are illustrated in Fig. 3.4, which compares interface shear strength of pure and composite polyimine films when changing heat pressing conditions in different times, temperatures and loads, respectively. The shear stress expresses all failure loads in Newton per square millimeter of the overlapped area, while shear strength is the maximum of shear stress (Fig. 3.4)[95]. A wide range of shear strength was observed for the polymer films heat pressed in different conditions. Shear strengths rose with heat pressing loads ranging from 50 g to 1100 g, but there was no rehealing under 50g loading for composite polyimine with 50% AgNP weight ratio, on account of AgNPs impeding bond exchange reaction, especially under lower loads (Fig. 3.4A). Similarly, shear strengths also went up as temperature and time increased (Fig. 3.4B, 3.4C). Meanwhile, shear strengths of pure polyimine are higher than those of composite polyimine under the same conditions (0 > 20%wt > 50%wt AgNPs), which means that improving the electrical conductivity of polyimine must sacrifice the extent of its ability to reheat. The pure, rehealable polyimines at 1100 g, 115 °C and 65 mins conditions exhibit significantly higher shear strength, 9.4 MPa, 13.2 MPa, and 9.8 MPa, respectively, compared to the samples prepared under other conditions.

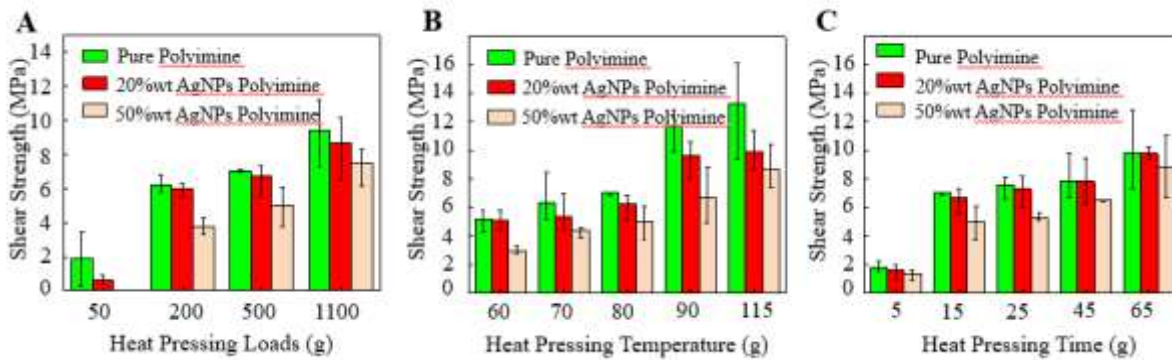


Figure 3.4. Shear strength of rehealed interfaces of polyimine specimens. A) Shear strength bar charts of rehealed interfaces in different loads B) Shear strength bar charts of rehealed interfaces in different temperatures. C) Shear strength bar charts of rehealed interfaces in different times.

The characteristics of composite polyimine conductivity are illustrated in Fig. 3.5. The LED light turns on when a strip of conductive polyimine is integrated into a simple lighting circuit (Fig. 3.5A). When the polyimine sample was cut in the middle, it caused the circuit to disconnect and the LED to turn off (Fig. 5b top right). After heat pressing the polyimine for 5 mins, 500g and 80°C, the LED light turned on again (Fig. 3.5B bottom). Electrical resistance ratios of conductive polymer films with 20%wt and 50%wt AgNPs are compared in Fig. 3.5C and the resistance of the samples obtained using four-point measurement are $\sim 6\Omega$ and $\sim 1\Omega$, respectively. Resistance ratio is the resistance of virgin polyimines divided by that of rehealed polyimines at the same sample length of 20mm. The smaller the value is, the stronger the conductivity will be after rehealing. The range of error bars at 5mins, 50g and 60°C are larger compared with the error bars of other data, that is because the polymer

interfaces only have a small part of healing, and the conductivity of AgNPs changes significantly under a small rehealing area. It appears that most rehealed films have better conductivity than virgin films because heat pressing could make the conductive polymers more compact and bring the silver nanoparticles closer together. The results indicate that with the rise of temperature, pressure and time, the conductivity of rehealed films increases. Consequently, 50% wt AgNPs polymer films have better conductivity than 20% wt composite polyimines after the same heat pressing procedure.

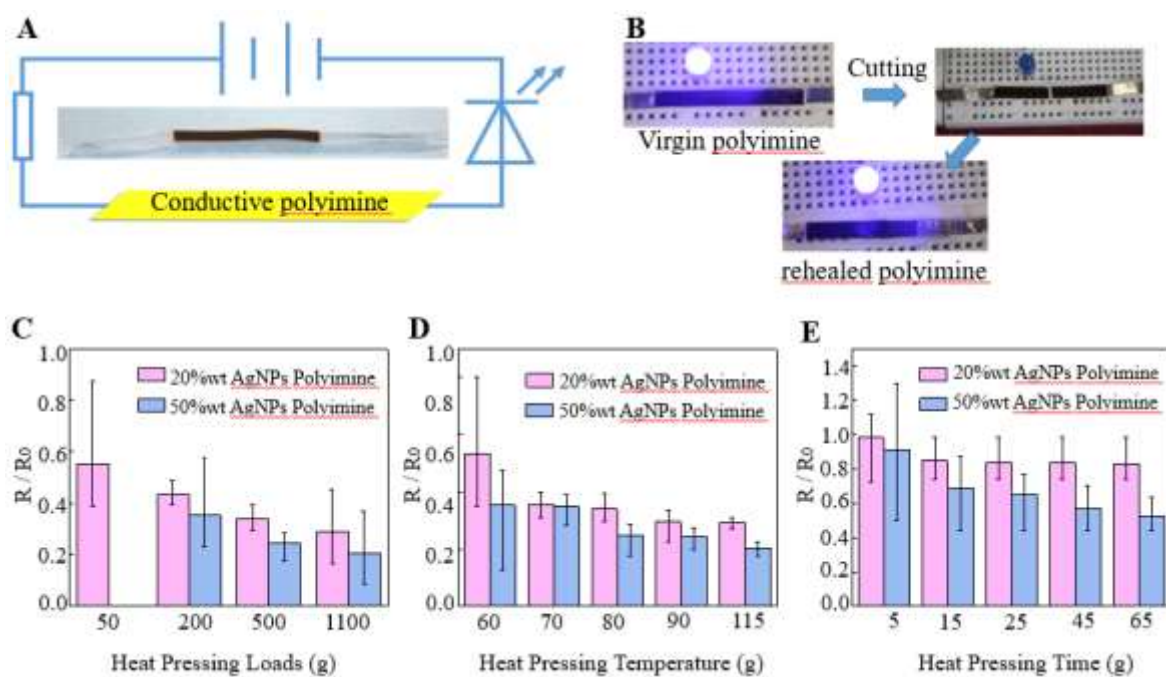


Figure 3.5. Characterization of conductive polyimines. A) Lighting circuit of conductive polyimine. B) An LED light is turned on with a virgin polyimine and the rehealed one. C)~E) Comparison of resistance ratio of rehealable polyimines in different loads (left), temperatures (medium) and times (right).

3.3 Measurements and testing methods for polyimines

Uniaxial tension test of polyimine films. Both pure and conductive polyimine films were tested using an INSTRON mechanical testing system. Uniaxial tension load with loading speed of 0.4 %/min was used for static tension test. The testing samples were prepared in the shape of Fig. 3.3A (0.15mm*3.5mm*34mm), by cutting polymer sheets with a laser cutter (Lide laser cutting machine). then stretched under a constant loading speed until interface broke.

Resistance test of conductive polyimine films. Four point measurement was adopted to measure their resistance change. A current supplier (HY3005M-3 Digital Control) was used for the current input, and an oscilloscope (KEYSIGHT DSO-X 2004A) was used for measuring the voltage. A constant current of 10 mA was applied on the composite polyimine films.

Analysis of front section view about rehealed polyimine films. Optical microscopy images of the lap-jointed areas before and after self-healing process from front section view in Fig. 3.6. Lap-joint areas before heat pressing are schematically illustrated in the middle of each frame, with a visible boundary line in the magnified views. And due to the inconsistent height of the overlapped layers, the microscope can only focus on the right part of each layer. On the contrary, the left part of each layer is blurred. After heat pressing under 80°C temperature, 500g loading for 65mins, the overlapped areas are rehealed (on the right of each frame), and both sides of layers are visible. The traces of boundary after heat pressing of composite polyimine (middle and right figures of Fig. 3.6B and 3.6C) are more evident than that of pure

polyimine (right of Fig. 3.6A) because the presence of AgNPs negatively affects bond exchange reaction in the polyimine especially for the boundary of interfaces.

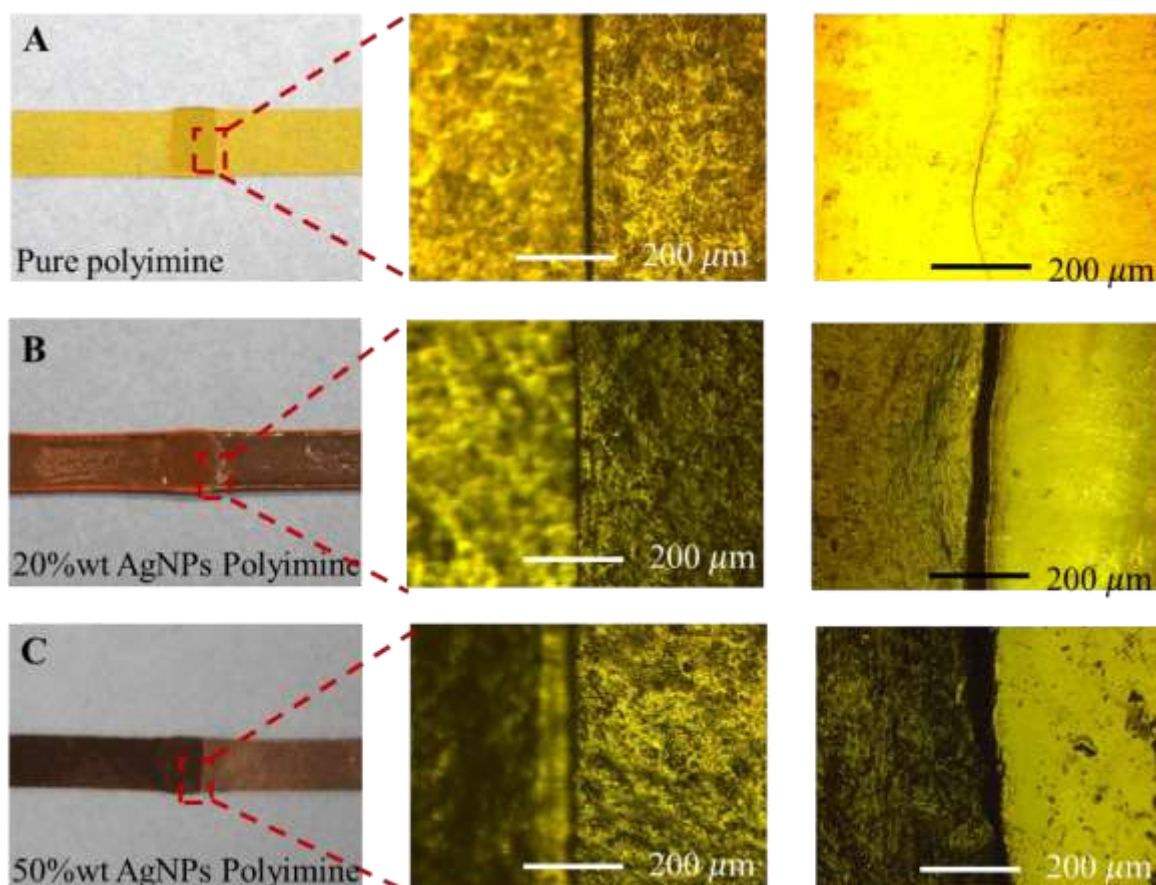


Figure 3.6. *Optical microscopy images of the top view of lap-joint polyimine films. A) A pure polyimine film. B) 20%wt AgNPs composite polyimine film. C) 50%wt AgNPs composite polyimine film. Optical images show lap-joint area (left of each frame). The magnified views on the middle frame show lap-joint cracks before self-healing. The optical microscopy images on the right show cracks after heat pressing at 80°C, 500g for 65mins.*

In conclusion, heat pressing conditions and AgNP weight ratio affect polyimine reheatability and conductivity. A range of interface shear strengths of overlapped films were obtained in different heat pressing states. Temperature, pressure and time directly influence the reheatability of these polyimines. AgNPs could also change bond exchange reaction rates, thus higher weight ratios of AgNPs influence the rehealing process of polyimines. We also demonstrated the conductivity of rehealed polyimine under different heat pressing conditions, composite polyimine films with higher AgNP weigh ratios have better conductivity and weaker reheatability. Pure polyimine films have better reheatability, but conductive polyimines have more functional applications, like in strain and thermal sensors. Hence, conductive polyimine have a more comprehensive application prospect after enough rehealing polymerization by enhancing the heat pressing conditions.

Chapter 4

Bio-memetic camouflageable surfaces enabled by Liquid Crystal Elastomer

4.1 Current researches about artificial camouflage

For naturally selected animals and plants, camouflage is a basic skill to survive every day. Big cats with stripes and dots hide in the bushes waiting to ambush, chameleons blend into colorful tree branches, and octopus change their skin textures to mimic anything from a sea rock to sea plants. Nature always inspires scientists and engineers to seek the best solutions. Soft robotics, as a hot topic, has attracted the attention of many researchers from different backgrounds [96]–[107]. However, helping soft robots blend into their surroundings remains a challenge. Color change was easily accomplished [105], but complex, programmable, and reversible texture shifting of soft robots' skin is more difficult to handle. In nature, animals have dedicated muscle system for supporting such functions. Pneumatic actuation of soft silicone materials is successfully introduced to develop a camouflageable skin[108]. A more straightforward mimicking of natural muscle tissues for camouflaging purposes is still on the way to explore.

Biological muscle contracts under stimulation, and thus interacts with its surrounding tissues. Localized and miniature pattern control is efficiently realized on such a platform. Liquid Crystal Elastomers (LCEs) exhibit the most similar actuation behavior to natural muscle, due to their dramatic contraction, reversible deformation, response to multiple stimuli, and great potential for micro-scale robotics[109]. Combing liquid crystal orientation and cross-

linked polymer networks, LCEs have attracted much attention towards creating artificial muscles[46]. The reversible change in chain formation due to a shift in temperature leads to macroscopic deformation. Alignment prior to actuation is critical for LCE actuators. Various methods have been considered including taking advantage of diamagnetic and dielectric anisotropy of mesogens, which is limited to certain monomers and requires large magnetic fields. Surface patterning, achieved by such means as rubbing with a cloth, is adopted as well, but limited to thin membranes (<100 um). Mechanical alignment is the most widely used option due to its convenience and ease of operation, offering the most potential for LCE actuators to mimic the large, linear actuation of natural muscle tissues. Stimulating the aligned LCEs also remains a challenge. Introducing a dye into the LCE network to enable a response to light proves to be a good method, but is confined to certain formulas and difficult for precise unit controlling. In other cases, heaters were adhered to the surface of aligned LCE layers [Yu kai paper, soft matter] to trigger phase disorder of the aligned LCE sheet, but this method was limited to small local strain and bending deformation. Embedding heaters into the LCE material could efficiently enhance the heat transferring from the heaters to the LCE network and enable linear actuation closer to natural muscle tissues. Unfortunately, conventional heaters based on solid metal and composite materials could be damaged under large alignment strain (up to 600%). A Liquid Metal (LM), however, could handle such deformation without any problem, and is especially suitable for LCE alignment. Further, LM heaters would introduce almost no extra confinements to the active polymer network, owing to their fluidic properties above a certain temperature. LM, at the same time, has been proved to work as very sensitive strain sensors[38]. A self-sensible actuator thus can be achieved easily on such system.

In this work, we choose an LCE network based on a two-stage thiol–acrylate reaction, and embed patterned LM heater (99.99% Gallium, Amazon) directly into the LCE network. The LM heater deforms with the LCE network during alignment with no damage. Linear actuation, bending, and twisting are easily realized with this system. Gallium (melting at 30°C) was chosen as the material for the LM heater and patterned using stencil methods. The LM heater not only remain robust during actuation but also does not confine the deformation of LCE networks. Large linear strains over 100% can be realized, which is much higher than natural muscle. Inspired by biological tissue, passive and active materials are then combined as a system, mimicking dramatically changing surface patterns. Taking advantage of the sensing capability of LM heaters, a self-sensible soft walker is also realized.

4.2 Fabrication and characterization of the Artificial Muscle

We embedded the LM (Gallium) into an LCE network to mimic the performance of natural muscular tissues. The LCE/LM artificial muscles (LLAMs) were fabricated layer by layer, as shown conceptually in Fig.4.1A and Fig.4.2B. The LM heaters (250um thick) were patterned on top of a 3M VHB layer (25um thick) utilizing stencil methods. The VHB layer was used as an adhesion medium and could thus firmly hold the LM heater patterns. The thin layer of VHB only slightly affects actuation due to its much thinner thickness. We achieved a low characteristic cross-section aspect ratio for the LM heaters to avoid the collapse of fluidic channels when the system undergoes large deformations. A liquid LCE layer (500um thick) was then cast on top of the LM heater patterns and allowed to cure at

80 °C for 24 hours. After the first stage of cross-linking, the LCE layer adhered to the VHB surface and LM heaters very well and formed a liquid channel. The sandwiched structure was then stretched with 100% uniaxial strain and further cross-linked under UV light (365nm wavelength) for 15 minutes. In the first example (Fig. 4.1A), we fabricated a LLAM with a length of 10mm, a thickness of 1.2mm and a width of 2.5mm. Two LM heaters were embedded on each side of the VHB layer. When a current (5A) goes through either one of the heaters, the LLAM bends toward that side. With current running through both heaters, the LLAM shrinks, as shown in Fig.4.1A, on the right. Both bending and linear actuation can thus be achieved on a single actuator using simple patterns, as shown in Fig.4.1A. We measured a smallest bending radius of about 10mm, and a linear contraction of about 45%, which is much higher than that of biological muscle and other forms of soft actuators. It should be noted that the optimal linear actuation strain can be further enhanced if a larger pre-stretch is introduced during alignment.

For a second example, a simpler actuator (with a length of 10mm, a thickness of 0.6mm and a width of 2.5mm) was fabricated using only one LM heater embedded in the LCE network (Fig. 4.1B), with a thickness of 500 um. The alignment direction was slightly biased, as shown in Fig. 4.1B, on the right. The LLAM primarily twisted when the LM heater was engaged, with a twisting angle of over 90⁰, comparable to other means but based on a simpler design. The twisting deformation occurred due to a bias alignment and thermal gradient within the LCE/LM composite layer, easily realized on our platform. Further, after more than 15 seconds of heating, we observed that the twisting stopped and linear shrinking

started to dominate. To stabilize the twisted state, one option was to shift the applied current down from 5 A to 2.5 A.

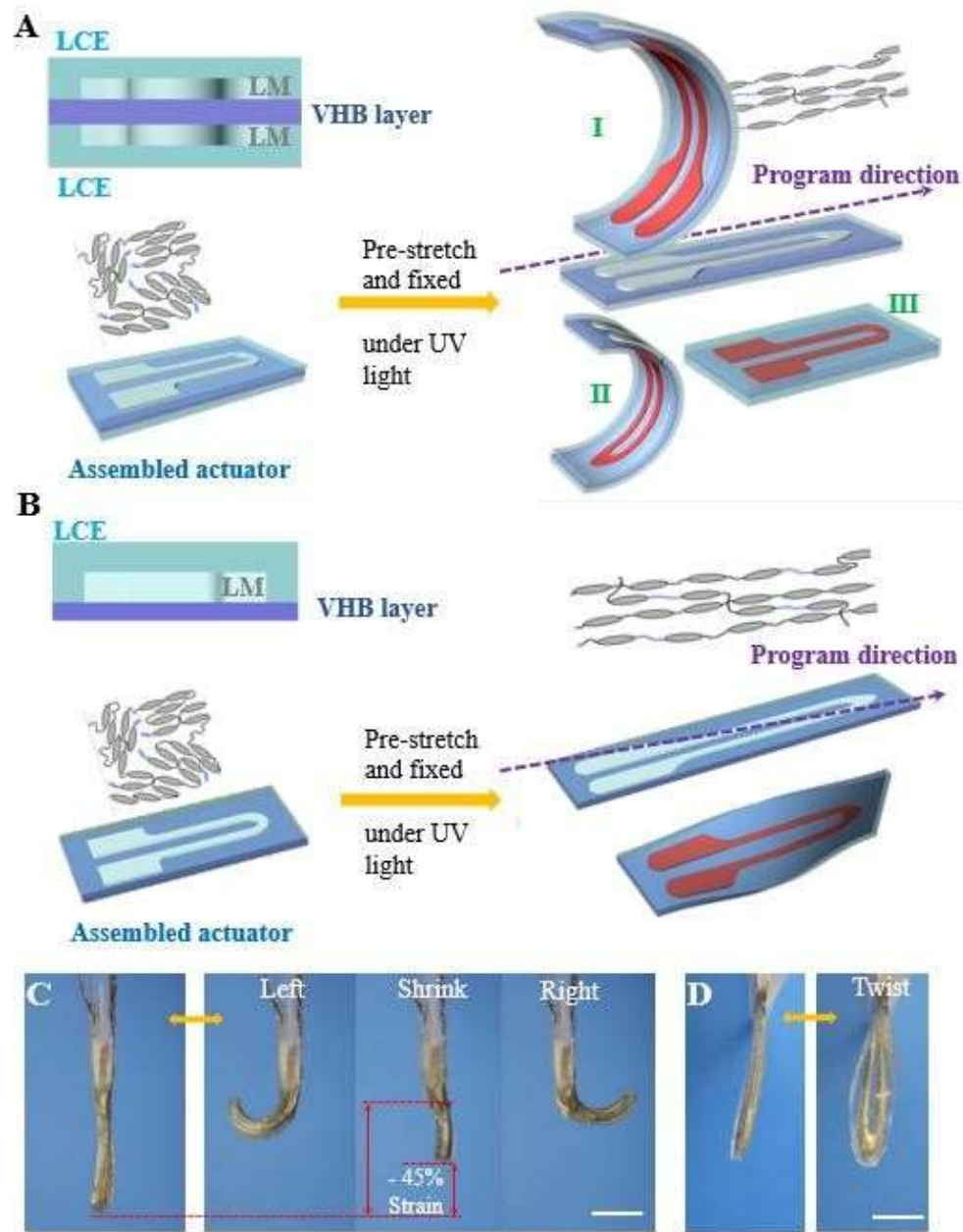


Figure 4.1. Conceptual demonstration and experimental results of LLAM. (A,B) Conceptual design about the LCE/LM actuator. Liquid metal was patterned on eachside of

the VHB layer and encapsulated with liquid LCE. After 1st stage polymerization the LCE/LM actuator was pre-stretched and further polymerize under UV light. Finally the actuator can perform bending, and shrinking. (C) Experimental Images of the LCE/LM actuator, which can bend and shrink. And obtains a maximum shrinking strain of 45%. Scale bar is 5mm.

Mechanical analysis of the LM heater channel and a heat transfer simulation of the LLAM were carried out, as shown in Fig. 4.2A and Fig. 4.2B, respectively. Compared to a solid metal, LM can undergo ‘infinite’ deformation without damage. In the LLAM, the LM heater deformed along with the fluidic channel during alignment (Fig. 4.2A middle), experiencing 69% to 96% strain, indicated in Fig. 4.2A, on the right. Solid metals, on the other hand, cannot withstand such deformation during LCE alignment. In the case of our LLAM, localized thermal distribution dominates the deformation. To better understand this mechanism, a heat transfer analysis was performed to reveal the thermal distribution on both the surface and throughout a cross-section of the LLAM, shown in Fig. 4.2B. The surface thermal distribution (Fig. 4.2B, middle) was first compared to a thermal image taken with an infrared camera (model) (Fig. 4.2B middle).

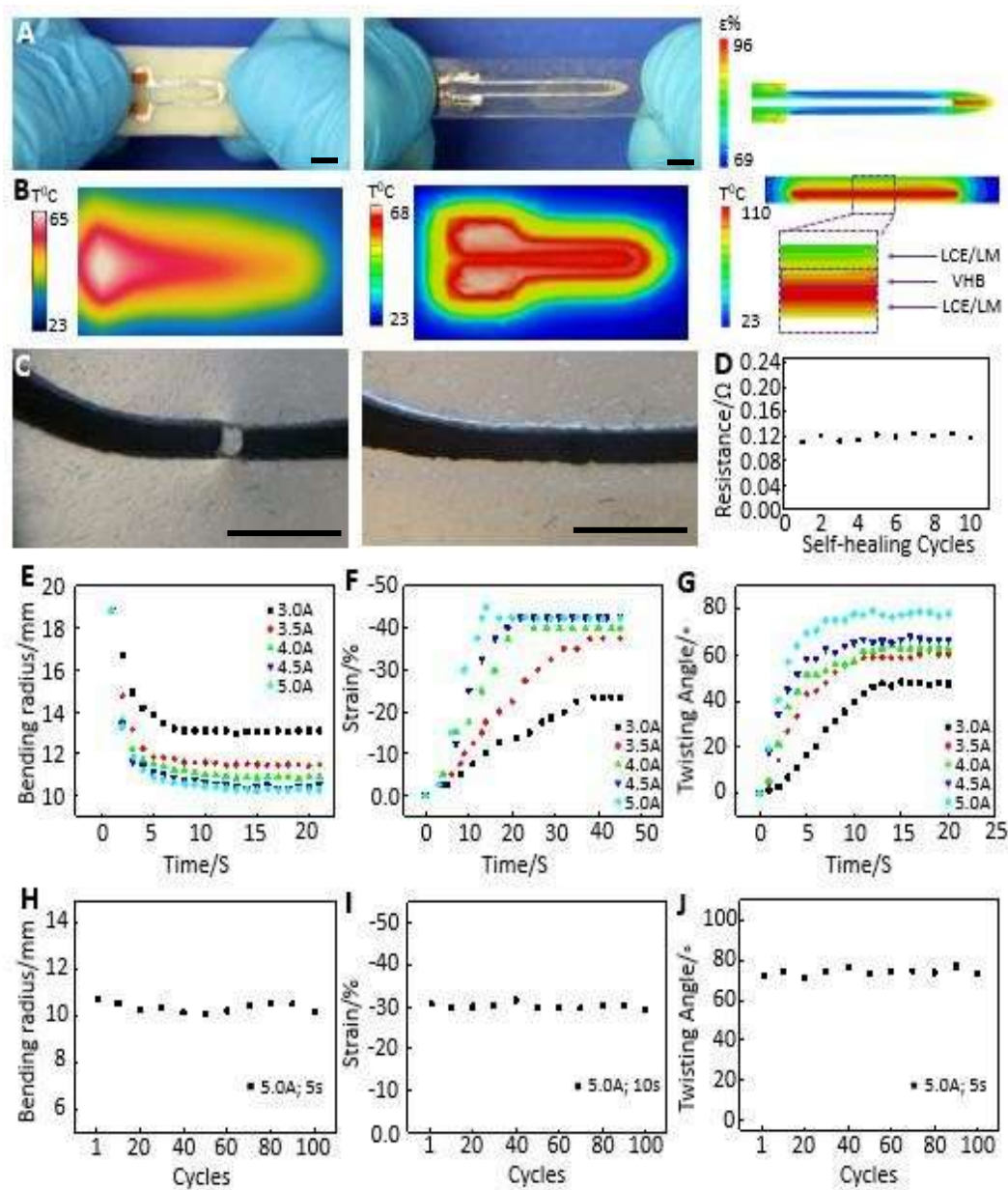


Figure 4.2. Characterization of the LLAM. (A) Experimental images and FEA results shows the LM deforms along with the LCE substrate during 2nd stage UV programming. The FEA results reveals Strain large than 69% and LM remains conductive. (B) Thermal images of the surface of LCE/LM actuator during full actuation mode and cross-section temperature distribution of the actuator. The thermal image and cross-section temperature distribution explained how temperature varies inside of the actuator, also explained why bending happen

when one side of the actuator was heated up. (C) self-healing of the LM channel encapsulated by LCE. After 10 times damage and self-heal, the conductivity of the LM heater doesn't show any increase. (E-G) Experimental test shows the performance of the LCE actuator during bending, shrinking and twisting, current of 3A, 3.5A, 4A, 4.5A and 5A were supplied for the actuation. (H-J) Cycle test of the LCE/LM actuator for 100 time, the performances remain almost the same.

We then investigated the thermal distribution of a cross-section, as in Fig. 4.2B, right. When one of the heaters was on, the temperature of the LCE layer beside this heater was much higher than on the other side: $>90^{\circ}\text{C}$, higher than transition temperature, versus $\sim 70^{\circ}\text{C}$, lower than transition temperature. To our knowledge, the LCE network deforms gradually with respect to temperature. Bending thus dominates due to the unsymmetrical actuation strains of the two LCE layers with different temperature gradients. When both heaters were on, the thermal distribution was symmetrical and more uniform along the cross-section, leading to linear actuation. Another advantage of introducing the LM heater into an LCE network is the self-healing property of the LM itself. In our work, the LM heater cross-section was designed with a small aspect ratio, thus damage almost never happened due to actuation. However, to investigate the self-healing of our LLAM, we first cooled the LLAM to a low temperature ($\sim 15^{\circ}\text{C}$, under which the LM heater shifted to a solid heater) and manually broke it, shown in Fig. 4.2C, left. By simply heating up the LLAM, the gallium heater was healed by slightly pressing the nearby area, shown in Fig. 4.2C, right.

The electrical conductivity of the Gallium heater during 10 cycles of breaking and re-healing is shown in Fig. 4.2D.

Since the LLAMs response to electric stimulation depends on time and current intensity, a detailed characterization of the bending, shrinking and twisting performance of the LLAM was carried out, as shown from Fig. 4.2E to Fig. 4.2J. Five different current values were applied and the actuation performances were recorded with respect to time. Figure 4.2E shows the radius change of the LLAM with respect to time and applied current. When a current was imposed on one of the LM heaters, the bending radius of the LLAM decreased with time and was relatively stable after about 5 seconds. In fact, higher current leads to a smaller stable bending radius and a faster actuation speed. Similar phenomena were observed for linear shrinking and twisting, as shown in Fig. 4.2F and Fig. 4.2G. It should be noted that the shrinking deformation took almost twice as long to reach a stable state as the other two forms, since the LLAM needs to be heated up more uniformly for linear actuation, as opposed to the other forms of actuation. We also investigated the performance of LLAM after many cycles. The cycle tests for bending, shrinking and twisting actuations were repeated at least 100 times each at a current of 5A, which offered the maximum actuation power. For bending and twisting cycle tests, currents were applied for 5 seconds. For the shrinking cycle test, the current was run for 10s, due to the effect's slower response. The cycle tests data are shown in Fig. 4.2G- Fig. 4.2I. After cycling through 100 times, the actuators show almost no change in performance.

Natural muscular tissues, especially for cephalopods, consist of active muscles and passive surrounding tissues and skins. The combination of such active/passive systems

paves the way for large actuation, complex texture transformations, and overall surface topology shifting. We integrated our active LLAM with passive soft materials such as PDMS (Polydimethylsiloxane) and Ecoflex (Ecoflex-00-30), and achieved the transformation of a 2D surface to a targeted, complex 3D shape. Considering that most biological deformation occurs as bending, we created an active/passive artificial tissue (APAT), as indicated in Fig. 4.3A. The APAT consists mainly of two parts: the LM heater micro channel, and the aligned LCE unit. We fabricated the LM heater channel with a similar method to that mentioned before but replaced the LCE with PDMS or Ecoflex. An LCE layer was prepared separately and aligned as a sheet beneath the LM heater channel (alignment direction shown in Fig. 4.3A). Patterns were then cut out of the LCE sheet using a mechanical cutter and the LCE layer was adhered to the LM channel on the VHB side directly. The adhesion between VHB and LCE layers proved to be very robust. Such a combination enables a soft, bio-mimicking actuator with both active ‘muscle’ and passive ‘tissue’.

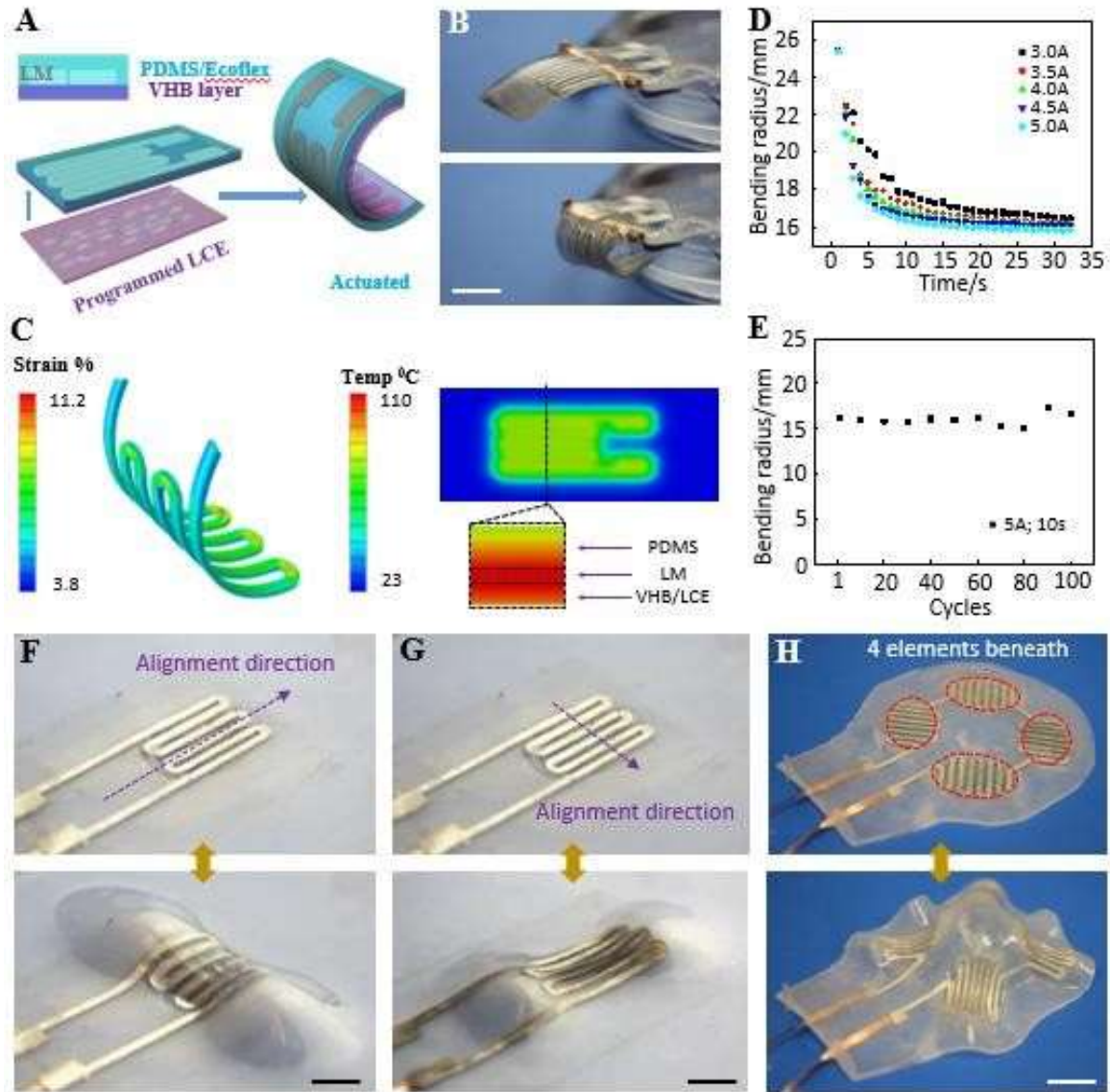


Figure 4.3. Design and characterization of the APAT. (A) concept of the APAT, LM was casted by passive materials like PDMS or Ecoflex, and a programmed piece of LCE layer was attached underneath. The LM heater can heat the LCE layer and the actuator bends. (B) Experimental image of the APAT. (C) FEA analysis of the strain and temperature distribution of the LM channel. (D,E) Characterizations of the APAT bending performance, and cycle testing of 100 times. (F-H) Designed pattern transformation of APAT, the alignment direction

offers different patterns and can function as single unit. While multiple units of LCE layers deforms a 2D plate piece into more complex 3D geometry. Scale bar is 5mm.

The deformation, in this case, is mainly bending, as shown in Fig. 4.3B. Upon heating, the aligned LCE layer shrinks while the passive layer remains almost unchanged, with the strain mismatch of the two layers leading to bending deformation, as indicated in Fig. 4.3B, bottom. Both mechanical and thermal analyses are demonstrated in Fig. 4.3C, with the mechanical analysis of LM fluidic channel deformation highlighting the advantage of adopting LM as heater material. Evidently, the maximum strain is about 10% (Fig. 4.3C left), which is higher than the yielding strain of most metals. Thermal analysis shows the thermal distribution of the cross-section of our APAT, shown in Fig. 4.3C, right. The temperature of the LCE layer, according to the simulation, is over 110°C, which is higher than the full actuation temperature of the LCE network. The bending performance of our APAT was characterized as shown in Fig. 4.3D. Five current values (3A, 3.5A, 4A, 4.5A, and 5A) are supplied, lasting for 30s, and the final bending radius of each case was recorded. Experimental data indicates that the bending radius increases with time and becomes stable after about 10s, with higher current values leading to smaller stable bending radii and quicker actuation. To investigate the robustness of our APAT, tests of 100 cycles were performed. A current of 5A applied for 10 seconds was applied to the LM heater and the bending radius at 10 seconds was recorded, as shown in Fig. 4.3E. Cycle test data reveals that the APAT shows almost no obvious performance change.

To further demonstrate the combined actuation of active and passive soft materials, a programmed LCE layer with an ellipse shape was attached under a much larger sheet of

Ecoflex with an embedded LM heater. The LM heater patterns covered the LCE layer from beneath and a current of 5A was applied to trigger deformation. Localized bulging formed due to the LCE layer shrinking, deforming the passive surrounding materials, as shown in Fig. 4.3F and Fig. 4.3G. Particularly, we aligned the ellipse LCE layer as indicated by the purple dashed lines in Fig. 4.3F and red dashed lines in Fig. 4.3G. More complex deformations can be realized with more independent elements. Here, four LCE elements were attached under the Ecoflex layer, each with a custom-designed LM heater on top. A current of 5A was applied to all the heaters, stimulating all four LCE elements at the same time. The overall actuation of the LCE elements thus deformed the flat 2D surface into a complex 3D configuration, as shown in Fig. 4.3H. The pictures also indicate an advantage of LM heaters, especially in this case, as the LM heaters are not only robust, but they do not confine the actuation.

In nature, mollusks tout the most potential for deformation. A leech can elongate its body to more than 5 times its original length, a snail can retract into a tiny shell with limited space, and an octopus can blend into its surroundings almost perfectly. Those creatures achieve complex shape change due to muscular hydrostat, which requires incompressible muscle actuation. Inspired by nature, a camouflaging soft robot was developed using the APAT approach. Figure. 4.4 demonstrating three different kinds of camouflage systems. Figure. 4.4A shows the deformation of a flat surface into a star like structure when electricity is connected to the LM heaters. The shape can be held for as long as the current is supplied. Assorted sizes of origami stars (made by hand) were placed around the APAT to compare the shape. The star camouflage was realized by attaching four LCE elements beneath an Ecoflex sphere sheet. LM heaters were fabricated in certain

areas where the LCE elements were attached. The stimulation and dissimulation of the LCE elements led to the reversible shape transformation from a 2D circular surface into a 3D star shape. Pink pigment was painted on both the APAT circle sheet and origami stars. Fig. 4.4B shows an APAT stripe camouflaged into a cluster of water plant leaves. The APAT stripe was painted with a ThermoChromic Temperature Activated Pigment, which is blue at room temperature and shifts to green at temperatures higher than 30°C (Fig. 4.4B). Higher temperature further triggered the transformation of the APAT from a flat stripe into a shape similar to that of the surrounding water plant leaves, shown in Fig. 4.4B bottom.



Figure 4.4. Demonstration of camouflage. (A) Experimental images showing a flat piece of APAT deformed into sea star shape, when a voltage of 5A was applied on the LM heaters. (B) Experimental image showing a flat APAT stripe that can deformed into water plant shape and change its surface color as well. The shape change is due to the actuation of

APAT while the color change is due to the ThermoChromic pigment mixed inside of the polymer network, which changed its color at temperature higher than 30 degree Celsius.

(C) A soft robot than can move forward into a Fungi group and deforms its back layer skin into a similar shape. The soft walker was also made of APAT, which bended during heating and flat when voltage cut down. Uni-fiction feet was embedded beneath to enable moving forward. Scale bar is 25mm

Next, a soft robot with camouflageable (camo) skin is demonstrated in Fig. 4.4C: I, II and III. The camo soft robot was composed of two parts: a soft walker on the bottom and a camo skin on top. The walker was fabricated into a rectangular APAT stripe with three fishing hooks beneath to function as uni-frictional feet with the capability move forward with simple bending and recovery. The camo skin consisting of three LCE elements was bonded to the soft walker using a drop of liquid Ecoflex that was subsequently cured. As demonstrated in Fig. 4.4C I and II, the soft robot traveled from an empty area into a group of real fungi. The skin, painted with a black pigment, was triggered to display the camo effect, simultaneously deforming the robot into the shape of its surroundings. The position of the fungus group in Fig. 4.4C III was arranged for the best camo effect.

The soft walker, at the same time, can be self-sensible, since LM can be used to fabricate very sensitive strain sensor. A self-sensible soft walker that sense its own deformation during work has been carried out with APAT. Figure 4.5A indicates the design and principle of such self-sensible soft walker. Two LM structures were fabricated on both

sides of the PDMS encapsulation layers. A programed LCE layer was attached to one side working as actuator. When actuating, the soft walker bended, leading to an increase of strain of the LM sensor on the other side, the deformation further led to the increase of resistance which was recorded by a data collector (National instrumental NI USB-9162). Thus, the deformation of the soft walker can be mapped to the resistance change of the LM sensor, as indicated in Fig. 4.5B. The height of the bending walk and the resistance change of the sensor are recorded with respect to time. Thus we obtained a relationship of the deformation with the resistance change, shown in Fig. 4.5C. Noted here that the resistance change could also from the heating effect from the LM heater on the other side. To further investigate this problem, a comparison experiment was carried out, in which the soft walker was fixed at two ends and was applied the same actuation current. The resistance change of the LM sensor was recorded, but almost no obvious resistance change was observed for the comparison experiment, thus, exclude the influence of heat. Further, thermal analysis (transient heat transfer analysis) of the temperature change of the LM sensor was also carried out. At time of 1s, 2s, 3s, 4s and 5s, the temperature of the LM sensor shows no obvious change, this is due to the low thermal conductivity of the PDMS layer and its comparatively large thickness (2mm).

The soft walker can sense its amplitude of moving as indicated in Fig.4.5D. A current of 3.5A was applied to the LM heater for ~4 seconds and cut off, the walk accomplished a cycle of motion and got one step forward, repeating such process ended up in moving from right to left, shown in Fig. 4.5D, upper. The corresponding resistance change of the walker during moving was recorded as well in Fig. 4.5E, upper. Similar processes but with a longer

heating time were used to let the walker have a larger moving amplitude, and the resistance change was also recorded, shown in Fig. 4.5D, middle and Fig. 4.5E, middle. Further, the soft walker was allowed to move at different amplitude and pass through a narrow space, shown in Fig. 4.5D, bottom, with a corresponding resistance change recorded. The experiments indicates that the APAT system can function well as both actuators and sensors.

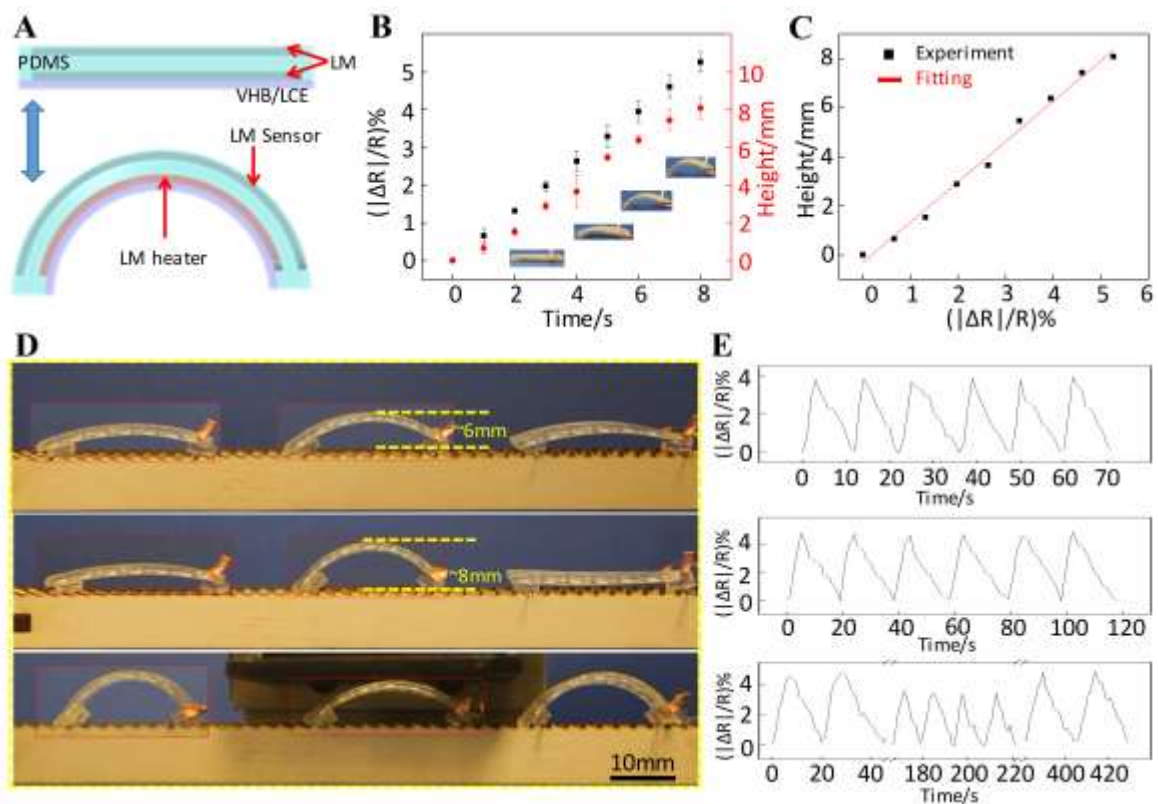


Figure 4.5. Self-sensing of LM/LCE based soft walker. (A) Concept shows how LCE soft walker sense its own move. A LM heater was embedded close to the LCE layer for actuation purpose, and a LM sensor was fabricated into the top layer that senses strain during deformation. (B) Relationship of LM sensor resistance change and the soft walker bending arch (height) with time after electrical current was applied to the LM heater. (C) Relationship

of the arch height with the LM sensor resistance change. (D) Experimental images showing the soft walker: moving forward with different amplitude (6mm high and 8mm high); squeeze into narrow space. The surface is made into uni-frictional for better controlling of each step of moving. (E) The soft walker can sense its own moving corresponding to three different case: moving with low amplitude; moving with high amplitude; squeezing into narrow space and move out.

4.3 Materials and methods for artificial skin

Material preparation. The LCE was prepared using a two-stage thiol-acrylate Michael addition-photopolymerization (TAMAP) reaction. 4-bis-[4-(3-acryloyloxypropypropyloxy) benzyloxy]-2-methylbenzene (RM257), pentaerythritol tetrakis(3-mercaptopropionate) (PETMP), 2,2-(ethylenedioxy) diethanethiol (EDDET), (2-hydroxyethoxy)-2-methylpropiophenone (HHMP) and dipropylamine (DPA) were used as received from Sigma Aldrich, except for RM257, which was from Wilshire Technologies. 4g of RM257, 0.217g of PETMP, 0.9157g of EDDET and 0.0257g of HHMP were dissolved into 1.6g of toluene solution. 0.568g of DPA (diluted with toluene at a ratio of 1:50) was then added into the solution for the first stage polymerization and cured at 80°C for 12h. The cured polymer was then stretched and exposed to UV light for at least 15mins (Omincure 2000) to trigger the second stage of polymerization.

FEA analysis to predict patterns. Finite element methods was adopted here for predicting the pattern formation of APAT. The LCE was molded with C3D8 element and used a user-defined-material (UMAT), in which, pre-stretch was introduced. However, thermal

expansion of the LCE was ignored due to its much less intense compared to linear actuation.

The detailed shape transformation was shown in Fig. 4.6

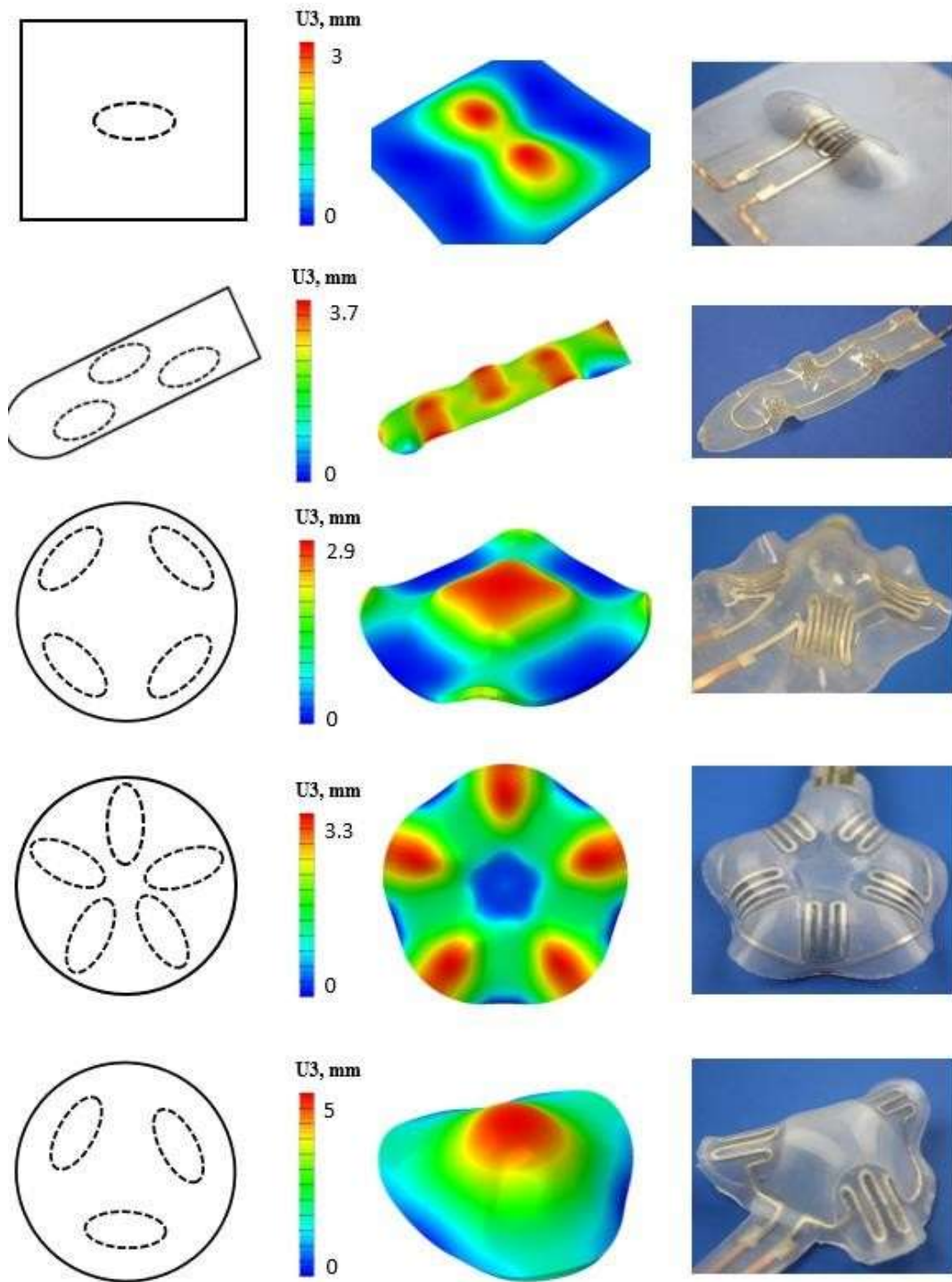


Figure 4.6. Finite element analysis for predicting such transformations

Fabricating LM patterns. The LM patterns were fabricated using a simple stencil method. Card stock paper (thickness, 350 um) was purchased from Amazon and cut into the designed pattern with a laser cutter. The paper mask was then placed on top of a VHB layer (3M VHB). LM was then cast on top of the mask, with the sticky surface of the VHB holding the LM pattern very well. After patterning, the paper mask was removed, leaving the LM pattern on top of the VHB layer. Copper wires were connected to the LM pattern as electrical connections, and experiments reveal that simple contact between the LM and copper guarantees robust electrical connectivity.

Embedding LM into LCE, PDMS or Ecoflex. To embed LM into other materials, the LM patterns were fabricated using the aforementioned method. The LCE solution remained in liquid state for around 15 mins after adding diluted DPA. The solution is cast on top of the LM patterns and placed in a vacuum chamber for 1 minute at 508 mmHg in order to remove any air bubbles caused by mixing. Everything was then sandwiched between two glass slices and cured at 80°C for 12h. When programming, LCE/LM system is heated above 30°C, then stretched and exposed to UV light with the LCE side on top. For PDMS and Ecoflex, the LM pattern was simply cast, degassed, and cured in the same way. Programmed LCE layers were then attached to the other side of the VHB. Due to the sticky nature of VHB, the adhesion between the VHB and LCE proved to be very reliable.

Fabricating camouflageable soft robot. The camo soft robot consists of two parts: the soft walker and the camo skin. Both parts were fabricated with the same system of passive/active component combination. To enable the walker to move forward, fishing hooks were partly embedded into the two ends of the walker, all pointed backwards. A current was applied to

the heater in the walker to trigger bending and then cut off to recover, the repetition of which enables the walker to move forward. The camo skin was fabricated with an Ecoflex sheet and three LCE elements and adhered to the top of the walker with liquid Ecoflex.

Testing bending, shrinking and twisting. To test the actuation performance of the devices, five current values were supplied, ranging from 3.5A to 5A. The actuation effects were recorded by video and the bending radius, strain, and twisting angle were analyzed directly from the video cut. For the cycle test, a current of 5A was applied to the bending and twisting case of LLAM for 5 seconds, and a current of 5A and was applied to linear shrinking of LLAM and bending of APAT for 10 seconds.

In this work, LM and LCE were combined to create a novel, completely soft actuation system. LCE offers advantages over all kinds of soft actuators and requires only heat stimulation. By introducing the LM heater, much more robust actuation can be achieved. The LCE heater, at the same time, is self-healable. A clever heating element pattern design helps to avoid the collapse of the LM fluidic channel. Inspired by natural muscle and tissue, active and passive soft materials were then joined to achieve complex deformation and camouflage abilities. In current research, the patterning of LM is limited to stenciling methods. Thus, to realize a small aspect ratio in the LM fluidic channel, the LM heater was made thick and bulky. In the future, other methods can be introduced to pattern much smaller scale LM heaters, which could further enhance the robustness and lower the current input for tomorrow's soft robots.

Chapter 5

Fabrication and characterization of highly deformable artificial muscle based on liquid crystal elastomer

5.1 Artificial muscles for robotics and healthcare

Robotics have huge potentials for daily care, medical aid, and other aspects of human life, as the technologies of materials, algorithms, control and machine learning are developing rapidly. To better serve people's life, robotics and other medical devices should be conformal to human bodies and perform as good as those conventional ones without loss of performance [110]–[116]. Soft materials and corresponding technologies are attracting more and more attention due to their adjustable properties, i.e., mechanical stiffness, electrical conductivity, thermal conductivity, and bio-compatibility, and therefore, they provide promising future for soft, compliant and high-performance robots, medical devices, and health care devices beyond the current rigid, cold, and bulky formats[116], [117].

Researches have made impressive progresses on various aspects of more human-like robots and human-friendly devices, including artificial skins[80], [118], [119], neural systems[120], and implantable devices[121]. However, another critical part of soft systems, i.e. the actuation mechanism or artificial muscles, is still far from ideal. There are several

candidates for artificial muscles, including dielectric elastomers[25], [122], ionic polymer metal composites[123], and liquid crystal elastomers (LCEs)[124], [125]. Among these candidates, LCEs possess characteristics most suitable for natural muscle-like actuators, including reversible and repeatable deformation, large elastic deformation range, low actuation voltage, remote control, and superior form factor[125]. LCEs are polymer networks in which liquid crystal monomers are aligned in certain programmed directions, i.e., the monodomain. When heated up, the liquid crystals lost their uniformity and forms multi-domains, i.e., the isotropic state, resulting in a macro-scale deformation[126]. When cooled down, the liquid crystals recover their alignment in the programmed directions, leading to macroscopic recovery of deformation. Such shape change can be as large as 400% [28]. Popular methods for heating up the LCEs include heating on a hot plate, light, and embedded heaters. For practical applications, energy delivery using embedded heaters is perhaps the most effective, efficient, and controllable[31]. However, conventional heaters are rigid and brittle, and cannot comply with the deformability of LCEs.

Here, we present a material system based on liquid metal (LM) as heater material and LCE as soft actuator, and demonstrate a fast, low cost and efficient fabrication method to pattern the heater in LCEs for artificial muscles. The LM heater is embedded inside LCE and is capable of undergoing large deformation together with the LCE, without any mechanical failures, interfacial delamination, or fatigue. In this study, we carried out fabrication, characterization, and analysis of the novel artificial muscles based on LCEs and LM.

5.2 Fabrication and characterization of LCE based artificial muscle

The LCE used in this study is based on a two-stage Thiol-Michael addition polymerization formula[127]. Three commercially available monomers are chosen as the base materials: 4-bis-[4-(3-acryloyloxypropypropyloxy) benzoyloxy]-2-methylbenzene (RM257), pentaerythritol tetrakis(3-mercaptopropionate) (PETMP) and 2,2-(ethylenedioxy) diethanethiol (EDDET). RM257 is the mesogen monomer which acts as the liquid crystal in the polymer matrix. PETMP is used as the crosslinker, and EDDET is a linear extender to adjust the stiffness of the polymer network. In this formula, 15 mol% excess of RM257 is adopted which is further crosslinked in the second stage. Dipropylamine (DPA) is the catalyst for the Thiol-Acrylate reaction in the first stage, while (2-hydroxyethoxy)-2-methylpropiophenone (HHMP) is used as the catalyst for the second stage polymerization under UV light exposure(365nm). This formula of LCE has a transition temperature around 100 °C. The LM is a combination of gallium and indium, with a weight ratio of 75% and 25% respectively. These two metals are mixed together at a temperature of 150 °C using a mechanical stirring machine for 30 mins. The LM alloy transitions into liquid state at temperatures higher than 15 °C.

A screen printing method was developed for the fabrication of the artificial muscle. Figure 1A illustrates the schematic design of the artificial muscle, which consists of a very thin VHB layer (25um) at the bottom, LM heater (200um) enclosed in the middle, and a LCE

layer (1000um) at the top. The fabrication process is schematically shown in Fig. 5.1B. The LM is first patterned with a mask on the VHB layer, with line width of 500 μm . The strong adhesion of VHB tape conquers the LM surface tension and holds the LM pattern without merging into spheres. Then the mask is removed, and liquid LCE prepolymer is cast on top of the LM side of the VHB layer. After being placed on a hotplate with 80 $^{\circ}\text{C}$ for 12 hours, the artificial muscle is stretched with 100% program strain (Fig. 5.1C) and exposed under UV light (365nm) for 15 mins for the second stage polymerization.

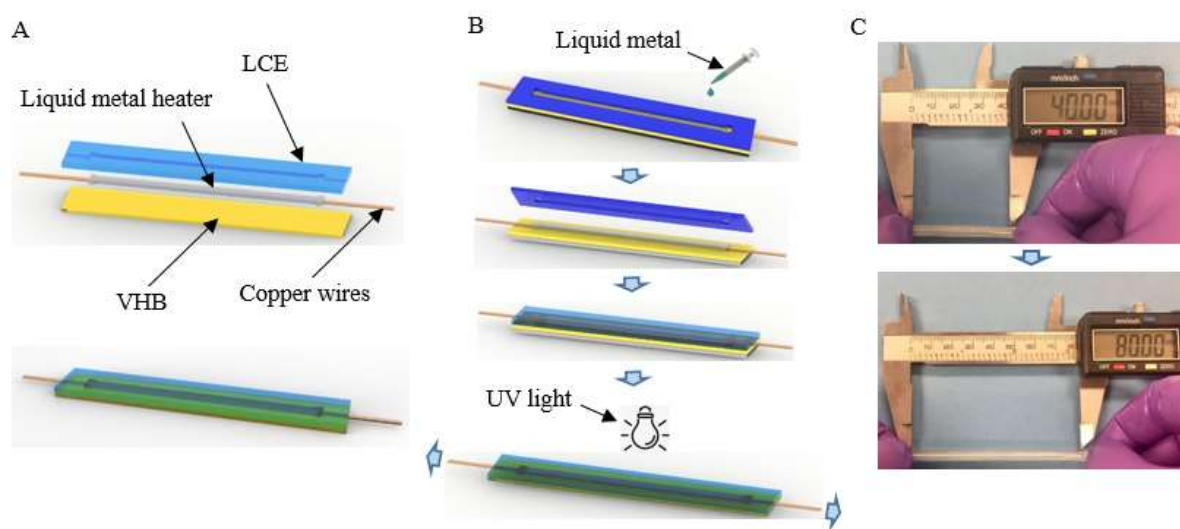


Figure 5.1. *The design and fabrication process of the LCE/LM artificial muscle. (A) The schematic design of the artificial muscle. (B) Fabrication process of the artificial muscle by using screening printing method. (C) Optical images of the LCE/LM artificial muscle at the*

original (upper, un-stretched), and the programmed state with 100% program strain (bottom, stretched).

Systematic characterization of the actuation behavior and performance are carried out. **Figure 5.2A** shows the setup for the contraction testing of the artificial muscle, which is fixed to a clamp at one end while the other end remains free. A small paper clip is attached to the free end to keep the sample straight before actuation. The paper clip has a weight of 1g, which is negligible compared with the lift force of the artificial muscle (~ 2 N, see below). An electric current is supplied to the LM heater to heat up the LCE. To investigate the temperature increase, an infrared camera is used for recording the surface temperature of the LCE during heating and cooling. Five different electric current values are used and the steady states of the deformed artificial muscle are recorded and exhibited in **Fig. 5.2B**. The first image shows the artificial muscle when it's not heated. The second to the sixth images demonstrate the steady states of the artificial muscle after it's heated with 1.5 A, 2.0 A, 2.5 A, 3.0 A, and 3.5 A electric current. The results show an increase of surface temperature and contractive strain corresponding to the increasing electric current.

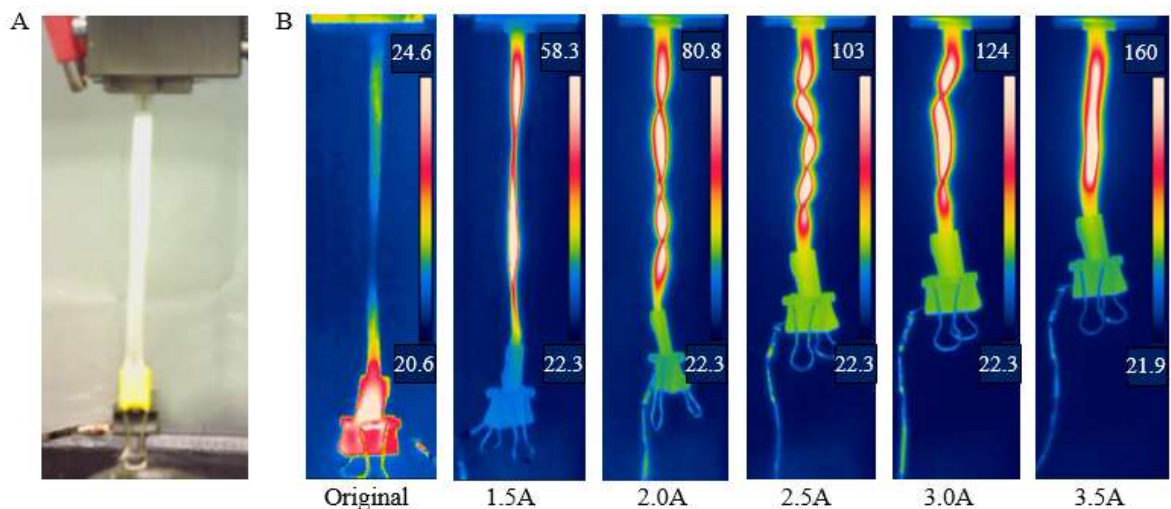


Figure 5.2. *Contraction test of the artificial muscle. (A) Experimental setup for the contraction test: one end of the artificial muscle is fixed while the other end keep free. A paper clip (~3g, much smaller than the actuation force) is attached to keep the sample straight. (B) Deformation and temperature distribution of the steady-state artificial muscle heated with different electric current.*

The dependence of the temperature increase and contraction strain in the artificial muscle on the heating electric current and size of the muscle fiber is investigated, and the results are presented in Fig. 3, as both the heating power and the size of the muscle fiber affect the heat transfer and temperature increase in the LCE. Here, three different widths of muscle fibers are fabricated and characterized: 3.1 mm, 4.51 mm, and 5.56 mm. Five different electric current values are supplied, and the temperature increases and the contraction strains at the steady states are presented. Figures 5.3A and 5.3B demonstrate the surface temperature and contraction strains of the artificial muscle of width 3.1 mm at the steady states versus the electric current. As the electric current increases from 1.5 A to 3.5 A, the surface temperature increases from 58.4⁰C to 160⁰C, while the contraction strain increases from 12.5% to 44.7%.

The results for the artificial muscle of width 4.51 mm and 5.56 mm are presented in Figs. 5.3C to 5.3F. The results show that the temperature and contraction strain decreases with increasing muscle width for the same electric current. For example, at 3.5 A electric current, the surface temperature decreases from 160⁰C to 115⁰C and 100⁰C, and the contraction strain decreases from 44.7% to 38.8% and 33.3%, when the muscle width increases from 3.1 mm to 4.51 mm and 5.56 mm.

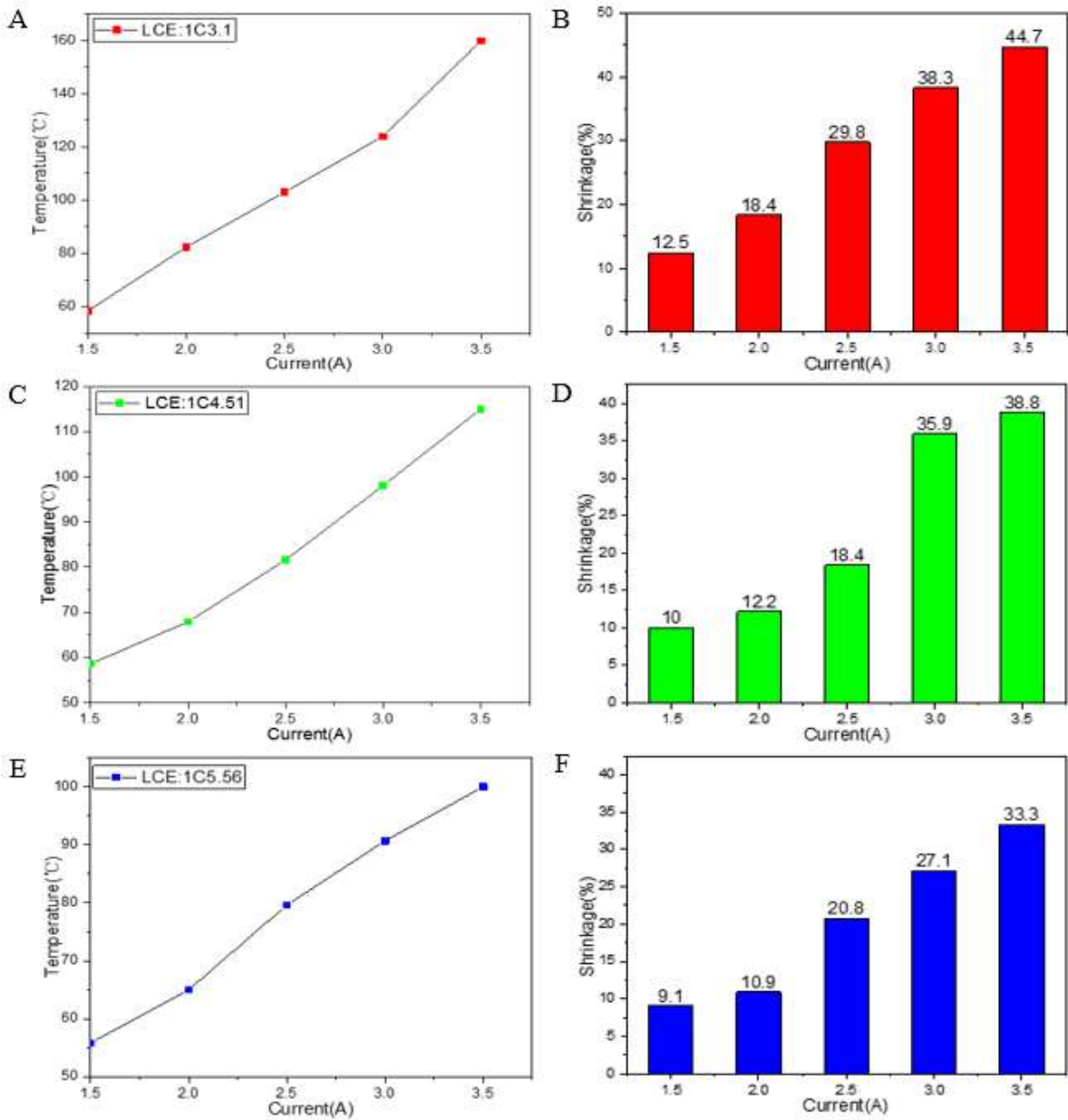


Figure 5.3. *Temperature and contraction characterization of the artificial muscle. The dependence of the steady-state surface temperature (A) and contraction strain (B) of the artificial muscle on electric current for LCE width 3.1 mm. The dependence of the steady-state surface temperature (C) and contraction strain (D) of the artificial muscle on electric current for LCE width 4.51 mm. The dependence of the steady-state surface temperature (E) and contraction strain (F) of the artificial muscle on electric current for LCE width 5.56 mm.*

Another important property of the artificial muscle is the force output during actuation. **Figure 5.4** demonstrates the experimental setup for measuring the pulling force of the artificial muscle. The artificial muscle is fixed at both ends in an Instron 5965 Material Testing System. The pulling force is recorded with respect to time when electric current is supplied to the LM to heat up the LCE. The surface temperature of the artificial muscle is monitored by an infrared camera. As shown in **Figs. 5.4B.** and **5.4C** are the temperature distribution in the artificial muscle when not heated and when an electric current of **2.5 A** is supplied to the LM. The surface temperature of the artificial muscle increases from $22\text{ }^{\circ}\text{C}$ to $75\text{ }^{\circ}\text{C}$.

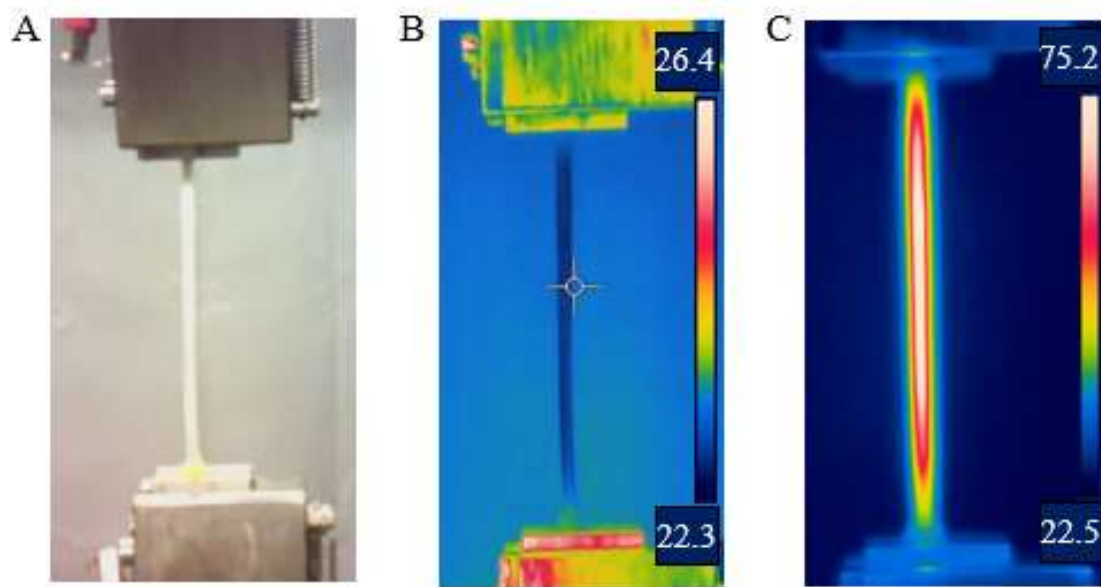


Figure 5.4. Pulling force test of the artificial muscle. (A) Experimental setup for the pulling force test: two ends are fixed in an 5965 Material Testing System, and the force is recorded with respect to time. Surface temperature measurement from an infrared camera at the beginning of the test (B) and during steady state (C) with electric current 2.5 A and sample with 5.56 mm.

The surface temperature and nominal pulling stress versus time for three different muscle fiber width 3.1 mm, 4.51 mm, and 5.56 mm are presented in Fig. 5.5. Five different electric current values ranging from 1.5 A to 3.5 A are supplied to the LM to generate heating. The results clearly show that for the same artificial muscle, higher electric current leads to faster temperature increase, and higher surface temperature and higher pulling stress at the steady state. However, for the same electric current, the surface temperature and nominal pulling stress at the steady state don't show strong dependence on the size of the artificial muscle, but the muscle fiber with larger cross sectional area can certainly generate larger pulling force.

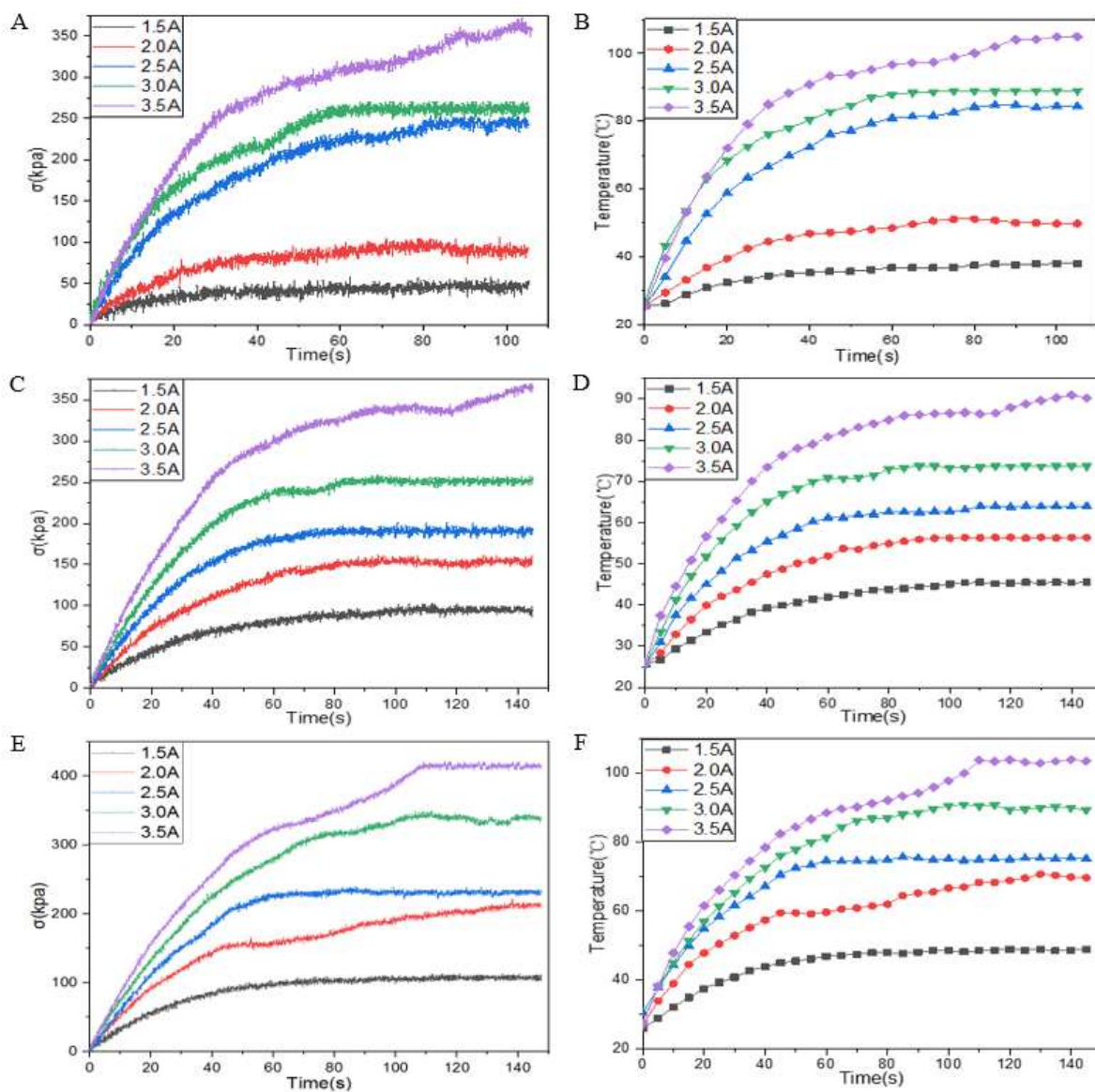


Figure 5.5. Pulling force characterization of the artificial muscle. The surface temperature (A) and nominal pulling stress (B) of the artificial muscle versus time with different electric current for LCE width 3.1 mm. The surface temperature (C) and nominal pulling stress (D) of the artificial muscle versus time with different electric current for LCE width 4.51 mm. The surface temperature (E) and nominal pulling stress (F) of the artificial muscle versus time with different electric current for LCE width 5.56 mm.

5.3 Conclusion:

In this work, the fabrication method for realizing a novel type of artificial muscle based on LCE and LM is developed and the actuating properties are investigated. Because of the liquid-like property, the LM heater fully embedded in the artificial muscle can undergo very large deformation without introducing any damage. To study the actuating characteristics, the dependence of surface temperature, contraction strain and nominal pulling stress of the artificial muscle on the electric current, heating time, and size of muscle fiber is studied. The results could provide important guide for designing artificial muscles or other applications that utilize actuation mechanism of LCEs.

Chapter 6

A vivo-mimetic prosthetic hand with a tendon-pulley design

6.1 Current researches about Prosthetic hand

Prosthetic hands, as one of the most important parts serving disabled person, have been devoted into huge effort in the last few decades. However, most of the econometrical prosthetic hands are still lack of durability, high performance, lightweight, Bionic-look, and affordability[128]–[131]. Various designs have been adopted such as Vincent hand[132], ILimb[133], Bebionic hand[134], and Michelange hand[135]. All those commercial prosthetic hand are based on a mechanical design that has stiff joints and low degrees of freedom, since all the power sources are from DC motors. This in turn leads to the bulky, heavy, complex and expensive products in the market nowadays. To overcome this, new mechanisms for auctions has been introduced, instead of using DC motor and mechanical gear systems, a tendon driven design have been introduced and was able to mimic the natural movements of human hands[136], [137]. However, such design still depended on DC motor as the power and required more space for the interconnectors between artificial tendon and the motor.

The key solution to such problems lie in the power source for actuation, while smart materials are fast developing for recent decades. Integrating smart materials into such systems

is thus promising. In other prosthetic parts, for example, a prosthetic arm equipped with a thermal pneumatic artificial muscle was successfully achieved[138], [139]. Other pneumatic powered health care and aid devices have been developed as well[140]. Apart from these, Shape memory alloys are also good candidates and are easy fabricated[141], [142]. More recently, Dielectric elastomers are also included in such systems and get a good performance [143], [144]. Among all those smart actuators, Liquid crystal elastomers (LCEs) attracted people's attention due to their actuating the most similar to natural muscles. Design and incorporate such materials into the prosthetic hand could potentially enable the artificial part function just like the real one.

In this work, a novel prosthetic hand combining the most up-to-date technology of Liquid Crystal Elastomer has been demonstrated[127]. Previous actuation methods for LCEs are subjected to the heating method, while directly embedding a heater seems to solve this problem[31]. However, those embedded heaters are either too rigid or too brittle. Here, we combined LCE actuators with Liquid metal heaters in a way that both large actuation strain and robustness can be achieved. Firstly systematic fabrication and characterization methods were explained, and then a tendon-pulley finger structure was adopted for integrating the LCE muscle into the prosthetic hand. Demonstrations of gestures and grabbing objects were shown at the end.

6.2 Fabrication and characterization of the prosthetic hand

The prosthetic hand in this work, other than conventional motor-joint ones, is based on a bio-inspired design shown in Fig.6.1A. The actuation materials are the tendons that are fixed onto the prosthetic hand, as indicated in Fig.6.1A left. For each finger, there is a strip of “tendon” that is consist of LCE and LM heater, sounded which three “pulleys” are responsible of holding the “tendon” close to the finger. Meanwhile, all parts including the prosthetic finger joints are treated with lubricant oil, and the “tendons” are free to move within the “pulleys”, mimicking natural human fingers. The pulleys in this work, to simplify the design, are made of rigid silicone tapes[145]. During actuation, they will prevent the LCE tendon from rupturing off the finger.

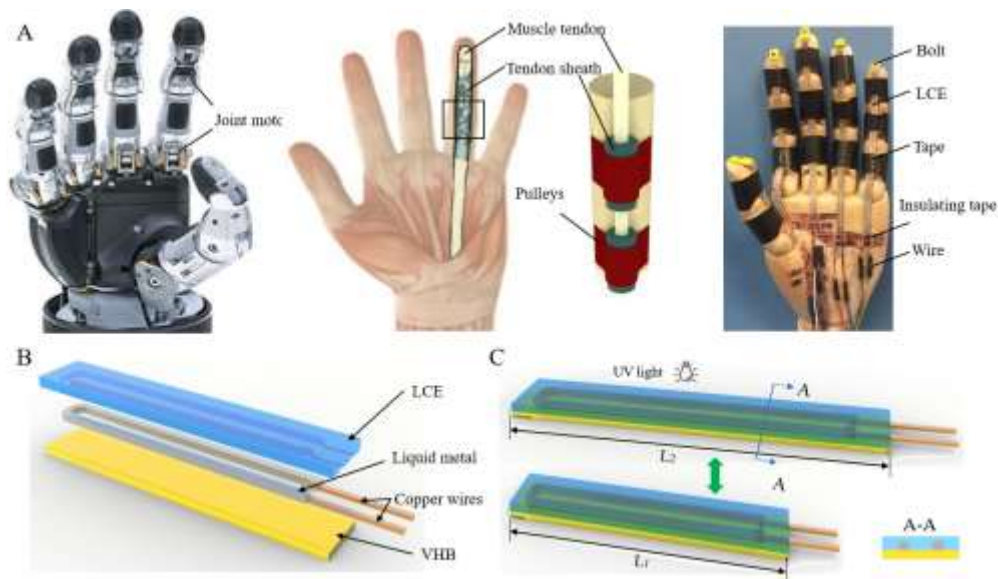


Fig. 6.1 Design, fabrication, and the structure of LCE. (A) Robot hand by joint motor. (B) The tissue structure of real fingers. (C) The structure of robot hand based on LCE drive. (D) The structure of robot hand based on LCE drive.

The structure of LCE. (E) The working principle of LCE. (F) The structure of LCE from another perspective.

The LCE “tendons” are based on a novel artificial muscle from our previous work []. The LM heaters are embedded into the LCE strip, as indicated in Fig.6.1B. The LM heater was patterned on top of sticky VHB layer utilizing a screen printing method, while two copper wires, which are used as external interconnectors, were connected at the end of the LM heater, the simple contact between the LM and the copper provided robust and good electric conductivity. Further, Liquid LCE (before Curing) was casted on top of the VHB bonding layer and LM heater pattern and was allowed to cure at 80 °C for 12h. The sandwiched structure was then pre-stretched from original length L_1 to a programmed length L_2 , indicated in Fig.6.1 C. UV light was used here for fixing the programmed state. Upon heating, in our case a current was applied through the copper wires, the LCE/LM actuators shrunk into the original length L_1 , while returned to L_2 when it was cooled down. Noted here that the thickness of the VHB layer in the current design is only about 25um which is way thinner than the total thickness of the LCE (thickness:1mm) and LM layer (thickness:0.6mm). Thus its mechanical effect to the actuation can be ignored.

To characterize the LCE/LM actuator, the sample was fixed at an Instron mechanical testing machine, and a thermal camera was placed nearby to recording the temperature change as well as the actuation strain. A current generator was used for supplying constant and stable electric current through the LM heater, the joule heating eventually led to the phase transformation of the LCE, and deformation happened. In the first case, the LCE is fixed on the clamp with only one end, while keep the other end free standing, indicated in Fig.6.2A.

When current passed through the LM heater, the LCE shrunk freely from the programmed length L_1 to the original length L_2 , shown in Fig. 6.2A right. The thermal camera recorded both the actuation strain and temperature distribution on the surface of the LCE/LM actuator. Further, image analysis revealed the relationship between the Strain and the current values. In the experiments, three current values are supplied: 1.5A, 2A, and 2.5A respectively, and three times of test were carried out for each current value, as indicated in Fig.6.2B, the Shrinking Strain increases with an increase of current, due to an more overall higher temperature of the LCE network, which results in higher actuation strain.

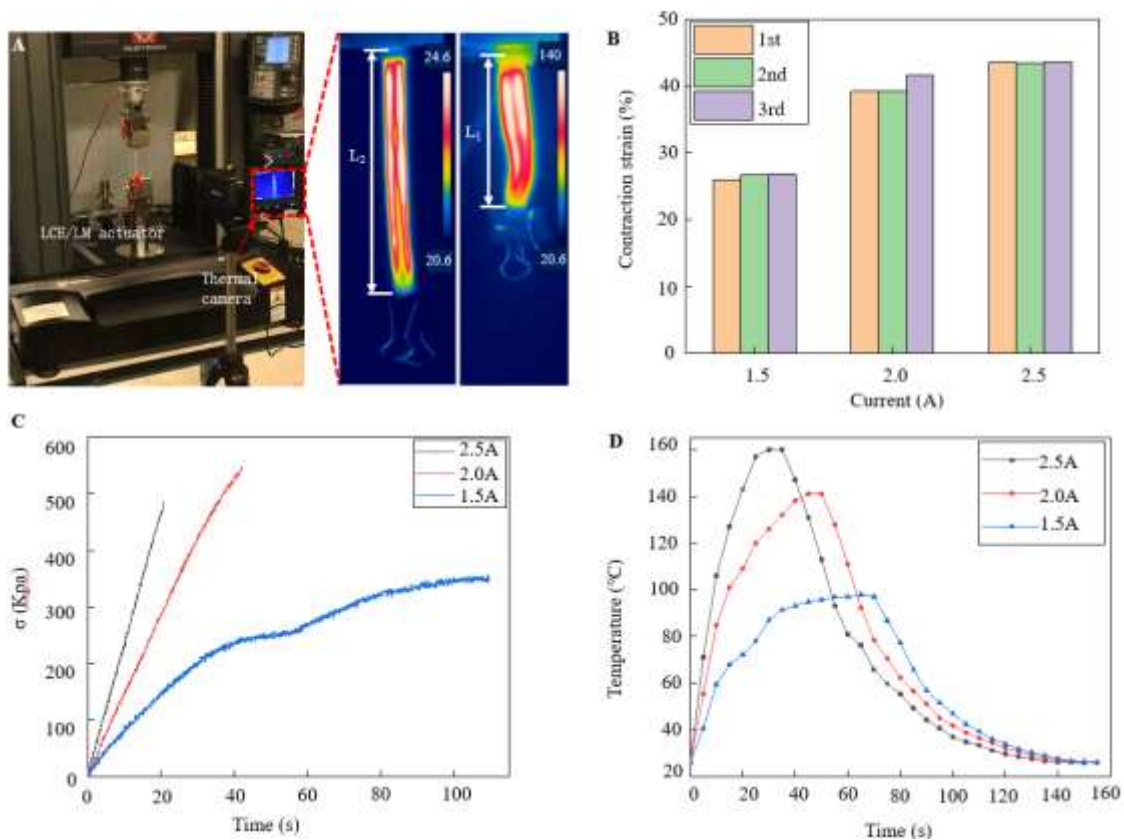


Fig. 6.2 The performance of LCE. (A) Experimental set up for measuring the Strain output of LCE muscle/tendon, a thermal camera was used to detect both the strain and temperature

(right). (B) Strain of LCE muscle at different current values, 3 samples are used here (C) Maximum Stress output of LCE under different currents. (D) Temperature change with respect to time under different current.

A second characterization was carried out in case of two fixed end on the mechanical testing machine, and the load was detected by the force sensor in the machine with respect to time. Figure 6.2C shows the stress response of the LCE actuator after a constant 2A current is applied, the results shows linear increase before 20s, while it tend to reach a peak value at 50s. Thus we notice that the maximum response time of the actuator and further cut the current at time of 50s, both temperature and stress started to decrease at the same time. The total cooling time in this case was found out to be about 110s, three times of testing was carried out as well, and the data of each test were close to each other, as indicated in Fig.6.2D.

One of the basic functions of a prosthetic hand is to make different gestures, which requires independent controlling of each finger. Here we embedded the LCE tendon into each finger, which was confined with three “pulleys” that we mentioned earlier, shown in Fig.6.3. To simply, rubber bands were used as “extensor tendons” for the recovery of the fingers to their original shape, see Fig.6.3A right. Then current was applied to all five tendons to make a “fist” gesture (Fig.6.3A). Moreover, other gestures can be easily realized by independently controlling the fingers, for example, a “thumb up” gesture can be made by actuating all the rest of the four fingers (Fig. 6.3B), and more examples are shown from Fig.6.3C to Fig.6.3F.

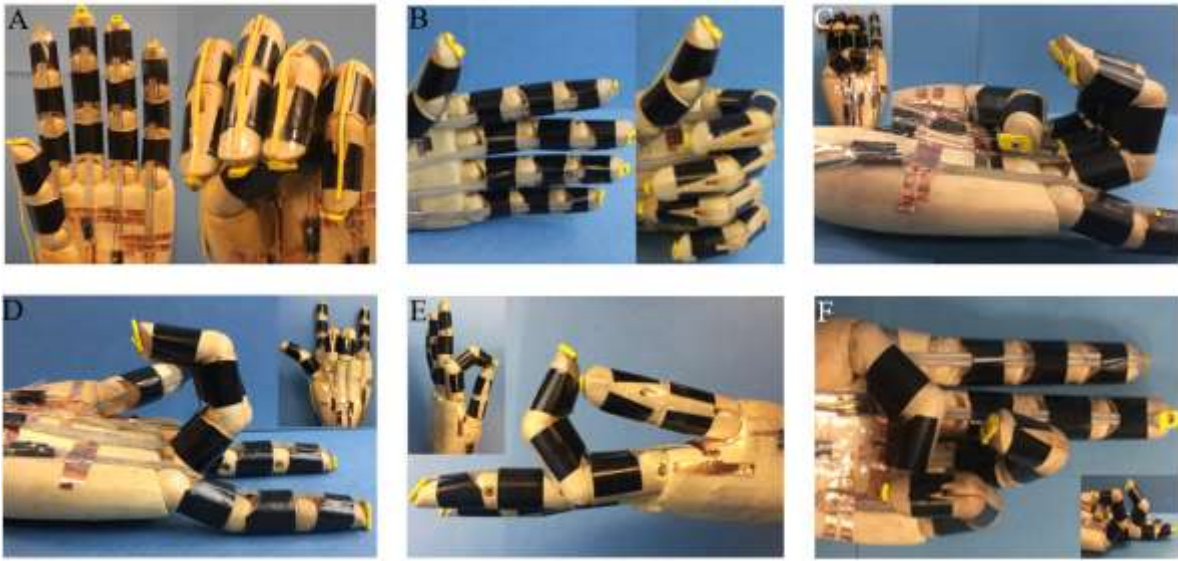


Fig. 6.3 Control fingers to achieve different actions. (A) The index finger bends to make an OK action. (B) Control the middle finger and the ring finger to bend at the same time. (C) Control the thumb, forefinger, middle finger, and ring finger to bend at the same time. (D) Control the index finger, middle finger, ring finger and little finger to bend at the same time in an upright position. (E) Control five fingers to bend at the same time in an upright position.

The prosthetic hand was able to perform more complex tasks like picking up or grabbing objects, shown in Fig. 6.4. Firstly, we demonstrated that the prosthetic hand is able to grab different shapes of objects, for example, a paper tube with diameter of 30mm (Fig. 6.4A), a plastic beaker (Fig.6.4B), and a maker pen (Fig.6.4B). Those objects have different shapes and weigh, while the prosthetic hand was able to handle all of them. Further, we tested the load carry capability of the prosthetic hand by letting it grabbing different weight of objects, the prosthetic hand can gently grab a light-weight soft plastic tube without break or

deform it (Fig.6.4D, weigh: 2.12g), as well as firmly grab a water bottle with a total weight of 200g. Only different current values were supplied to the LCE muscle for each case. Finally, a demonstration of lifting a bag with 251g groceries was demonstrated in Fig.6.4F.

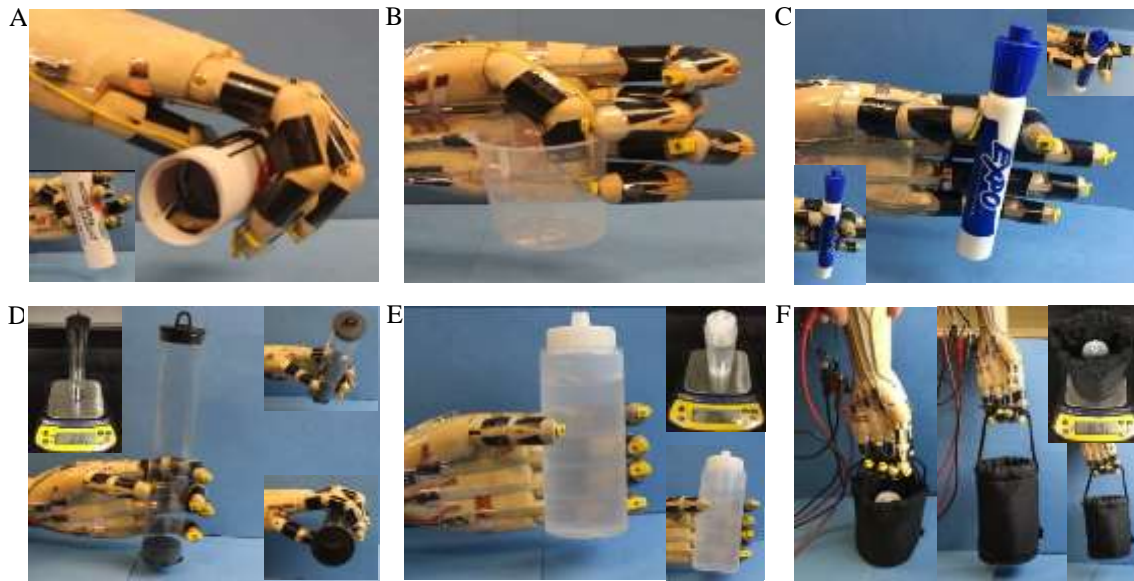


Fig. 6.4 *The practical application of robot hand. (A) Take the paper tube. (B) Take the cup. (C) Take a pen. (D) Take a slender plastic bucket which weight is 2.12g. (E) Take a bottle of water which weight is 200g. (F) Lifting objects which weight is 251.9g.*

6.3 Conclusion:

In this work, a novel artificial muscle was introduced as the “tendon” of a prosthetic hand. The combination of LCE and LM was demonstrated in this work and their basic performance was characterized as well. The LCE/LM “tendons” has a robust behavior and large strain output, however, the response is quite slow, this has something to do with our current LCE formula and the design of prosthetic hand itself. More promising formulas with a lower transition temperature will shorten the response. Meanwhile, our prosthetic hand is a solid wood piece which pertains a low thermal conductivity. Future design could focus on the shape and structure of prosthetic hand that fits for the use of the LCE/LM actuators. Other functionalities like making gestures and lifting weight was demonstrated as well, and proved to be robust.

Bibliography

- [1] S. Xu *et al.*, “Soft Microfluidic Assemblies of Sensors, Circuits, and Radios for the Skin,” *Science*, vol. 344, no. 6179, pp. 70–74, Apr. 2014.
- [2] S. C. B. Mannsfeld *et al.*, “Highly sensitive flexible pressure sensors with microstructured rubber dielectric layers,” *Nature Materials*, vol. 9, no. 10, pp. 859–864, Oct. 2010.
- [3] H. Lee *et al.*, “A graphene-based electrochemical device with thermoresponsive microneedles for diabetes monitoring and therapy,” *Nature Nanotechnology*, vol. 11, no. 6, pp. 566–572, Jun. 2016.
- [4] J. Choi, D. Kang, S. Han, S. B. Kim, and J. A. Rogers, “Thin, Soft, Skin-Mounted Microfluidic Networks with Capillary Bursting Valves for Chrono-Sampling of Sweat,” *Advanced Healthcare Materials*, vol. 6, no. 5, p. 1601355, 2017.
- [5] D.-H. Kim *et al.*, “Epidermal Electronics,” *Science*, vol. 333, no. 6044, pp. 838–843, Aug. 2011.
- [6] A. Chortos, J. Liu, and Z. Bao, “Pursuing prosthetic electronic skin,” *Nature Materials*, vol. 15, no. 9, pp. 937–950, Sep. 2016.
- [7] V. E. Abraira and D. D. Ginty, “The Sensory Neurons of Touch,” *Neuron*, vol. 79, no. 4, pp. 618–639, Aug. 2013.
- [8] “Wound Healing Center at Inova Loudoun treats complex wound and ostomy cases,” *Inova Newsroom*, 19-May-2017. [Online]. Available: <https://www.inovanewsroom.org/ilh/2017/05/wound-healing-center-at-inova-loudoun-treats-complex-wound-and-ostomy-cases/>. [Accessed: 23-Feb-2019].
- [9] K. S. Toohy, N. R. Sottos, J. A. Lewis, J. S. Moore, and S. R. White, “Self-healing materials with microvascular networks,” *Nature Materials*, vol. 6, no. 8, pp. 581–585, Aug. 2007.
- [10] B. C.-K. Tee, C. Wang, R. Allen, and Z. Bao, “An electrically and mechanically self-healing composite with pressure- and flexion-sensitive properties for electronic skin applications,” *Nature Nanotechnology*, vol. 7, no. 12, pp. 825–832, Dec. 2012.
- [11] P. Taynton, K. Yu, R. K. Shoemaker, Y. Jin, H. J. Qi, and W. Zhang, “Heat- or Water-Driven Malleability in a Highly Recyclable Covalent Network Polymer,” *Advanced Materials*, vol. 26, no. 23, pp. 3938–3942, 2014.
- [12] A. K. Awasthi, M. Wang, M. K. Awasthi, Z. Wang, and J. Li, “Environmental pollution and human body burden from improper recycling of e-waste in China: A short-review,” *Environmental Pollution*, vol. 243, pp. 1310–1316, Dec. 2018.

- [13] L. Brunsveld, B. J. B. Folmer, E. W. Meijer, and R. P. Sijbesma, "Supramolecular Polymers," *Chem. Rev.*, vol. 101, no. 12, pp. 4071–4098, Dec. 2001.
- [14] X.-F. Wu *et al.*, "Electrospinning core-shell nanofibers for interfacial toughening and self-healing of carbon-fiber/epoxy composites," *Journal of Applied Polymer Science*, vol. 129, no. 3, pp. 1383–1393, 2013.
- [15] Y. Yang and M. W. Urban, "Self-healing polymeric materials," *Chemical Society Reviews*, vol. 42, no. 17, pp. 7446–7467, 2013.
- [16] N. Roy, B. Bruchmann, and J.-M. Lehn, "DYNAMERS: dynamic polymers as self-healing materials," *Chemical Society Reviews*, vol. 44, no. 11, pp. 3786–3807, 2015.
- [17] C. J. Kloxin, T. F. Scott, B. J. Adzima, and C. N. Bowman, "Covalent Adaptable Networks (CANs): A Unique Paradigm in Cross-Linked Polymers," *Macromolecules*, vol. 43, no. 6, pp. 2643–2653, Mar. 2010.
- [18] T. Maeda, H. Otsuka, and A. Takahara, "Dynamic covalent polymers: Reorganizable polymers with dynamic covalent bonds," *Progress in Polymer Science*, vol. 34, no. 7, pp. 581–604, Jul. 2009.
- [19] H. Y. Park, C. J. Kloxin, T. F. Scott, and C. N. Bowman, "Stress Relaxation by Addition–Fragmentation Chain Transfer in Highly Cross-Linked Thiol–Yne Networks," *Macromolecules*, vol. 43, no. 24, pp. 10188–10190, Dec. 2010.
- [20] D. Montarnal, M. Capelot, F. Tournilhac, and L. Leibler, "Silica-Like Malleable Materials from Permanent Organic Networks," *Science*, vol. 334, no. 6058, pp. 965–968, Nov. 2011.
- [21] R. J. Wojtecki, M. A. Meador, and S. J. Rowan, "Using the dynamic bond to access macroscopically responsive structurally dynamic polymers," *Nature Materials*, vol. 10, no. 1, pp. 14–27, Jan. 2011.
- [22] L. Hines, K. Petersen, G. Z. Lum, and M. Sitti, "Soft Actuators for Small-Scale Robotics," *Advanced Materials*, vol. 29, no. 13, p. 1603483, 2017.
- [23] R. F. Shepherd *et al.*, "Multigait soft robot," *PNAS*, vol. 108, no. 51, pp. 20400–20403, Dec. 2011.
- [24] S. Shian, K. Bertoldi, and D. R. Clarke, "Dielectric Elastomer Based 'Grippers' for Soft Robotics," *Advanced Materials*, vol. 27, no. 43, pp. 6814–6819, 2015.
- [25] E. Acome *et al.*, "Hydraulically amplified self-healing electrostatic actuators with muscle-like performance," *Science*, vol. 359, no. 6371, pp. 61–65, Jan. 2018.
- [26] H.-T. Lin, G. G. Leisk, and B. Trimmer, "GoQBot: a caterpillar-inspired soft-bodied rolling robot," *Bioinspir. Biomim.*, vol. 6, no. 2, p. 026007, Apr. 2011.

- [27] I. Must *et al.*, “Ionic and Capacitive Artificial Muscle for Biomimetic Soft Robotics,” *Advanced Engineering Materials*, vol. 17, no. 1, pp. 84–94, 2015.
- [28] S. V. Ahir, A. R. Tajbakhsh, and E. M. Terentjev, “Self-Assembled Shape-Memory Fibers of Triblock Liquid-Crystal Polymers,” *Advanced Functional Materials*, vol. 16, no. 4, pp. 556–560, 2006.
- [29] O. M. Wani, H. Zeng, and A. Priimagi, “A light-driven artificial flytrap,” *Nature Communications*, vol. 8, p. 15546, May 2017.
- [30] C. Li, Y. Liu, X. Huang, and H. Jiang, “Direct Sun-Driven Artificial Heliotropism for Solar Energy Harvesting Based on a Photo-Thermomechanical Liquid-Crystal Elastomer Nanocomposite,” *Advanced Functional Materials*, vol. 22, no. 24, pp. 5166–5174, 2012.
- [31] C. Yuan *et al.*, “3D printed reversible shape changing soft actuators assisted by liquid crystal elastomers,” *Soft Matter*, vol. 13, no. 33, pp. 5558–5568, 2017.
- [32] S. Schuhladen, F. Preller, R. Rix, S. Petsch, R. Zentel, and H. Zappe, “Iris-like tunable aperture employing liquid-crystal elastomers,” *Adv. Mater. Weinheim*, vol. 26, no. 42, pp. 7247–7251, Nov. 2014.
- [33] Y. Yu, M. Nakano, and T. Ikeda, “Photomechanics: Directed bending of a polymer film by light,” *Nature*, vol. 425, no. 6954, p. 145, Sep. 2003.
- [34] T. Yoshino, M. Kondo, J. Mamiya, M. Kinoshita, Y. Yu, and T. Ikeda, “Three-Dimensional Photomobility of Crosslinked Azobenzene Liquid-Crystalline Polymer Fibers,” *Advanced Materials*, vol. 22, no. 12, pp. 1361–1363, 2010.
- [35] K. M. Lee, T. J. Bunning, and T. J. White, “Autonomous, Hands-Free Shape Memory in Glassy, Liquid Crystalline Polymer Networks,” *Advanced Materials*, vol. 24, no. 21, pp. 2839–2843, 2012.
- [36] Y. Sawa *et al.*, “Shape selection of twist-nematic-elastomer ribbons,” *PNAS*, vol. 108, no. 16, pp. 6364–6368, Apr. 2011.
- [37] H. Finkelmann, E. Nishikawa, G. G. Pereira, and M. Warner, “A New Opto-Mechanical Effect in Solids,” *Phys. Rev. Lett.*, vol. 87, no. 1, p. 015501, Jun. 2001.
- [38] M. D. Dickey, “Stretchable and Soft Electronics using Liquid Metals,” *Advanced Materials*, vol. 29, no. 27, p. 1606425, 2017.
- [39] S. Alkhalil, Y. Kolesnikov, and C. Karcher, “Measurement of electrical conductivity of liquid metals using Lorentz force sismometry,” in *8th International Conference on Electromagnetic Processing of Materials*, Cannes, France, 2015.
- [40] P. Cordier, F. Tournilhac, C. Soulié-Ziakovic, and L. Leibler, “Self-healing and thermoreversible rubber from supramolecular assembly,” *Nature*, vol. 451, no. 7181, pp. 977–980, Feb. 2008.

- [41] E. T. Thostenson and T.-W. Chou, “Carbon Nanotube Networks: Sensing of Distributed Strain and Damage for Life Prediction and Self Healing,” *Advanced Materials*, vol. 18, no. 21, pp. 2837–2841, 2006.
- [42] Y.-L. Rao *et al.*, “Stretchable Self-Healing Polymeric Dielectrics Cross-Linked Through Metal-Ligand Coordination,” *J. Am. Chem. Soc.*, vol. 138, no. 18, pp. 6020–6027, 11 2016.
- [43] J. Y. Oh *et al.*, “Intrinsically stretchable and healable semiconducting polymer for organic transistors,” *Nature*, vol. 539, no. 7629, pp. 411–415, 17 2016.
- [44] C.-H. Li *et al.*, “A highly stretchable autonomous self-healing elastomer,” *Nat Chem*, vol. 8, no. 6, pp. 618–624, 2016.
- [45] O. R. Cromwell, J. Chung, and Z. Guan, “Malleable and Self-Healing Covalent Polymer Networks through Tunable Dynamic Boronic Ester Bonds,” *J. Am. Chem. Soc.*, vol. 137, no. 20, pp. 6492–6495, May 2015.
- [46] M. O. Saed, A. H. Torbati, D. P. Nair, and C. M. Yakacki, “Synthesis of Programmable Main-chain Liquid-crystalline Elastomers Using a Two-stage Thiol-acrylate Reaction,” *J Vis Exp*, no. 107, Jan. 2016.
- [47] D. Son *et al.*, “Multifunctional wearable devices for diagnosis and therapy of movement disorders,” *Nat Nanotechnol*, vol. 9, no. 5, pp. 397–404, May 2014.
- [48] J. Kim *et al.*, “Stretchable silicon nanoribbon electronics for skin prosthesis,” *Nature Communications*, vol. 5, p. 5747, Dec. 2014.
- [49] S. Lee *et al.*, “A transparent bending-insensitive pressure sensor,” *Nature Nanotechnology*, vol. 11, no. 5, pp. 472–478, May 2016.
- [50] J. Kong *et al.*, “Nanotube Molecular Wires as Chemical Sensors,” *Science*, vol. 287, no. 5453, pp. 622–625, Jan. 2000.
- [51] D.-H. Kim, J. Xiao, J. Song, Y. Huang, and J. A. Rogers, “Stretchable, Curvilinear Electronics Based on Inorganic Materials,” *Advanced Materials*, vol. 22, no. 19, pp. 2108–2124, May 2010.
- [52] D.-H. Kim *et al.*, “Materials and noncoplanar mesh designs for integrated circuits with linear elastic responses to extreme mechanical deformations,” *PNAS*, vol. 105, no. 48, pp. 18675–18680, Dec. 2008.
- [53] D.-H. Kim *et al.*, “Stretchable and Foldable Silicon Integrated Circuits,” *Science*, vol. 320, no. 5875, pp. 507–511, Apr. 2008.
- [54] Y. Wang, Z. Li, and J. Xiao, “Stretchable Thin Film Materials: Fabrication, Application, and Mechanics,” *J. Electron. Packag*, vol. 138, no. 2, pp. 020801-020801–22, Apr. 2016.

- [55] Y. M. Song *et al.*, “Digital cameras with designs inspired by the arthropod eye,” *Nature*, vol. 497, no. 7447, pp. 95–99, May 2013.
- [56] H. Liu, Y. Huang, and H. Jiang, “Artificial eye for scotopic vision with bioinspired all-optical photosensitivity enhancer,” *Proceedings of the National Academy of Sciences of the United States of America*, vol. 113, no. 15, pp. 3982–3985, 2016.
- [57] Y. H. Jung *et al.*, “High-performance green flexible electronics based on biodegradable cellulose nanofibril paper,” *Nature Communications*, vol. 6, p. 7170, May 2015.
- [58] A. R. Studart, “Biologically Inspired Dynamic Material Systems,” *Angewandte Chemie International Edition*, vol. 54, no. 11, pp. 3400–3416, Mar. 2015.
- [59] R. Libanori *et al.*, “Stretchable heterogeneous composites with extreme mechanical gradients,” *Nature Communications*, vol. 3, p. 1265, Dec. 2012.
- [60] E. Palleau, S. Reece, S. C. Desai, M. E. Smith, and M. D. Dickey, “Self-Healing Stretchable Wires for Reconfigurable Circuit Wiring and 3D Microfluidics,” *Advanced Materials*, vol. 25, no. 11, pp. 1589–1592, 2013.
- [61] Y. Li, S. Chen, M. Wu, and J. Sun, “Polyelectrolyte Multilayers Impart Healability to Highly Electrically Conductive Films,” *Advanced Materials*, vol. 24, no. 33, pp. 4578–4582, Aug. 2012.
- [62] C. Wang, H. Wu, Z. Chen, M. T. McDowell, Y. Cui, and Z. Bao, “Self-healing chemistry enables the stable operation of silicon microparticle anodes for high-energy lithium-ion batteries,” *Nat Chem*, vol. 5, no. 12, pp. 1042–1048, Dec. 2013.
- [63] J. A. Neal, D. Mozhdghi, and Z. Guan, “Enhancing Mechanical Performance of a Covalent Self-Healing Material by Sacrificial Noncovalent Bonds,” *J. Am. Chem. Soc.*, vol. 137, no. 14, pp. 4846–4850, Apr. 2015.
- [64] S. A. Odom *et al.*, “A Self-healing Conductive Ink,” *Advanced Materials*, vol. 24, no. 19, pp. 2578–2581, May 2012.
- [65] B. J. Blaiszik *et al.*, “Autonomic Restoration of Electrical Conductivity,” *Advanced Materials*, vol. 24, no. 3, pp. 398–401, 2012.
- [66] C. Hou, T. Huang, H. Wang, H. Yu, Q. Zhang, and Y. Li, “A strong and stretchable self-healing film with self-activated pressure sensitivity for potential artificial skin applications,” *Scientific Reports*, vol. 3, p. 3138, Nov. 2013.
- [67] P. Taynton *et al.*, “Repairable Woven Carbon Fiber Composites with Full Recyclability Enabled by Malleable Polyimine Networks,” *Advanced Materials*, vol. 28, no. 15, pp. 2904–2909, 2016.

- [68] B. J. Blaiszik, S. L. B. Kramer, S. C. Olugebefola, J. S. Moore, N. R. Sottos, and S. R. White, "Self-Healing Polymers and Composites," *Annual Review of Materials Research*, vol. 40, no. 1, pp. 179–211, 2010.
- [69] Y. C. Yuan, T. Yin, M. Z. Rong, and M. Q. Zhang, "Self healing in polymers and polymer composites. Concepts, realization and outlook: A review," *Express Polymer Letters*, vol. 2, no. 4, pp. 238–250, 2008.
- [70] V. K. Thakur, M. K. Thakur, P. Raghavan, and M. R. Kessler, "Progress in Green Polymer Composites from Lignin for Multifunctional Applications: A Review," *ACS Sustainable Chem. Eng.*, vol. 2, no. 5, pp. 1072–1092, May 2014.
- [71] K. Song, "Self-healing and self-cleaning nanocomposite coatings," *Advanced Materials*, p. 4, 2018.
- [72] D. Son *et al.*, "An integrated self-healable electronic skin system fabricated via dynamic reconstruction of a nanostructured conducting network," *Nat Nanotechnol*, vol. 13, no. 11, pp. 1057–1065, Nov. 2018.
- [73] F. Ghezzi *et al.*, "Development and Characterization of Healable Carbon Fiber Composites with a Reversibly Cross Linked Polymer," *Journal of Composite Materials*, vol. 44, no. 13, pp. 1587–1603, Jun. 2010.
- [74] "Thermo-responsive mending of polymers crosslinked by thermally reversible covalent bond: Polymers from bisfuranic terminated poly(ethylene adipate) and tris-maleimide | Request PDF," *ResearchGate*. [Online]. Available: https://www.researchgate.net/publication/238117465_Thermo-responsive_mending_of_polymers_crosslinked_by_thermally_reversible_covalent_bond_Polymers_from_bisfuranic_terminated_polyethylene_adipate_and_tris-maleimide. [Accessed: 25-Feb-2019].
- [75] P. Du, X. Liu, Z. Zheng, X. Wang, T. Joncheray, and Y. Zhang, "Synthesis and characterization of linear self-healing polyurethane based on thermally reversible Diels–Alder reaction," *RSC Adv.*, vol. 3, no. 35, pp. 15475–15482, Aug. 2013.
- [76] E. D. Rodriguez, X. Luo, and P. T. Mather, "Linear/Network Poly(ϵ -caprolactone) Blends Exhibiting Shape Memory Assisted Self-Healing (SMASH)," *ACS Appl. Mater. Interfaces*, vol. 3, no. 2, pp. 152–161, Feb. 2011.
- [77] J. Liu *et al.*, "An advanced elastomer with an unprecedented combination of excellent mechanical properties and high self-healing capability," *Journal of Materials Chemistry A*, vol. 5, no. 48, pp. 25660–25671, 2017.
- [78] C. Zeng, H. Seino, J. Ren, K. Hatanaka, and N. Yoshie, "Bio-Based Furan Polymers with Self-Healing Ability," *Macromolecules*, vol. 46, no. 5, pp. 1794–1802, Mar. 2013.
- [79] G. Hong *et al.*, "Mechanoresponsive Healable Metallosupramolecular Polymers," *Macromolecules*, vol. 46, no. 21, pp. 8649–8656, Nov. 2013.

- [80] Z. Zou, C. Zhu, Y. Li, X. Lei, W. Zhang, and J. Xiao, "Rehealable, fully recyclable, and malleable electronic skin enabled by dynamic covalent thermoset nanocomposite," *Science Advances*, vol. 4, no. 2, p. eaaq0508, Feb. 2018.
- [81] A. M. Peterson, R. E. Jensen, and G. R. Palmese, "Room-Temperature Healing of a Thermosetting Polymer Network Using the Diels–Alder Reaction," *ACS Appl. Mater. Interfaces*, vol. 2, no. 7, pp. 2169–2169, Jul. 2010.
- [82] C.-M. Chung, Y.-S. Roh, S.-Y. Cho, and J.-G. Kim, "Crack Healing in Polymeric Materials via Photochemical [2+2] Cycloaddition," p. 3.
- [83] Y. Amamoto, J. Kamada, H. Otsuka, A. Takahara, and K. Matyjaszewski, "Repeatable Photoinduced Self-Healing of Covalently Cross-Linked Polymers through Reshuffling of Trithiocarbonate Units," *Angewandte Chemie International Edition*, vol. 50, no. 7, pp. 1660–1663, 2011.
- [84] B. Ghosh and M. W. Urban, "Self-Repairing Oxetane-Substituted Chitosan Polyurethane Networks," *Science*, vol. 323, no. 5920, pp. 1458–1460, Mar. 2009.
- [85] M. Burnworth *et al.*, "Optically healable supramolecular polymers," *Nature*, vol. 472, no. 7343, pp. 334–337, Apr. 2011.
- [86] N. N. Xia, X. M. Xiong, M. Z. Rong, M. Q. Zhang, and F. Kong, "Self-Healing of Polymer in Acidic Water toward Strength Restoration through the Synergistic Effect of Hydrophilic and Hydrophobic Interactions," *ACS Appl. Mater. Interfaces*, vol. 9, no. 42, pp. 37300–37309, Oct. 2017.
- [87] J. Li, H. Ejima, and N. Yoshie, "Seawater-Assisted Self-Healing of Catechol Polymers via Hydrogen Bonding and Coordination Interactions," *ACS Appl. Mater. Interfaces*, vol. 8, no. 29, pp. 19047–19053, Jul. 2016.
- [88] N. N. Xia, M. Z. Rong, and M. Q. Zhang, "Stabilization of catechol–boronic ester bonds for underwater self-healing and recycling of lipophilic bulk polymer in wider pH range," *Journal of Materials Chemistry A*, vol. 4, no. 37, pp. 14122–14131, 2016.
- [89] C. Kim and N. Yoshie, "Polymers healed autonomously and with the assistance of ubiquitous stimuli: how can we combine mechanical strength and a healing ability in polymers?," *Polymer Journal*, vol. 50, no. 10, p. 919, Oct. 2018.
- [90] P. Taynton *et al.*, "Re-healable polyimine thermosets: polymer composition and moisture sensitivity," *Polym. Chem.*, vol. 7, no. 46, pp. 7052–7056, Nov. 2016.
- [91] P. Song, H. Qin, H.-L. Gao, H.-P. Cong, and S.-H. Yu, "Self-healing and superstretchable conductors from hierarchical nanowire assemblies," *Nature Communications*, vol. 9, no. 1, p. 2786, Jul. 2018.
- [92] A. C. Balazs, T. Emrick, and T. P. Russell, "Nanoparticle Polymer Composites: Where Two Small Worlds Meet," *Science*, vol. 314, no. 5802, pp. 1107–1110, Nov. 2006.

- [93] M. Kubo *et al.*, “Stretchable Microfluidic Radiofrequency Antennas,” *Advanced Materials*, vol. 22, no. 25, pp. 2749–2752, 2010.
- [94] A. E. Aliev *et al.*, “Giant-Stroke, Superelastic Carbon Nanotube Aerogel Muscles,” *Science*, vol. 323, no. 5921, pp. 1575–1578, Mar. 2009.
- [95] American Society for Testing and Materials. Philadelphia, Ed., *Standard Test Method for Apparent Shear Strength of Single-Lap-Joint Adhesively Bonded Metal Specimens by Tension Loading (Metal-to-Metal)*. West Conshohocken, PA: ASTM, 1999.
- [96] “The soft touch of robots,” *Nature Reviews Materials*, vol. 3, no. 6, p. 71, Jun. 2018.
- [97] T. J. Wallin, J. Pikul, and R. F. Shepherd, “3D printing of soft robotic systems,” *Nature Reviews Materials*, vol. 3, no. 6, p. 84, Jun. 2018.
- [98] D. Rus and M. T. Tolley, “Design, fabrication and control of origami robots,” *Nature Reviews Materials*, vol. 3, no. 6, p. 101, Jun. 2018.
- [99] S. Palagi and P. Fischer, “Bioinspired microrobots,” *Nature Reviews Materials*, vol. 3, no. 6, p. 113, Jun. 2018.
- [100] C. Yang and Z. Suo, “Hydrogel ionotronics,” *Nature Reviews Materials*, vol. 3, no. 6, p. 125, Jun. 2018.
- [101] M. Cianchetti, C. Laschi, A. Menciassi, and P. Dario, “Biomedical applications of soft robotics,” *Nature Reviews Materials*, vol. 3, no. 6, p. 143, Jun. 2018.
- [102] M. Sitti, “Miniature soft robots — road to the clinic,” *Nature Reviews Materials*, vol. 3, no. 6, p. 74, Jun. 2018.
- [103] K. Althoefer, “Antagonistic actuation and stiffness control in soft inflatable robots,” *Nature Reviews Materials*, vol. 3, no. 6, p. 76, Jun. 2018.
- [104] C. Walsh, “Human-in-the-loop development of soft wearable robots,” *Nature Reviews Materials*, vol. 3, no. 6, p. 78, Jun. 2018.
- [105] C. Xu, G. T. Stiubianu, and A. A. Gorodetsky, “Adaptive infrared-reflecting systems inspired by cephalopods,” *Science*, vol. 359, no. 6383, pp. 1495–1500, Mar. 2018.
- [106] P. Rothemund *et al.*, “A soft, bistable valve for autonomous control of soft actuators,” *Science Robotics*, vol. 3, no. 16, p. eaar7986, Mar. 2018.
- [107] E. Coevoet *et al.*, “Software toolkit for modeling, simulation, and control of soft robots,” *Advanced Robotics*, vol. 31, no. 22, pp. 1208–1224, Nov. 2017.
- [108] J. H. Pikul, S. Li, H. Bai, R. T. Hanlon, I. Cohen, and R. F. Shepherd, “Stretchable surfaces with programmable 3D texture morphing for synthetic camouflaging skins,” *Science*, vol. 358, no. 6360, pp. 210–214, Oct. 2017.

- [109] T. J. White and D. J. Broer, “Programmable and adaptive mechanics with liquid crystal polymer networks and elastomers,” *Nature Materials*, vol. 14, no. 11, pp. 1087–1098, Nov. 2015.
- [110] A. Nathan *et al.*, “Flexible Electronics: The Next Ubiquitous Platform,” *Proceedings of the IEEE*, vol. 100, no. Special Centennial Issue, pp. 1486–1517, May 2012.
- [111] M. Stoppa and A. Chiolerio, “Wearable Electronics and Smart Textiles: A Critical Review,” *Sensors*, vol. 14, no. 7, pp. 11957–11992, Jul. 2014.
- [112] K. D. Harris, A. L. Elias, and H.-J. Chung, “Flexible electronics under strain: a review of mechanical characterization and durability enhancement strategies,” *J Mater Sci*, vol. 51, no. 6, pp. 2771–2805, Mar. 2016.
- [113] C. Lee *et al.*, “Soft robot review,” *Int. J. Control Autom. Syst.*, vol. 15, no. 1, pp. 3–15, Feb. 2017.
- [114] K.-J. Cho, J.-S. Koh, S. Kim, W.-S. Chu, Y. Hong, and S.-H. Ahn, “Review of manufacturing processes for soft biomimetic robots,” *Int. J. Precis. Eng. Manuf.*, vol. 10, no. 3, pp. 171–181, Jul. 2009.
- [115] N. Elango and A. A. M. Faudzi, “A review article: investigations on soft materials for soft robot manipulations,” *Int J Adv Manuf Technol*, vol. 80, no. 5, pp. 1027–1037, Sep. 2015.
- [116] M. Manti, V. Cacucciolo, and M. Cianchetti, “Stiffening in Soft Robotics: A Review of the State of the Art,” *IEEE Robotics Automation Magazine*, vol. 23, no. 3, pp. 93–106, Sep. 2016.
- [117] K. A. Daltorio, A. D. Horchler, S. Gorb, R. E. Ritzmann, and R. D. Quinn, “A small wall-walking robot with compliant, adhesive feet,” in *2005 IEEE/RSJ International Conference on Intelligent Robots and Systems*, 2005, pp. 3648–3653.
- [118] D.-H. Kim *et al.*, “Epidermal Electronics,” *Science*, vol. 333, no. 6044, pp. 838–843, Aug. 2011.
- [119] D. J. Lipomi *et al.*, “Skin-like pressure and strain sensors based on transparent elastic films of carbon nanotubes,” *Nature Nanotechnology*, vol. 6, no. 12, pp. 788–792, Dec. 2011.
- [120] S. Musallam, B. D. Corneil, B. Greger, H. Scherberger, and R. A. Andersen, “Cognitive Control Signals for Neural Prosthetics,” *Science*, vol. 305, no. 5681, pp. 258–262, Jul. 2004.
- [121] Y. Onuki, U. Bhardwaj, F. Papadimitrakopoulos, and D. J. Burgess, “A Review of the Biocompatibility of Implantable Devices: Current Challenges to Overcome Foreign Body Response,” *J Diabetes Sci Technol*, vol. 2, no. 6, pp. 1003–1015, Nov. 2008.

- [122] T. Li *et al.*, “Agile and Resilient Insect-Scale Robot,” *Soft Robotics*, vol. 6, no. 1, pp. 133–141, Nov. 2018.
- [123] B. Bhandari, G.-Y. Lee, and S.-H. Ahn, “A review on IPMC material as actuators and sensors: Fabrications, characteristics and applications,” *Int. J. Precis. Eng. Manuf.*, vol. 13, no. 1, pp. 141–163, Jan. 2012.
- [124] T. Guin *et al.*, “Layered liquid crystal elastomer actuators,” *Nature Communications*, vol. 9, no. 1, p. 2531, Jun. 2018.
- [125] M. K. McBride *et al.*, “A readily programmable, fully reversible shape-switching material,” *Science Advances*, vol. 4, no. 8, p. eaat4634, Aug. 2018.
- [126] S. W. Ula, N. A. Traugott, R. H. Volpe, R. R. Patel, K. Yu, and C. M. Yakacki, “Liquid crystal elastomers: an introduction and review of emerging technologies,” *Liquid Crystals Reviews*, vol. 6, no. 1, pp. 78–107, Jan. 2018.
- [127] C. M. Yakacki, M. Saed, D. P. Nair, T. Gong, S. M. Reed, and C. N. Bowman, “Tailorable and programmable liquid-crystalline elastomers using a two-stage thiol–acrylate reaction,” *RSC Advances*, vol. 5, no. 25, pp. 18997–19001, 2015.
- [128] R. G. E. Clement, K. E. Bugler, and C. W. Oliver, “Bionic prosthetic hands: A review of present technology and future aspirations,” *The Surgeon*, vol. 9, no. 6, pp. 336–340, Dec. 2011.
- [129] P. Geethanjali, “Myoelectric control of prosthetic hands: state-of-the-art review,” *Med Devices (Auckl)*, vol. 9, pp. 247–255, Jul. 2016.
- [130] J. T. Belter and A. M. Dollar, “Performance characteristics of anthropomorphic prosthetic hands,” in *2011 IEEE International Conference on Rehabilitation Robotics*, 2011, pp. 1–7.
- [131] M. Controzzi, C. Cipriani, and M. C. Carrozza, “Design of Artificial Hands: A Review,” in *The Human Hand as an Inspiration for Robot Hand Development*, R. Balasubramanian and V. J. Santos, Eds. Cham: Springer International Publishing, 2014, pp. 219–246.
- [132] “Vincent Systems GmbH.” [Online]. Available: <https://vincentsystems.de/en/>. [Accessed: 25-Feb-2019].
- [133] “i-limb ultra | Touch Bionics.” [Online]. Available: <http://touchbionics.com/products/active-prostheses/i-limb-ultra>. [Accessed: 25-Feb-2019].
- [134] “Life changing myoelectric hand packed with the latest technology - bebionic.” [Online]. Available: http://bebionic.com/the_hand. [Accessed: 25-Feb-2019].

- [135] “Michelangelo prosthetic hand.” [Online]. Available: <https://www.ottobockus.com/prosthetics/upper-limb-prosthetics/solution-overview/michelangelo-prosthetic-hand/>. [Accessed: 25-Feb-2019].
- [136] and and J. H. Chang, “Design and control of a robotic finger for prosthetic hands,” in *Proceedings 1999 IEEE/RSJ International Conference on Intelligent Robots and Systems. Human and Environment Friendly Robots with High Intelligence and Emotional Quotients (Cat. No.99CH36289)*, 1999, vol. 1, pp. 113–117 vol.1.
- [137] M. Zecca, S. Micera, M. C. Carrozza, and P. Dario, “Control of Multifunctional Prosthetic Hands by Processing the Electromyographic Signal,” *CRB*, vol. 30, no. 4–6, 2002.
- [138] H. Takeda, N. Tsujiuchi, T. Koizumi, H. Kan, M. Hirano, and Y. Nakamura, “Development of prosthetic arm with pneumatic prosthetic hand and tendon-driven wrist,” in *2009 Annual International Conference of the IEEE Engineering in Medicine and Biology Society*, 2009, pp. 5048–5051.
- [139] K. Schorger, J. P. Simon, D. Clark, and A. Williams, “Pneumatic hand prosthesis project,” May 2018.
- [140] “500459_RevB_Rockson_Clinical_Highlights-1.pdf.” .
- [141] K. Andrianesis and A. Tzes, “Development and Control of a Multifunctional Prosthetic Hand with Shape Memory Alloy Actuators,” *J Intell Robot Syst*, vol. 78, no. 2, pp. 257–289, May 2015.
- [142] B. Le, K. McVary, K. McKenna, and A. Colombo, “A Novel Thermal-activated Shape Memory Penile Prosthesis: Comparative Mechanical Testing,” *Urology*, vol. 99, pp. 136–141, Jan. 2017.
- [143] A. P. Gerratt, H. O. Michaud, and S. P. Lacour, “Elastomeric Electronic Skin for Prosthetic Tactile Sensation,” *Advanced Functional Materials*, vol. 25, no. 15, pp. 2287–2295, 2015.
- [144] J. Mehta, Y. Chandra, and R. P. Tewari, “The Use of Dielectric Elastomer Actuators for Prosthetic, Orthotic and Bio-Robotic Applications,” *Procedia Computer Science*, vol. 133, pp. 569–575, Jan. 2018.
- [145] S. Bhinder, R. Flores, K. Inuzuka, and R. Ramos, “Flexion-Induced Automatic Prosthetic for Partial-Finger Amputees,” *Pacific Undergraduate Research and Creativity Conference (PURCC)*, May 2017.